

Development of Fluorescent Hybrid Nanostructure for Influenza Virus Detection and Cell Imaging

メタデータ	言語: en 出版者: Shizuoka University 公開日: 2015-06-24 キーワード (Ja): キーワード (En): 作成者: Syed, Rahin Ahmed メールアドレス: 所属:
URL	https://doi.org/10.14945/00008740

THESIS

**Development of Fluorescent Hybrid Nanostructure for
Influenza Virus Detection and Cell Imaging**

Syed Rahin AHMED

Graduate School of Science and Educational Division

Department of Bioscience

Shizuoka University

December 2014

THESIS

**Development of Fluorescent Hybrid Nanostructure for
Influenza Virus Detection and Cell Imaging**

インフルエンザウイルス検出及び細胞イメージングに向けた
蛍光ハイブリッドナノ構造体の開発

ソイルド ラヒン アハメッド

静岡大学

大学院自然科学系教育部

バイオサイエンス 専攻

2014年12月

Graduate School of Science and Educational Division
Major in Bioscience
Shizuoka University

CERTIFICATE OF APPROVAL

This is to certify that the Ph.D. thesis entitled:

Development of Fluorescent Hybrid Nanostructure for Influenza Virus
Detection and Cells Imaging

By
Syed Rahin AHMED

has been approved by the Thesis Committee on January 29, 2015 as
satisfactory for the thesis requirement for the degree of Doctor of Science

Thesis Committee

Professor Enoch Y Park (Supervisor)	Signature
Professor Jaebeom Lee (Co-supervisor)	Signature
Professor Kwangnak Koh (Co-supervisor)	Signature
Professor Naoharu Watanabe (Co-supervisor)	Signature
Professor Hiroshi Inokawa (Co-supervisor)	Signature
Professor Tatsuya Kato (Co-supervisor)	Signature

TABLE OF CONTENTS

LIST OF FIGURES	v
LIST OF TABLES	ix
LIST OF ABBREVIATIONS	x
ABSTRACT	1
CHAPTER I. INTRODUCTION	
1.1. Fluorescent hybrid nanostructure.....	5
1.2. Plasmon/semiconductor hybrid structure and its bio-applications.....	6
1.3. Magneto/semiconductor hybrid structure and its bio-applications.....	14
1.4. Conclusion.....	19
CHAPTER II. PHOTOLUMINESCENCE ENHANCEMENT ON QUANTUM DOTS/Ag NANONEEDLES HYBRID NANOSTRUCTURE	
2.1. Introduction.....	21
2.2. Experimental details.....	22
2.2.1. Methods.....	22
2.2.2. Preparation of thermal-coating substrate and Ag-nNDL	22
2.2.3. Synthesis of CdSe/ZnS QDs.	23
2.2.4. QD coating on the smooth and rough substrates	23
2.2.5. Optical and microscopic measurements.....	24
2.3. Results and discussion.....	24
2.3.1 SEM & AFM Images of Ag-nNDL film.....	24
2.3.2. QD coating on smooth and rough substrates.....	26
2.3.3. Spectroscopic study of QDs on Ag substrates.....	27
2.4. Conclusions.....	32

CHAPTER III. FLUORESCENT HYBRID NANOSTRUCTURE-BASED ASSAY PLATFORM FOR VIRUS DETECTION

3.1. Introduction.....	34
3.2. Materials and methods.....	36
3.2.1. Materials.....	36
3.2.2. Preparation of NPGL and semiconductor nanoparticles.....	36
3.2.3. Immobilization of CdTe QDs on the NPGL substrate.....	37
3.2.4. Immobilization of CdTe QDs on the NPGL substrate.....	37
3.2.5. Topographic observation and spectroscopic studies of NPGL films.....	38
3.2.6. Characterization of antibody specificity.....	38
3.2.7. Conjugation of HA Ab66189 antibody with NPGL and its binding check using ELISA.....	39
3.2.8. Binding capacity of HA Ab66189 antibody with cysteamine capped QDs using ELISA.....	39
3.2.9. Detection platform of HA, Influenza viruses A/Beijing/262/95 (H1N1), and A/Yokohama/110/2009 (H3N2) on NPGL.....	40
3.2.10. Detection of influenza virus by rapid influenza diagnostic test (RIDT).....	40
3.3. Results and discussion.....	41
3.3.1. Topographic observation of NPGL films.....	41
3.3.2. Spectroscopic and microscopic studies of the NPGL films.....	42
3.3.3. Immunoassay of HA on NPGL05 and QDs.....	44
3.3.4. Immunoassay for virus detection.....	47
3.3.5. Detection of influenza virus using rapid influenza diagnostic test (RIDT).....	49
3.4. Conclusions.....	51

CHAPTER IV. FLUORESCENT HYBRID NANOSTRUCTURE FOR IMAGING COLON CARCINOMA CELLS

4.1. Introduction.....	53
4.2. Materials & Methods.....	55
4.2.1 Materials.....	55
4.2.2. Synthesis of CdTe QDs.....	55
4.2.3. Synthesis of Fe ₃ O ₄ NPs.....	55
4.2.4. Preparation of FMNPs.....	56
4.2.5. TIRF microscope and TEM Imaging of FMNPs.....	56
4.2.6. Superconducting quantum interference device (SQUID) measurement.....	56
4.2.7. Cell lines and cell cultures.....	57
4.2.8. Trypan blue test.....	57
4.2.9. Preparation of hCC49 antibody Fab regions.....	58
4.2.10. Conjugation of hCC49 antibody Fab region with FMNPs and its binding activity.....	59
4.2.11. Cellular imaging using hCC49 antibody Fab region conjugated FMNPs.....	59
4.3. Results and discussion.....	60
4.3.1. Spectroscopic study of CdTe QDs and FMNPs.....	60
4.3.2. Total internal reflection fluorescence (TIRF), transmission electron microscope (TEM) images and dynamic light scattering (DLS) of studies FMNPs.....	61
4.3.3. Superconducting quantum interference device (SQUID) study of FMNPs.....	62
4.3.4. Stability of FMNPs and cell viability in the presence of FMNPs....	63
4.3.5. Confirmation of FMNPs conjugated with Fab region of hCC49 antibody	64
4.3.6. Cellular imaging of colon carcinoma cells using FMNPs conjugated with Fab region of hCC49 antibody.....	65
4.4. Conclusions.....	67

CHAPTER V. CONCLUSIONS AND FUTURE PERSPECTIVES

5.1. Conclusions..... 69
5.2. Future Perspectives..... 69

REFERENCES..... 71

PUBLICATIONS..... 84

ACKNOWLEDGEMENT..... 85

LIST OF FIGURES

- Figure 1.1.** TEM images of spiky SPs assembled in the presence of different amounts of smooth Fe₃O₄ @Au core-shell particles: (a) 4.5 nM, (b) 8.9 nM, (c) 13.2 nM, and (d) 17.5 nM. Insets show magnified images of corresponding individual SPs. [Volume of smooth Fe₃O₄ @Au seeds increased from 100 to 400 μL in 100 μL increments for spectra (a)–(d)].…………… 8
- Figure 1.2.** (i) Schematic of preparation of the multifunctional gold nanostar/quantum dots doped SiO₂ nanoparticles. (ii) TEM images of gold nanostar with different seed volume a 20 μL, b 100 μL (iii) The fluorescence image of MDA-MB-231 breast cells gained under a UV irradiation and b white light irradiation after the MFNPs were linked onto the breast cells.…………… 9
- Figure 1.3.** 30μm×30μm tapping-mode AFM images of ordered PS particles (a) 20 μm×20μm tapping-mode AFM images of silver arrays made with a latex mask of PS particles 4.9μm in diameter. (d) 15μm×15μm image of arrays made with a latex mask of PS particles 3.2 μm in diameter. (e,f) Fluorescence and optical images, of a single CdSe@ZnS hexagonal array made with a 3.2 μm particles diameter PS mask. …………… 13
- Figure 1.4.** (i) Schematic of the formation of the CS-SPs. (ii) A set of TEM images of CS-SPs at different magnifications. Scale bars, 500 nm, 100nm and 10nm (a–c), respectively.(iii) Intravital multiphoton microscopy through the cranial window was carried out at different time point: pre-injection (a), 4 h post injection (b) and 24 h post injection (c). Scale bar, 150 μm. Images from red and green channels are shown in small panels (top: red channel, bottom: green channel). Green emission signals are generated from a blood vessel tracer and red emission signals are generated by mPEG-functionalized silica-CSSPs. In vivo T2-weighted magnetic resonance images of pre- (h) and 24 h post- (i) injection of mPEG-silane functionalized silica-CS-SPs. Twenty four hours post-injection image show clear tumour visualization (denoted by the red dash line). Scale bar, 3 mm. (j) The corresponding T2 relaxation (relax.) time fitting results for the tumour region at time points of pre-injection (Pre., blue bar) and 24 h post injection (Post., red bar). …………… 15

- Figure 1.5.** (i) Schematic illustration of immuno-labeling using $\text{Fe}_3\text{O}_4/\text{CdTe}$ nanocomposites which are formed by linking multiple TGA stabilized CdTe QDs with the thiol-functionalized silica-coated iron oxide nanoparticles.(ii) Images of live HeLa cells (a) without interacting with any nanoparticles, (b) directly labeled by $\text{Fe}_3\text{O}_4/\text{CdTe}$ nanocomposites without antibody conjugated, and (c) immuno-labeled by $\text{Fe}_3\text{O}_4/\text{CdTe}$ nanocomposites conjugated with anti-CEACAM8. In the three panels, the left columns represent the phasecontrast images, the center columns represent the fluorescent images, and the right columns are the overlays of the left and center columns.17
- Figure 1.6.** (i) TEM image of (a) reference Fe_3O_4 NPs and (b) core/shell $\text{Fe}_3\text{O}_4/\text{ZnSe}$ NPs. (ii) (a) Magnetization against T under ZFC and FC conditions for the reference Fe_3O_4 and core/shell $\text{Fe}_3\text{O}_4/\text{ZnSe}$ NP samples. (b) PLE and PL spectra measured at room temperature for the reference ZnSe and core/shell $\text{Fe}_3\text{O}_4/\text{ZnSe}$ NP samples. 18
- Figure 2.1.** SEM images of Ag-nNDLs at $\times 50,000$ (A) and $\times 150,000$ (B). Topographical AFM images of Ag films: (C) smooth Ag substrate and (D) rough Ag-nNDLs. Insets show the depth profiles along each line.26
- Figure 2.2.** AFM images of smooth (A) and rough (B) substrate after QD coating. 27
- Figure 2.3.** UV and PL spectra of CdSe/ZnS QDs (A) and UV-vis spectra of Ag-nNDLS (B). a, smooth Ag nanofilm; b, Ag-nNDL. (C) Absorbance spectra of QDs on each film. (D) Fluorescence spectra of QDs in chloroform at the same absorbance intensity. 29
- Figure 2.4.** PL spectra for CdSe/ZnS nanocrystals on silver surfaces (A). a, smooth surface; b, rough surface. (B) Time profile of PL signal for CdSe/ZnS nanocrystals on Ag surfaces. 30
- Figure 3.1.** Schematic of virus detection using nanoporous gold leaf (NPGL) film. The NPGL (a) and quantum dots (QDs) (b) were firstly conjugated with anti-hemagglutinin (HA) antibodies (anti-HA Ab, Y shape) by the reaction of ethylcarbodiimide (EDC)/N-hydroxysuccinimide (NHS). Then anti-HA Ab-conjugated with NPGL and QDs form complex (c) in presence of HA on the surface of influenza virus, finally enhancing PL intensity. 35

- Figure 3.2.** SEM and AFM images and the measured R_{rms} of each NPGL sample with various dealloying times (5–60 min), where e.g., NPGL05 depicts 5 min of dealloying time. Dealloyed times are 5 min (a), 10 min (b), 30 min (c) and 60 min (d). Bars in upper and lower panels denote 300 and 500 nm respectively.41
- Figure 3.3.** (A) UV and PL spectra of CdTe QDs; (B) absorbance spectra of QDs on different films and PL spectra of QDs in aqueous solvent at the same absorbance intensity. 43
- Figure 3.4.** (a) Photoluminescence (PL) spectra of QDs on different roughnesses of NPGL and glass substrate (for QD only); (b) time-based fluorescence kinetics profile of PL signal for QDs on different surfaces; (c) lifetimes (τ) variance depending on surface roughness; (d) fluorescence microscopic image of QDs on metallic nanostripe patterns. IRF in (b) stands for instrumental response function. 44
- Figure 3.5.** (A) ELISA for HA ab66189 antibody binding with influenza H1N1 HA; (B) ELISA for recombinant influenza H1N1 HA binding with HA ab661891 antibody-conjugated NPGL05; (C) Binding check of antibody with NPGL05 with naked eyes; (D) FTIR spectrum of antibody binding with NPGL. The error bars in A and B indicate standard deviation (SD) in each measurement. 45
- Figure 3.6.** (A) PL and absorbance spectra of cysteamine capped QDs; (B) ELISA for HA ab661891 antibody-modified QDs with recombinant influenza H1N1 HA ; (C) FTIR spectrum of antibody binding with QDs ; (D) Fluorescence microscopic image of virus detection. The error bars in B indicate SD in each measurement. 46
- Figure 3.7.** (a) PL enhancement of QDs with and without the nanostructure; (b) PL enhancement corresponding on different quantities of recombinant influenza HA (H1N1) on anti-HA Ab-conjugated NPGL05. (Inset) The calibration curve of PL intensity versus HA concentration. The error bars indicate SD in each measurement. 47
- Figure 3.8.** (a) PL spectroscopic detection of influenza virus A/Beijing/262/95 (H1N1) using anti-HA (H1N1) Ab (ab66189)-bioconjugated QDs depending on the existence of anti-HA (H1N1) Ab (ab66189)-bioconjugated NPGL05

film; (b) PL intensity versus influenza virus A/Beijing/262/95 (H1N1) concentration; (c) ELISA results for anti-HA (H3N2) Ab 82454 binding with influenza virus A/Yokohama/110/2009 (H3N2); (d) the calibration curve of PL intensity corresponding on the concentration of the influenza virus A/Yokohama/110/2009 (H3N2). 48

Figure 3.9. (A) ELISA for HA (H3N2) ab82454 antibody-modified NPGL film with recombinant influenza HA (H3N2); (B) ELISA for HA (H3N2) ab82454 antibody-modified QDs with recombinant influenza HA (H3N2). The error bars in A & B indicate SD in each measurement. 49

Figure 3.10. Influenza virus A/Yokohama/110/2009 (H3N2) detection using commercial RIDT. Virus concentrations were 10,000, 5,000 and 1,000 PFU/ml, respectively. A, B, and C denote influenza A virus, influenza B virus, and control, respectively. 50

Figure 4.1. Spectroscopic analysis of CdTe QDs and FMNPs. (A) Absorbance and PL spectra of CdTe QDs; (B) PL spectra of FMNPs and supernatant..... 61

Figure 4.2. Images of TIRF (A) and TEM (B), and DLS (C). Bars in A and B denote 1 μ m and 50 nm, respectively. 62

Figure 4.3. Hysteresis loops of the FMNPs. Magnetic properties of FMNPs and MNPs were measured using SQUID at 300 K. 63

Figure 4.4. Stability of prepared FMNPs at room temperature (A), fluorescence images of FMNPs at different stages (B), and cell viability in the presence of FMNPs (C). The cytotoxicity of the FMNPs was measured using Vero cells by the trypan blue exclusion test. 64

Figure 4.5. ELISA result for Figure 26: antibody conjugated with FMNPs. Anti-FLAG antibody and hCC49 antibody Fab region conjugation was performed on FMNPs. 65

Figure 4.6. Confocal laser scanning microscopy images of cancer cells. Differential interference contrast (DIC) images of LS174T cells with (A), without (B) hCC49 antibody Fab region conjugated FMNPs, and 293 T cells with hCC49 antibody Fab region conjugated FMNPs (C). Merged images of DAPI/Fluorescence for LS174T cells with (D), without (E) hCC49 antibody

Fab region conjugated FMNPs, and 293 T cells with hCC49 antibody Fab region conjugated FMNPs (F).	66
---	----

LIST OF TABLE

Table 1. Comparison of influenza virus A/Yokohama/110/2009 (H3N2) detection using RIDT.	49
---	----

LIST OF ABBREVIATIONS

AAO: Anodised aluminum oxide
AFM: Atomic force microscope
Ag-nNDL: Ag nanoneedle
Au NPs: Gold nanoparticles
BSA: Bovine serum albumin
CdO: Cadmium oxide
CTAB: Hexadecyltrimethyl ammonium bromide
DAPI: 4',6- diamidino-2-phenylindole
DI water: Deionized water
EBL: Electron-beam lithography
EDC: N-(3-dimethylaminopropyl)-N-ethylcarbodiimide
ELISA: Enzyme-linked immunosorbent assay
FMNPs: Fluorescence magnetic nanoparticles
FTIR: Fourier transform infrared spectroscopy
Fab: Fragment antigen binding
FWHM: The full-width at half maximum
HA: Hemagglutinin
HEK293: Human embryonic kidney 293 cell
HRP: Horseradish peroxidase
LbL: Layer-by-layer
LOD: Limit of detection
LED: Light emitting diode
LSM: Laser scanning microscope
LSPR: Localized surface plasmon resonance
MEF: Metal-enhanced fluorescence
MNPs: Magnetic nanoparticles
MFNPs: Multifunctional nanoparticles
MPA: 3-Mercaptopropionic acid
MRI: Magnetic resonance imaging

NHS: *N*-hydroxysuccinimide
NPGL: Nanoporous Gold leaf
NPs: Nanoparticles
NSL: Nanosphere lithography
OA: Oleic acid
ODE: Octadecene
PAA: Polyacrylic acid
PDDA: Poly-diallyldimethylammonium chloride
PFU: Plaque forming units
PL: Photoluminescence
PMMA: Poly (methyl methacrylate)
QDs: Quantum dots
QY: Quantum yield
RIDT: Rapid influenza diagnostic test
 R_{RMS} : Root mean square
SD: Standard deviation
SEM: Scanning electron microscopy
SP: Surface plasmon
SPPs: Surface plasmon polaritons
SQUID: Superconducting quantum interference device
TEM: Transmission electron microscopy
TGA: Thioglycolic acid
TIRF: Total internal reflection fluorescence
TMB: 3, 3', 5, 5'-Tetramethylbenzidine
TOP: Trioctylphosphine
UV: Ultra-violet

ABSTRACT

Fluorescent hybrid nanostructure materials have received substantial attention for their promising performance in nanobio technological applications. A combination of more than one nanocomponent into a hybrid structure gives rise to new collective properties different from the constituents. The hybrid nanostructures not only have multifunctional properties, but also may induce synergistic properties, arising from interfacial particle-particle interactions. Coupling of two or more components produces a hybrid nanostructure that allows electronic transfer across the junction to change local electronic structure. These behaviours make them to generally have potential applications in biomedical methods for biosensing, drug delivery system.

The functional fluorescent hybrid nanomaterials with combined plasmonic-fluorescent or magnetic-fluorescent structures have unique optoelectronic properties for biomedical applications. The optical, electronic, magnetic properties could be controlled by adjusting their sizes, shapes, compositions, and surface chemistry. Several types of the hybrid nanostructures are potentially useful for biomedical applications. For example, the plasmonic-fluorescent materials would be interesting as dual-use biological tags, giving the ability to visualize labeled cells using both magnetic resonance and fluorescence imaging techniques, while external magnetic fields could be employed for the directed assembly of such materials.

In this study, **Chapter one** reviews the design, fabrication, and biomedical applications of the fluorescent hybrid nanomaterials with combined plasmonic-fluorescent and magnetic-fluorescent structures. New collected properties of the hybrid nanostructures arising from the particle-particle interactions and the geometries are discussed from specific results of recent publications. The functionalizations of the hybrid nanostructures with polymer and silica coatings yielded water-soluble nanohybrid colloids are described. The subsequent conjugation of biomolecules with the coated nanohybrids afforded biosensing and the use of them as multimodal bioprobes for multimodal imaging and therapy are highlighted.

Chapter two describes the fabrication of plasmonic metallic film with surface roughness for fluorescent enhancement. Such imperfection or rough surface can cause

substantial losses and significantly reduce the surface plasmon (SP) decoherence time due to scattering of light on it, which is considered to increase radiative decay rates and shorten the fluorescence lifetime. Plasmonic metallic nanostructures have been prepared based on template based fabrication. Surface plasmon-induced emission of organic ZnS-capped CdSe QDs quantum dots (QDs) showed six-fold increase in the fluorescence intensity and striking reduction in fluorescence lifetimes on close proximity of rough Ag nanoneedle compared to the case of smooth surfaces. The methodologies and observations reported in this chapter could be relevant for the design and construction of high-efficiency light-emitting diodes, platform fabrication of biological and environmental monitoring, and high-contrast imaging.

Chapter three describes the biosensing application of plasmonic-fluorescent hybrid nanostructure. In the present study, a rapid, sensitive and quantitative detection of influenza A virus targeting hemagglutinin (HA) was developed using hybrid structure of quantum dots (QDs) and nanoporous gold leaf (NPGL). NPGL film was prepared by dealloying bimetallic film where its surface morphology and roughness were fairly controlled. Anti-influenza A virus HA antibody (ab66189) was bound with NPGL and amine ($-NH_2$) terminated QDs. These biofunctionalized NPGL and QDs formed a complex with the influenza virus A/Beijing/262/95 (H1N1) and the photoluminescence (PL) intensities of QDs were linearly correlated with the concentrations of the virus up to 1 ng/mL while no PL was observed in the absence of the virus, or in bovine serum albumin (BSA, 1 mg/mL) alone. In addition, it was demonstrated that this assay detected successfully influenza virus A/Yokohama/110/2009 (H3N2) that is isolated from a clinical sample, at a concentration of ca. 50 plaque forming units (PFU)/mL. This detection limit is 2-order more sensitive than a commercially available rapid influenza diagnostic test. From these results, the proposed assay may offer a new strategy to monitor influenza virus for public health.

Chapter four describes the preparation and cellular imaging application of new fluorescent-magnetic hybrid nanocomposites based on fluorescent CdTe QDs and Fe_3O_4 MNPs. Hybrid nanostructure were developed by a simple LbL fabrication technique which retains the magnetic and fluorescence properties and also showed good optical properties, decent saturation magnetization. Fragment antigen binding (Fab) region of

hCC49 was conjugated with composites, which was used for specific cancer cell imaging. Fluorescence microscopy showed significant preferential binding of the NPs conjugates by cells and showing the ability of the FMNPs probes for imaging application. Ultimately, it is believed that these particles will provide a new class of multimodal NPs for the complex biologic systems.

Overall this dissertation introduced preparation of fluorescent hybrid nanostructure combined with plasmonic-fluorescent and magneto-fluorescent. Furthermore, this thesis expanded the physical study of plasmon–semiconductor hybrid nanostructure to develop a highly sensitive detection of influenza virus based on exciton-plasmon interaction. Also, bioimaging application of newly prepared magneto-plasmonic hybrid nanostructure has been shown successfully on cancer carcinoma cells. The demonstration of these multifunctional nanocomposites and their properties has stimulated a significant increase in the development of combined detection and treatment strategies in nanobiotechnology field.

CHAPTER I
INTRODUCTION

1. Introduction

1.1 Fluorescent Hybrid Nanostructure

Nanoscale fluorescent hybrid materials are one of the most promising and rapidly emerging research areas in materials chemistry. The ability to selectively arrange nanosized domains of metallic, semiconducting, and magnetic materials into a single hybrid nanoparticle offers an intriguing route to engineer nanomaterials with multiple functionalities or the enhanced properties of one domain. With the advancement of hybrid nanostructures composed of semiconductor and metal components have lead to the creation of new generation of contrast agents and sensing systems. Due to their multiple domains, these nanostructures posses different features and therefore they should be able to perform several tasks in parallel. Their applications are expected to significantly improve the diagnosis and treatment of a variety of diseases [1,2].

Over past decades, a vast number of studies have been devoted to the preparations of various fluorescent hybrid nanostructures, including plasmonic/semiconductor, and magnet/semiconductor ones. Tremendous effort has been made to form (plasmonic metal)/semiconductor hybrid nanostructures to increase the visible-light response of wideband gap semiconductor nanostructures which has recently attracted much attention because of the unique properties of localized surface plasmon resonance (LSPR). The complementary optical properties of plasmonic metal and semiconductor nanostructures make them attractive components for many applications that require controlled flow of electromagnetic energy on the nanometer length scale. When combined into heterostructures, the nanometer-scale vicinity of the two material systems leads to interactions between quantum-confined electronic states in semiconductor nanostructures and dielectric-confined electromagnetic modes in the metal counterparts. Such exciton-plasmon interactions allow design of absorption and emission properties, control of nanoscale energy-transfer processes, creation of new excitations in the strong coupling regime, and increase of optical nonlinearities. With the advancement of novel fabrication techniques, the functionalities of plasmonic metal and semiconductor nanostructures will be further increased for better control of optical properties and energy flows on nanometer length and femtosecond time scales. Those plasmonic/semiconductor hybrid nanostructure has versatile applications in optical biosensor, biotechnology, and solar

energy harvesting field [3-5].

A further important direction for applications of fluorescent hybrid nanoparticles concerns their use as multifunctional biological markers. Considering that engineered multifunctional nanoparticles (NPs) with highly integrated imaging modalities are a key focus area in bionanotechnology that will have a profound impact on molecular diagnosis, imaging, and therapeutics. An example of such multifunctional NPs is fluorescent magnetic NPs that bear two attractive features, fluorescence and superparamagnetism. Therefore, it is conceivable that one single agent to provide imaging in multiple imaging modalities (optical and magnetic) would be of great value to offer more comprehensive diagnostic information and the dynamics of disease progression. Fluorescent magnetic NPs allowing their intracellular movements to be controlled using magnetic force and monitored using a fluorescent microscope. These features could lead to effective multifunctional drug-loaded magnetic NPs that would facilitate increased drug transport rates, mucus penetration, biological separation, protein purification, bacteria detection, and drug delivery and antibiotic efficiency in biofilms and cellular imaging [6-9].

In this review, we focus on recent strategies used to create plasmon/semiconductor and magneto/semiconductor hybrid nanoparticles, present the emergent properties of these multicomponent materials, and discuss their potential applicability in biological sensing and imaging.

1.2 Plasmon/semiconductor hybrid structure and its bio-applications

Fluorescent materials have found widespread application in the life sciences as probes that provide fast and consistent detection of biomolecular interactions in a reliable and reproducible fashion. Regardless of the measurement technique used, the fluorescence intensity produced by a fluorescent probe is of key importance in determining its capability to provide specific detection of materials of interest in the presence of unknown amounts of other substances. Techniques that enhance fluorescence emission can reduce measurement times, increase sensitivity, or reduce the amount of material required for accurate detection. It is well-known that the presence of a metal surface in close proximity to a fluorophore can significantly modify its emission [10]. For example, Lee et al. developed influenza virus monitoring system by interaction between

plasmonic nanomaterials and fluorescent particles. The observed detection limitation was 100-fold higher than that of the commercial diagnostic kit with excellent selectivity. Such system may be applied not only to the influenza virus, but also to various other infectious viruses [11].

Roughness and imperfections in plasmonic metal surface can trap incident light through their surface plasmons and confine it to sub wavelength spaces. For enhanced roughness, multiple scattering of light occurs in nanostructured random media. Such roughness allows surface plasmon polaritons (SPPs) of high momentum to scatter, lose momentum, and then converted to radiated light which ultimately absorbs by fluorophores in metal-semiconductor nanostructure and emit enhanced fluorescence light[12-14]. This phenomenon, known as metal-enhanced fluorescence (MEF), plays a key role in near-field technological applications. Such near-field optics and optical tunneling light-matter interactions has developed into an important subfield of physical optics. It is well known that evanescent waves play a prominent role in near-field optics and in optical tunneling. An evanescent wave cannot exist in the absence of other waves in space. This property makes a theoretical understanding of light-matter interaction in the optical near-field challenging. Research in the field of near-field optics is vitally important for accessing dipole-forbidden transitions which will open up new and exciting frontiers for the field of nanobiotechnology.

Recent years, though a tremendous number of theoretical and experimental investigations have been studies in near-field optics, there are still only few studies dealing with nonlinear aspects. In this paper, we report in detail the application of grating coupled SPP-enhanced fluorescence to surface quantum dots (QDs) instead of fluorescent dyes. QDs have high quantum efficiencies compared to most fluorescent dyes and high resistance to photobleaching, facilitating easier measurement, and increased sample resilience. These properties are accompanied by size-dependent emission spectra and broad absorption bands, which allow for widely separated excitation and emission. The combination of these novel properties has made QDs one of the prime candidates for application to biosensing and nanotechnology. In addition to their favorable optical properties, the larger physical dimensions of these materials enables a much more detailed study of the behavior of surface plasmon coupled fluorescence enhancement on

nanostructured surfaces [15].

The tuning of the plasmonic properties for implementation in different biological applications relies on the design and fabrication of metallic structure. In recent years, there have been tremendous developments in the synthetic control of nanocrystal size, shape, and composition, thus allowing the tailoring of their properties. Zho and co-workers reported a method for the formation of spiky nanoscale particles, which represent some of the interesting non-Platonic, non-Archimedean, non-spherical, concave shapes [16] (Fig. 1.1).

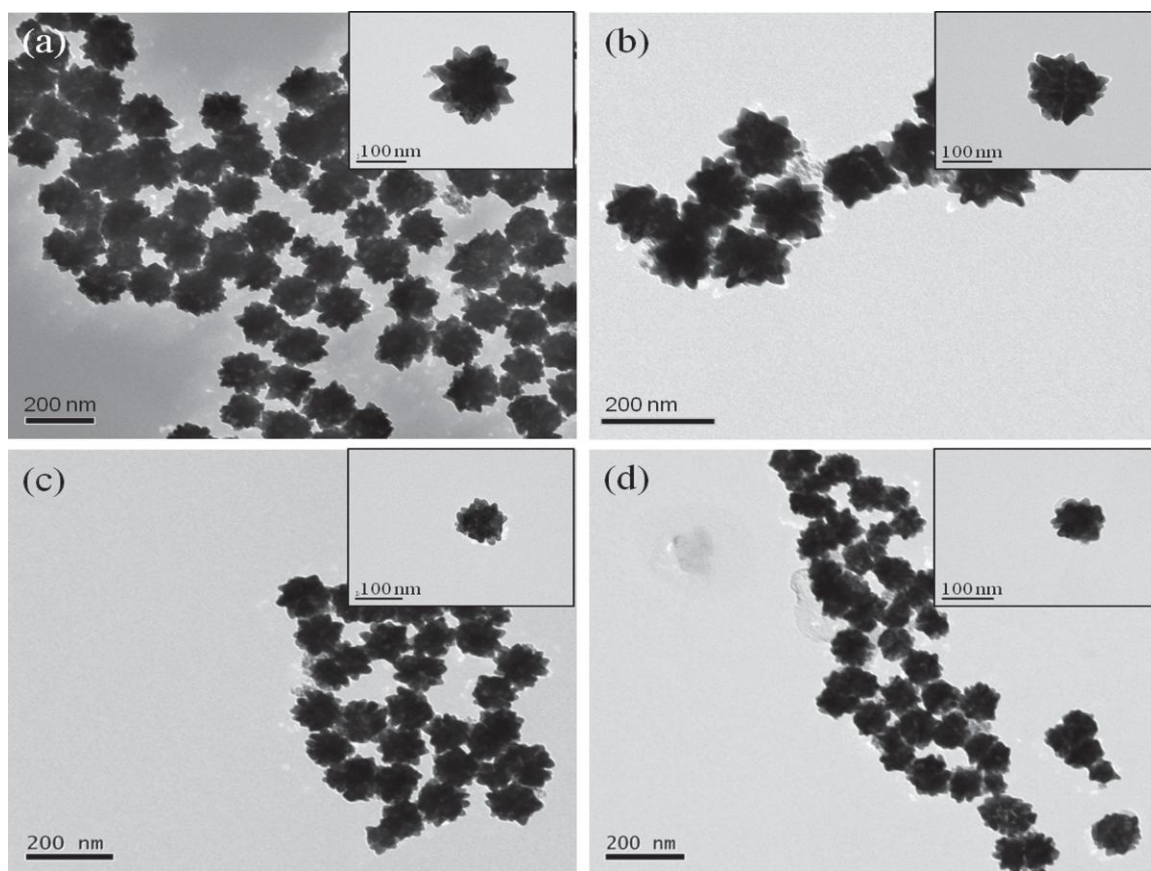


Figure 1.1: TEM images of spiky SPs assembled in the presence of different amounts of smooth Fe_3O_4 @Au core-shell particles: (a) 4.5 nM, (b) 8.9 nM, (c) 13.2 nM, and (d) 17.5 nM. Insets show magnified images of corresponding individual SPs. [Volume of smooth Fe_3O_4 @Au seeds increased from 100 to 400 μL in 100 μL increments for spectra (a)–(d)]. (Reprinted, with permission, from Ref. 16. Copyright 2007 John Wiley and Sons)

Such non-uniform plasmonic metallic surface, patterned on the nano-scale can dramatically modify the optical properties of semiconductor in its vicinity. For example, Yin and Zhu et al. have shown that the multifunctional nanoparticles (MFNPs) composed of gold nanostar@SiO₂@CdTeS quantum dots@SiO₂ nanoprobe showed brightly fluorescence and an enhancement factor of 23 % was realized in MFNPs, compared with the bare QDs. Furthermore, the nanoprobe displays strong fluorescence image of MDA-MB-231 breast cells [17] (Fig. 1.2).

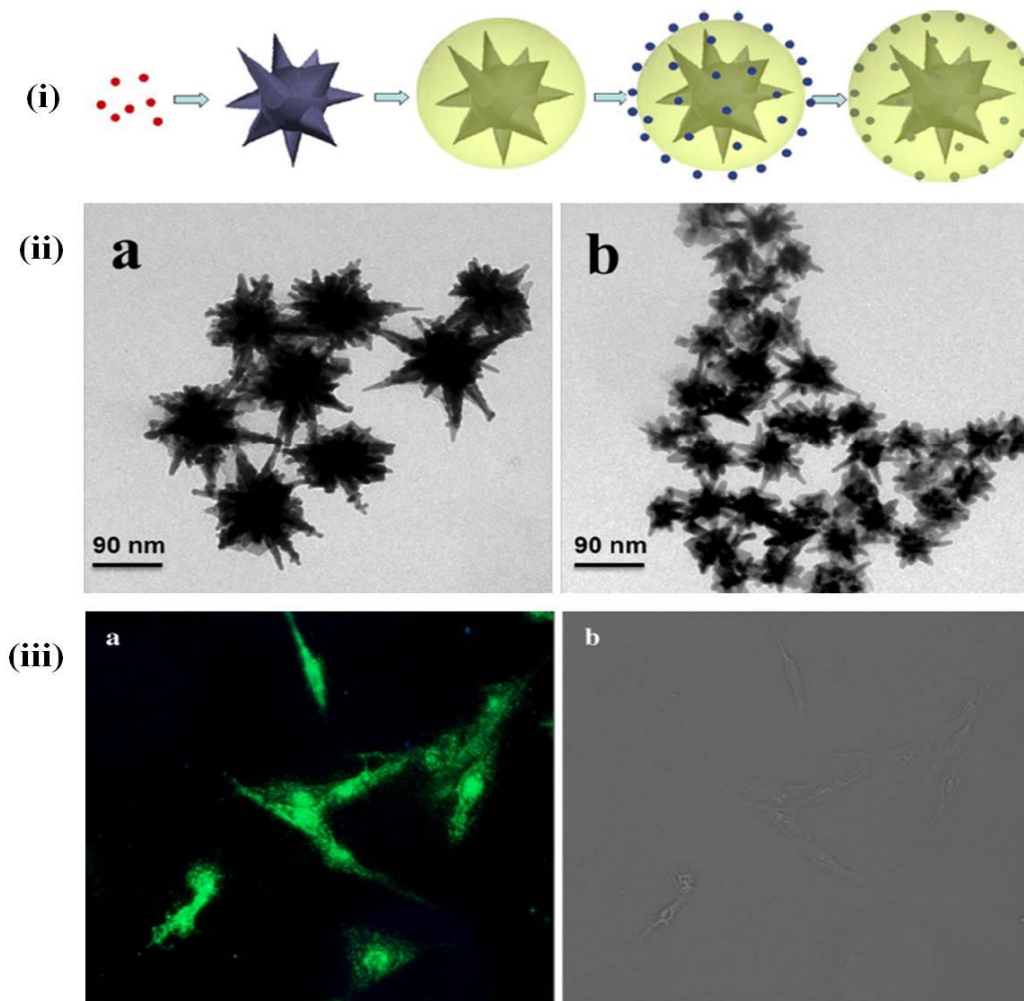


Figure 1.2: (i) Schematic of preparation of the multifunctional gold nanostar/quantum dots doped SiO₂ nanoparticles. (ii) TEM images of gold nanostar with different seed volume a 20 μL, b 100 μL (iii) The fluorescence image of MDA-MB-231 breast cells gained under a UV irradiation and b white light irradiation after the MFNPs were linked onto the breast cells. (Reprinted, with permission, from Ref. 17. Copyright Springer)

Zhou et al. also attained 52% emission enhancement from spiky gold nanoparticles–CdTe NPs conjugation compared with the CdTe NPs during detection of

protein. Such work is unique in terms of optical and biological properties because it involves enhancing the fluorescence of QDs by LSPR of rough-surfaced metallic NPs [18]. Recent work has shown a dramatic enhancement of PL intensity and decay rate of the QDs was achieved on rougher metallic surfaces. The observation of these PL enhancements from nanocomposites was further applied for the development of sensitive influenza virus A (H1N1) detection (up to 1 ng/mL) and influenza A (H3N2) virus at a concentration of ca. 50 plaque forming units (PFU)/mL. Later detection limit is 2-order more sensitive than a commercially available rapid influenza diagnostic test [19].

Silver nano-island films produce by combining slow evaporation and rapid thermal annealing with average diameter of 50 nm. The full-width at half maximum (FWHM) of this distribution is 40 nm whereas the height is centered at 37 nm with a FWHM of 20 nm. The islands have an areal density of $230 \pm 10 \mu\text{m}^{-2}$. From these values we estimate an average inter-island distance of (16.0 ± 0.7) nm. With a 10 nm-thick SiO_2 spacer, the photoluminescence of a layer of CdSe/ZnS colloidal QDs is enhanced on average by a factor of $\eta = 160$ compared to a nominally equal layer on bare quartz [20]. Similar enhanced photoluminescence (PL) intensities (23-fold) and two-fold increased PL decay rates are observed when the QDs are located on evaporated gold films [21]. These techniques however are limited by the inhomogeneity of the island structures and the proportion of fluorophores preferentially placed in relation to the metal to give the enhancement effect.

Nanostructures generated by anodised aluminium oxide (AAO) template can create homogeneous island structures with controllable diameter and length over large area. By a simple patterning and a one-step anodization process this platform could be integrated into microdevices for ultrasensitive fluorescence biological analysis [22]. This shows a cheap ultrasensitive platform that is easily produced and could be applied in single use devices or as a new substrate for MEF structures. For example, Ahmed et al. used metallic Ag nanoneedle films were used for observing luminescence enhancement depending on surface roughness. Structure and roughness of the fabricated sample are predetermined by the structure of the designated template. Fluorescence change was carefully monitored in colloidal CdSe/ZnS coreshell QDs that are resided in the vicinity of two different rough surfaces of Ag nanoneedles, i.e., rough and smooth surface. For

the rough surface, vertically aligned Ag nanoneedles (Ag-nNDL) with lengths of a few hundred nanometers and diameters of approximately 50 nm were used as substrates. Meanwhile, a thermally coated Ag substrate was used as the smooth surface. Observed changes include a six-fold increase in the fluorescence intensity and striking reduction in fluorescence lifetimes of CdSe/ZnS QDs on rough Ag nanoneedle compared to the case of smooth surfaces [12].

The progress in the nanofabrication methodologies has revived the study of surface plasmons, which are considered for wave guiding in the nanoscale. Nanofabrication methods offer organizing plasmonic structures into arrays. Direct-write techniques such as electron-beam lithography (EBL) can fabricate linear and 2D arrays of nanoparticles with different spacings, which typically need to be on the order of the size of the particle or less (<200 nm) for efficient dipolar coupling. Zin and co-workers has been fabricated Au nanoarray using EBL and reported 15-fold increase in surface plasmon-enhanced fluorescence from hybrid nanoassemblies of Au nanoarray-QDS based on biomolecules. Such a synergetic combination of inorganic nanostructures, peptidemediated assembly, and lithographic patterning should enable the precise control necessary to produce highly integrated multifunctional hybrid nanoassemblies for a diverse range of nanobiotechnological applications [23].

Focused ion beam milling has been the most common method for fabricating hole and slot structures in optically thick metal films. This method can drill completely or partially through the film and can control the diameter and spacing of the structures with reasonable precision (approximately 100 nm). Figure 1(a) schematically illustrates a plasmonic meta-material combined with QDs. The metamaterial arrays with a total size of $40 \times 40 \mu\text{m}$ each were fabricated by focused ion beam milling in a 50nm-thick gold film on a glass substrate. Hybridized semiconductor quantum dots with plasmonic metamaterial leads to a multi-fold intensity increase and narrowing of their photoluminescence spectrum resulting [24]. Free-standing suspended films have also been fabricated by focused ion beam milling and reactive ion etching, but the generation of multilayered metal films is difficult and laborious. However, new types of nanofabrication tools, based on soft lithography, can generate a wide range of plasmonic structures with exceptional optical properties. There are two important features of these

techniques: (a) They provide a scalable and inexpensive approach for creating arrays of complementary metal structures (nanoholes and nanoparticles), and (b) they expand the types of plasmonic metamaterials that are possible because the metal building blocks can now be organized over multiple length scales and over macroscale areas. Mulvaney and co-workers demonstrated a simple, robust and flexible procedure to generate 2D ordered arrays of QDs by (i) generating metallic Island with a thickness of around 30 nm via nanosphere lithography (NSL) (ii) using bifunctional alkanes to build a self-assembled monolayer of a chemical linkers on the island and then (iii) deposition core-shell CdSe@Zns QDs to form 2D arrays with tunable luminescence. Confocal microscopy measurements yielded a clear fluorescence image of the hexagonal arrays, proving the presence of QDS organized on the metallic island. This periodic array can be scaled from 100 nm to 5 μm with relative ease: the NSL masks can be replicated, scale-up to macroscopic area is feasible [25] (Fig. 1.3).

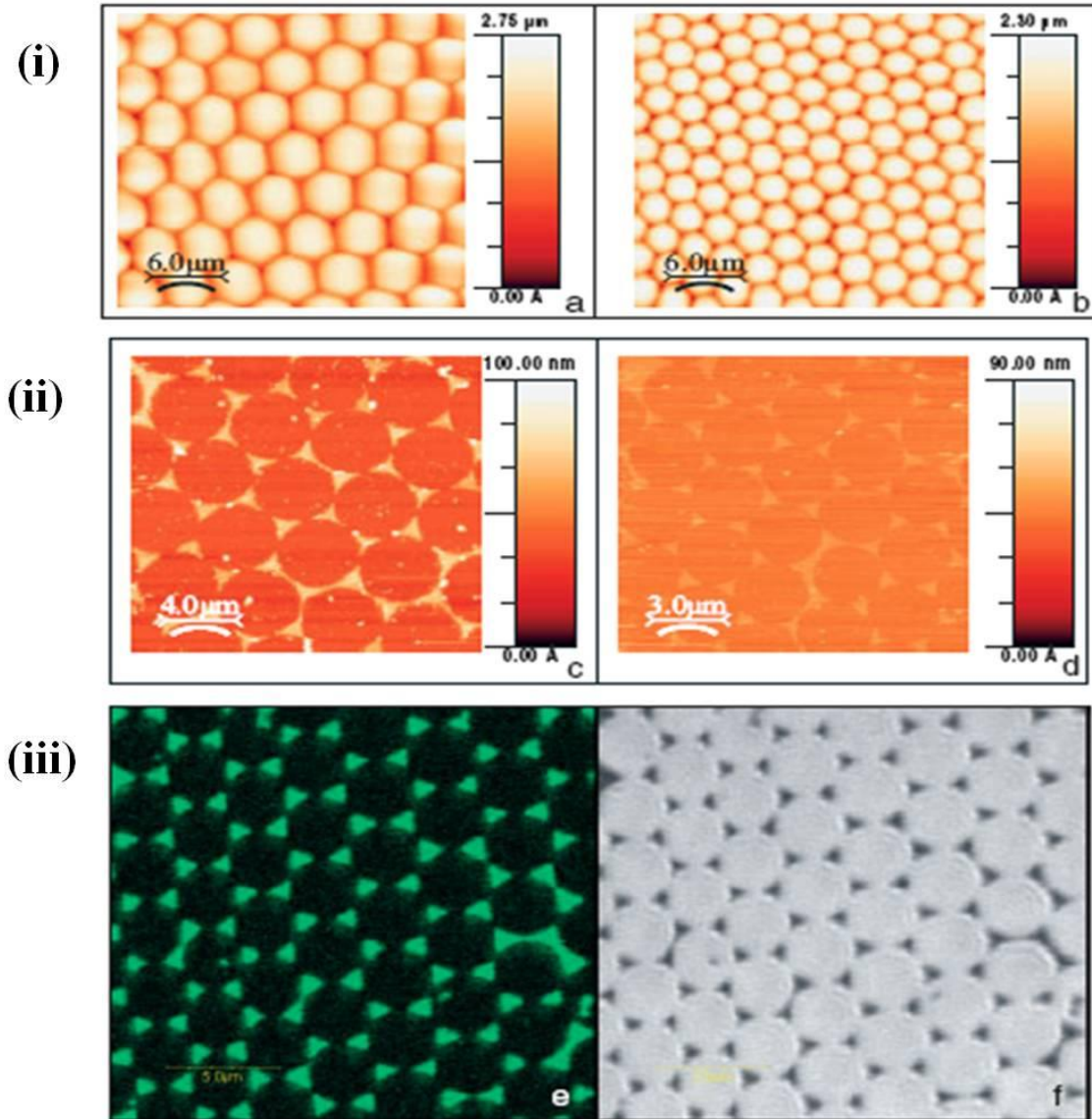


Figure 1.3: 30μm×30μm tapping-mode AFM images of ordered PS particles (a) 20 μm×20μm tapping-mode AFM images of silver arrays made with a latex mask of PS particles 4.9μm in diameter. (d) 15μm×15μm image of arrays made with a latex mask of PS particles 3.2 μm in diameter. (e,f) Fluorescence and optical images, of a single CdSe@ZnS hexagonal array made with a 3.2 μm particles diameter PS mask. (Reprinted, with permission, from Ref. 25. Copyright John Wiley and Sons).

1.3 Magneto/semiconductor hybrid structure and its bio-applications

The inclusion of fluorescence and magnetic nanoparticles in nanoscale entity offers further important direction of fluorescent hybrid nanostructures concerns their use as multifunctional nanomedical platforms for multimodal imaging or simultaneous diagnosis and therapy [7,8]. Considering that semiconductor quantum dots have already emerged as a fluorescent probes with increased applications for cell labeling, biosensing, in vivo imaging [26-28] and magnetic nanoparticles that are nontoxic and biodegradable, play an increasingly important role in science and technology, i.e., in biology and medicine for imaging, cell tracking, magnetic separation and bio- and chemo-sensing [29-35]. So, combined structure with both functionalities on one hybrid nanoparticle presents a powerful approach with potential implications for medical diagnostics. A specific difficulty in the preparation of magnetic /fluorescent nanostructures is the risk of quenching of the fluorophore on the surface of the particle by the magnetic core. In addition, if there are a number of fluorescent molecules attached to the surface of the particle, they may act to quench each other. Non-radiative transfer has been blamed for the quenching of fluorescent molecules when attached to magnetic nanoparticles. This quenching process is believed to occur because of fluorophore contact with the metal oxide particle surface, resulting in an energy transfer process. The problem of quenching can be partially resolved by providing the magnetic nanoparticle with a stable shell prior to the introduction of the fluorescent molecule, or by first treating the fluorophore with an appropriate spacer [9]. In this review, we intend to highlight the advances and developments that have occurred over last decade for magnetic/quantum dots hybrid structure for biological applications.

In the last decade the field of NPs with combined magnetic and fluorescent properties has more and more become a fast evolving branch of science with an exponentially increasing number of new developments per year. A lot of effort has been given to combine magnetic and fluorescent nanoparticles into one nanoprobe by covalent/coordination chemistry, in combination with assembly methods, by epitaxial growth, or by including both species into a matrix from silica, polymer or oil droplets and liposomes, and numerous publications report about further functionalization of the resulting magnetic and fluorescent NPs [6,] (Fig 1.4), for *e.g.* biomolecular targeting or

with therapeutic agents.

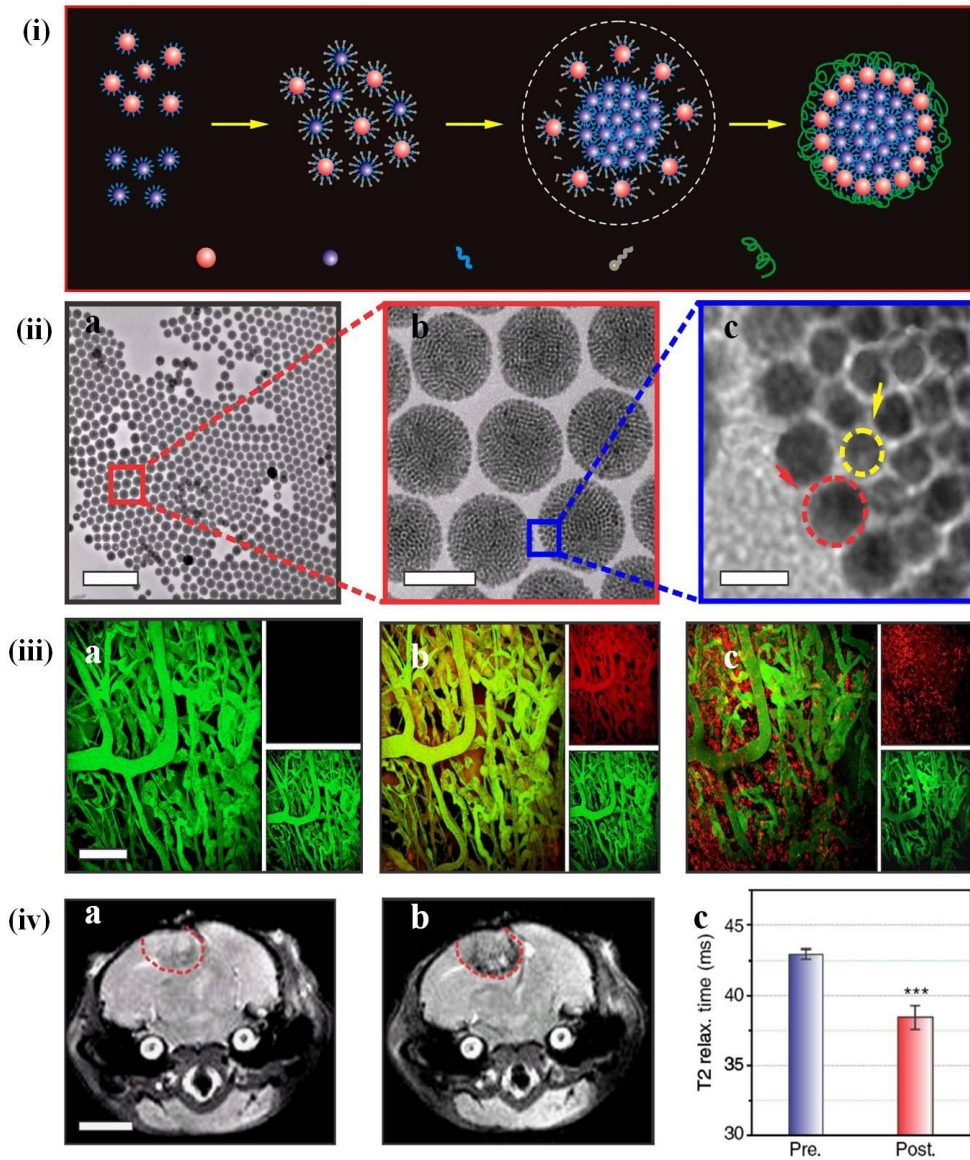


Figure 1.4: (i) Schematic of the formation of the CS-SPs. (ii) A set of TEM images of CS-SPs at different magnifications. Scale bars, 500 nm, 100nm and 10nm ((a–c)), respectively.(iii) Intravital multiphoton microscopy through the cranial window was carried out at different time point: pre-injection (a), 4 h post injection (b) and 24 h post injection (c). Scale bar, 150 mm. Images from red and green channels are shown in small panels (top: red channel, bottom: green channel). Green emission signals are generated from a blood vessel tracer and red emission signals are generated by mPEG-functionalized silica-CSSPs. In vivo T2-weighted magnetic resonance images of pre- (h) and 24 h post- (i) injection of mPEG-silane functionalized silica-CS-SPs. Twenty four hours post-injection image show clear tumour visualization (denoted by the red dash line). Scale bar, 3 mm. (j) The corresponding T2 relaxation (relax.) time fitting results for the tumour region at time points of pre-injection (Pre., blue bar) and 24 h post injection (Post., red bar). (Reprinted, with permission, from Ref. 6. Copyright Nature Publishing Group).

The area of fluorescent-magnetic nanocomposites is still very much in its developing stage, making the classification of these materials difficult and quite arbitrary. Fluorescent-magnetic hybrid nanostructure preparation have so far been successful with different coating agents, e.g., silica [36-39], oil droplets [40] and vesicles [41], as well as polymer matrices [42-46]. Most of these nanocomposites are further functionalized and applied for imaging or sensing applications. For example, Sun et.al, prepared a new kind of magnetic, fluorescent multifunctional nanoparticles (~ 30 nm in diameter) was demonstrated, where multiple fluorescent CdTe quantum dots (QDs) are covalently linked to and assembled around individual silica-coated superparamagnetic Fe_3O_4 nanoparticles and active carboxylic groups are presented on the surface for easy bioconjugation with biomolecules. The $\text{Fe}_3\text{O}_4/\text{CdTe}$ magnetic/fluorescent nanocomposites conjugated with anti-CEACAM8 antibody were successfully employed for immuno-labeling and fluorescent imaging of HeLa cells [37](Fig. 1.5).

To prepared hybrid nanostructure of fluorescent and magnetic NPs, various techniques, such as co-precipitation methods [46], ultrasonic emulsification [45], miniemulsion/emulsion polymerization [44], and co-embedding of both NP types into temporarily swollen poly(styrene/acrylamide) copolymer nanospheres [47] were applied. An additional method for preparing the fluorescent and magnetic NPs inside polymeric nanoobjects using layer-by-layer self-assembly technique due to oppositely charged building blocks of polymers [48]. With a flow channel system and a local magnetic field gradient the magnetism induced trapping of the magnetic and fluorescent polymer capsules was monitored by fluorescence microscopy [49].

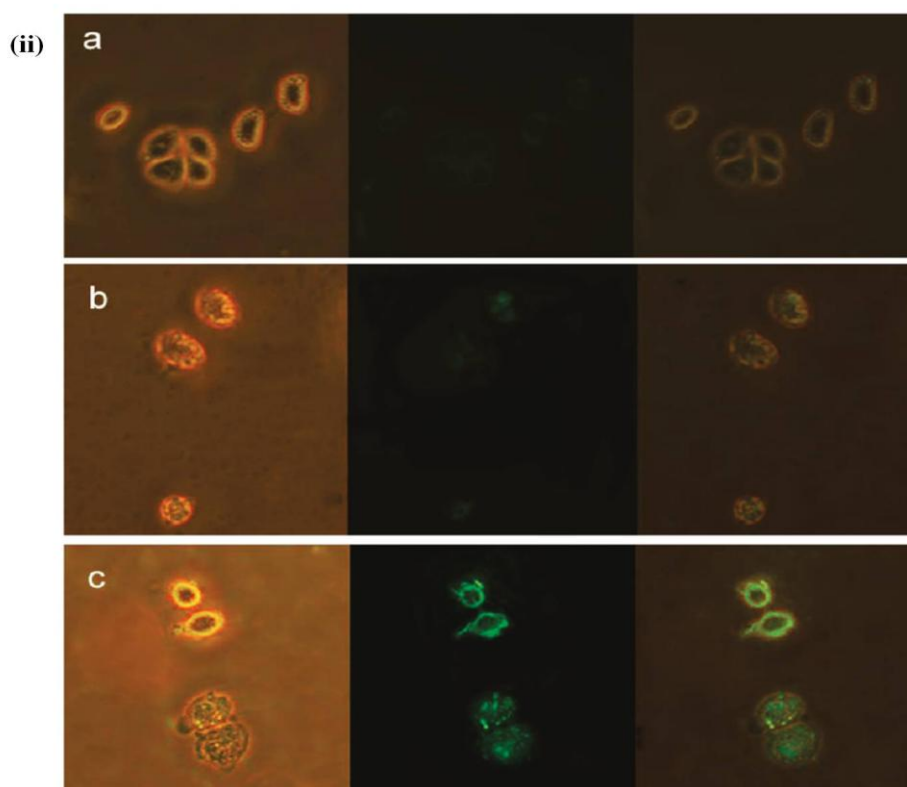
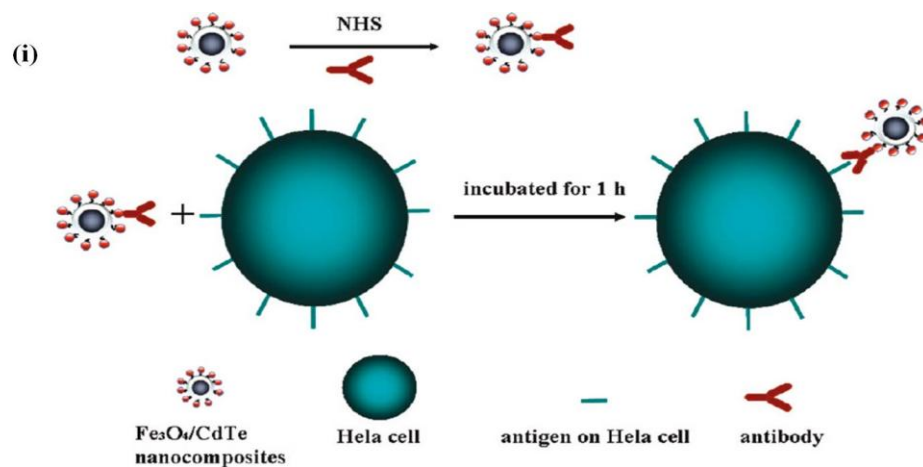


Figure 1.5: (i) Schematic illustration of immuno-labeling using $\text{Fe}_3\text{O}_4/\text{CdTe}$ nanocomposites which are formed by linking multiple TGA stabilized CdTe QDs with the thiol-functionalized silica-coated iron oxide nanoparticles. (ii) Images of live HeLa cells (a) without interacting with any nanoparticles, (b) directly labeled by $\text{Fe}_3\text{O}_4/\text{CdTe}$ nanocomposites without antibody conjugated, and (c) immuno-labeled by $\text{Fe}_3\text{O}_4/\text{CdTe}$ nanocomposites conjugated with anti-CEACAM8. In the three panels, the left columns represent the phase-contrast images, the center columns represent the fluorescent images, and the right columns are the overlays of the left and center columns. (Reprinted, with permission, from Ref. 37. Copyright 2007 Wiley-VCH Verlag GmbH & Co. KGaA).

An interesting magnetic and fluorescent nanosystem describes the assembly of quantum dots onto magnetite nanorings [50]. In this synthesis route, electrostatic interaction between positively charged poly(ethylene imine) capped highly luminescent CdSe/ZnS quantum dots and citric acid functionalized nanorings was exploited to induce the assembly. Alternatively, magnetic fluorescent NPs have been developed exploiting *in situ* chemical synthesis methods [51-54]. Vargas and co-workers, for example, have synthesized Fe₃O₄/ZnSe nanoparticles (NPs) composite nanocrystals. The 7 nm core/3 nm shell NPs show good magnetic and photoluminescence (PL) responses (Fig. 1.6). By comparing the magnetic properties of Fe₃O₄ NPs and the core/shell Fe₃O₄/ZnSe NPs, authors have found the enhancement of the energy barrier in the core/shell composite NPs. This effect directly modifies the relaxation time, which is of fundamental interest to biomedical applications [55].

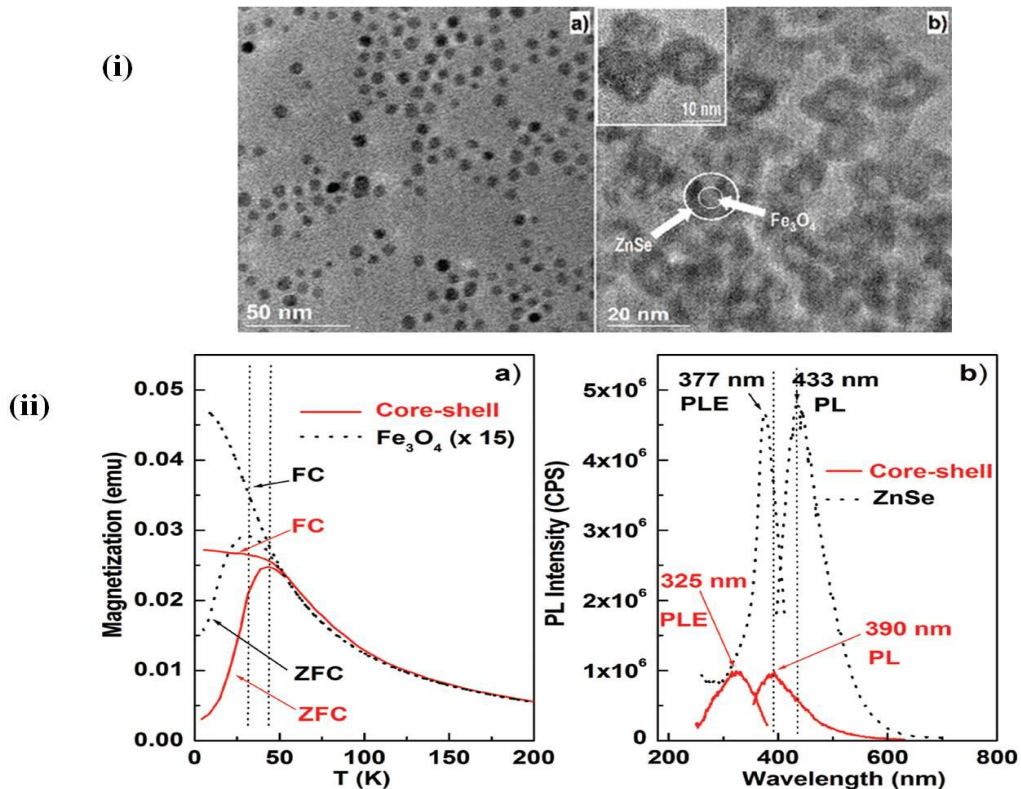


Figure 1.6: (i) TEM image of (a) reference Fe₃O₄ NPs and (b) core/shell Fe₃O₄/ZnSe NPs. (ii) (a) Magnetization against T under ZFC and FC conditions for the reference Fe₃O₄ and core/shell Fe₃O₄/ZnSe NP samples. (b) PLE and PL spectra measured at room temperature for the reference ZnSe and core/shell Fe₃O₄/ZnSe NP samples. (Reprinted, with permission, from Ref. 55. Copyright AIP Publishing LLC).

We have shown that a lot of progress has been achieved already in preparing of magnetic and fluorescent nanoobjects of different varieties over recent years. There is a great need and demand for these materials. From above discussion, it is clear that magnetic-fluorescent nanocomposites offer new approaches and opportunities in chemistry, biology and medicine. However, despite of all recent progress made, the fluorescent-magnetic nanocomposite area is still in its infant stage and significant efforts are needed for further development of these materials and their utilization in real life applications.

1.4. Conclusion

The interface between materials science and biology has been a fertile research area to not only advance our fundamental knowledge of biomaterials, but also create novel hybrid nanomaterials with practical applications. Recent development in nanotechnology has revealed a variety of hybrid nanostructure with unique size- and shape-dependent physiochemical properties. However, to create hybrid bio-nanomaterials for practical applications, control over the fabrication of nanomaterials with well tailored shapes and properties should be achieved. Also, for sensing and imaging applications, the nanomaterials should be engineered to acquire target recognition abilities for selective targeting, labeling and signal transduction. In this review chapter, we have presented the potentiality of fluorescent hybrid nanostructure preparations based on plasmonic NPs, Quantum dots (QDs) and magnetic NPs. These nanostructures benefit from several advantages: their magnetic and optical properties can be tuned through size, shape and composition engineering, their efficiency can exceed by several orders of magnitude that of contrast agents clinically used, to make supersensitive sensor for diagnosis, their surface can be modified to incorporate specific targeting agents and they can possibly be integrated in complex architecture to yield multi-modal imaging agents.

CHAPTER II
PHOTOLUMINESCENCE ENHANCEMENT ON
QUANTUM DOTS/Ag NANONEEDLES HYBRID
NANOSTRUCTURE

2.1. Introduction

The need for near-field optics has increased tremendously because of the fabrication of metallic nanostructures with tunable surface morphology, allowing unprecedented control over electronic, optical, and mechanical properties [3,56-62]. Physical and chemical properties of metallic nanostructure are drastically different from those of the bulk solid. This is manifested by a high energy, increased number of defect sites, distinctive electronic state, altered surface crystal structure, and strong absorption at specific wavelength. As a result of these unique features, the metal surface plays a key role in near-field technological applications. In particular, silver film has been frequently employed because of its intrinsic properties such as low contact resistance and low refractive index. Prominent optical nanostructures include composite structures of semiconducting nanocrystals on these metallic surfaces, which allow us to induce highly efficient emission via excitations in strong coupling regime. In particular, the interfaces are essential in the optical response of semiconductor nanocrystals on metals, where coupling between plasmonic energy and exciton develops [3,58]. This coupling develops new aspects of nanocomposite material systems, inducing many applications that require delicate control of electromagnetic energy in the nanoscale range. For example, Gomez et al. used planer Ag thin film to study the regime of strong light-matter coupling in semiconductor nanocrystals. The demonstration of room-temperature strong coupling involving surface plasmons (SPs) and colloidal quantum dots (QDs) has important practical used of all - optical nonlinear devices, threshold less laser operation, single-photon optical transistors and spacers (surface plasmon amplification by stimulated emission) that rely on optimizing nanoscale light-matter interaction. Gryczynski et al. studied surface plasmon-coupled emission of semiconductor QDs on a glass slide covered with 50 nm of silver and a 5-nm protective SiO₂ layer. This might also lead to applications in biological detection, optical coatings, and nanoelectronics [63,64]. However, most research was related to thin metallic film. Very few researches have dealt with the relationship between surface roughness and Plasmon induced photoluminescence (PL) enhancement, even though the roughness of the metallic surface should be a crucial factor for effectively manipulating the interaction between metallic and semiconducting materials in nanoscale devices [65-73]. Therefore, in this paper,

metallic Ag nanoneedle films were used for observing luminescence enhancement depending on surface roughness. Structure and roughness of the fabricated sample are predetermined by the structure of the designated template. Fluorescence change was carefully monitored in colloidal CdSe/ZnS coreshell QDs that are resided in the vicinity of two different rough surfaces of Ag nanoneedles, i.e., rough and smooth surface. For the rough surface, vertically aligned Ag nanoneedles (Ag-nNDL) with lengths of a few hundred nanometers and diameters of approximately 50 nm were used as substrates. Meanwhile, a thermally coated Ag substrate was used as the smooth surface. It is probable that the relation between surface roughness and PL enhancement will be a valuable factor to develop further photonic and electronic devices in nanoscale regime.

2.2. Experimental Details

2.2.1 Methods

Cadmium oxide (CdO, 99.99%), selenium (99.5%, powder), sulfur (99%, powder), 1-octadecene (ODE, 90%), zinc acetate (99.99%), oleic acid (OA, 90%), trioctylphosphine (TOP, 90%), poly(methyl methacrylate) (PMMA), and chloroform (99.8%) were purchased from Aldrich (Sigma-Aldrich Corporation, St. Louis, MO, USA). All the chemicals were used as received, without further purification.

2.2.2 Preparation of thermal-coating substrate and Ag-nNDL

A smooth Ag layer was prepared on Si wafer by thermal coating. A thermal evaporator (Thermal Co-evaporator, GEORIMTECH, Daegu, Korea) was utilized at the condition of $<1.3 \times 10^{-3}$ Pa and supplying voltage of 0.55 V. Then, it generated 300 nm of thin Ag layer on the substrate. The coated substrate was stored in a desiccators (<30% humidity) before further polymer- and QD-coating process. To produce rough surface, evaporation of silver on the porous template was performed as reported elsewhere [74]. Anodized aluminum oxide (AAO/Al; Nextron Inc., Seoul, Korea) membranes were used as templates; the length and pore size of the AAO membrane were 50 μm and 80 nm, respectively. The prepared AAO membrane was cleaned sequentially in ethanol and deionized water, and then mounted on a thermal evaporator. Evaporation of Ag wire

(99.999%) was carried out in a high-vacuum atmosphere ($<1.3 \times 10^{-3}$ Pa). The membrane was dissolved with NaOH (2 M) solution at 40°C for 24 h. Then, the residual Ag film was cleaned carefully using ethanol and deionized water. A Si wafer plate was attached to the rear side of the film for easy handling.

2.2.3 Synthesis of CdSe/ZnS QDs

As with a typical synthetic procedure based on the previous reference [75], 0.05 mmol cadmium oxide and 2 mmol zinc (acetate)₂ were dissolved in a mixture of 3.5 mL oleic acid (OA) and 8 mL 1-octadecene in a 50-mL round flask. The solution was degassed and purged with N₂ for 30 min, heated to 180°C to obtain a pale yellow solution, and then cooled to 100°C, at which the reaction solution was degassed for 20 min. Then, the reaction mixture was further heated to 300°C, yielding a clear solution of Cd(OA)₂ and Zn(OA)₂. At the elevated temperature of 300°C, 0.1 mmol Se and 1.5 mmol S, both dissolved in 1.5 mL trioctylphosphine, were swiftly injected into the hot solution, and the color of the solution turned light red immediately. Continuous heating at 310°C for 10 min allowed the QDs to emit green color of fluorescence.

2.2.4. QD coating on the smooth and rough substrates

Before the coating process, the Ag-nNDL film was cleaned carefully by sequential treatment with ethanol and deionized water to remove any organic residues. Then, it was dried gently by filtered N₂ gas under ambient conditions. Colloidal CdSe/ZnS QDs were first dissolved in chloroform to obtain a dilute solution (approximately 1.4×10^{-10} M). To serve as a spacer between the Ag film and the QDs, a 1% solution of PMMA in toluene was spin-coated onto two different Ag films at 4,000 rpm for 40 s and cured at 60°C to create a thin layer. The root mean square of roughness, R_{RMS} , of the respective films was calculated in at least five different areas of $10 \times 10 \mu\text{m}$. From the surface morphological images of atomic force microscopy (AFM; Veeco Instruments Inc., Plainview, NY, USA), the R_{RMS} of each sample, i.e., smooth and rough substrates, were 1.8 ± 0.12 nm and 39.7 ± 1.08 nm, respectively. The polymer coating process allows the QDs to be associated with plasmon resonance while preventing

luminescence quenching due to charge transfer between the QDs and the Ag surface [76]. Then, the 100 μ l QD solution was spin-coated over the PMMA thin film at 4,000 rpm for 40 s at room temperature.

2.2.5. Optical and microscopic measurements

To measure the absorbance of the QDs on the Ag-nNDLs, the absorbance reflection mode was utilized in UV-visible (UV-vis) spectroscopy (SCINCO S-3100, SCINCO Co., Ltd., Seoul, Korea). The PL enhancements of the samples were measured by a fluorescence spectrophotometer (Model No. F-7000, Hitachi, Tokyo, Japan) when the angle of incident light was 45°. Fluorescence lifetimes (τ) of the respective samples were measured at a 380-nm excitation wavelength using a light-emitting diode (LED; PTI Inc., Oakland, CA, USA). Note that this wavelength is similar to the wavelength of the surface plasmonic field of individual Ag-nNDLs, which would enhance the signal-to-noise ratio of the gathered fluorescence from the QDs deposited on the Ag substrate. Possible spurious scattering of light was blocked by installing optical filters and slits that are as narrow as possible. Topographic images of Ag-nNDL surfaces were obtained using AFM (diInnova, Veeco, USA) and scanning electron microscopy (SEM; Hitachi-S4700, Japan).

2.3. Results and discussion

2.3.1 SEM & AFM Images of Ag-nNDL film

Topographic observation of Ag-nNDL film Figure 2.1 shows morphologies of the smooth and rough Ag films, i.e., thermal-coated and nNDL substrate. The conical end shapes of the Ag-nNDL were arrayed in an average distance of 350 nm. The shapes and sizes of the needles were relatively regular and ordered in a large area (over a few micrometers). The needle diameter was 50 ± 1.25 nm, which is smaller than the pore size of the AAO. The average length of the Ag-nNDLs was about 197 ± 4.03 nm. The end shape of each nanoneedle was not regular since Ag needles were fabricated while the AAO entrance was being blocked. Normally, the size and shape of the metallic end are

dominant factors affecting the plasmonic enhancement of fluorescent materials, particularly in a single-NP-level experiment [77,78]. However, in our experiments, many QDs were coated on the Ag-nNDLs with no order. This reduced the size and shape effects but show collective optical response of total enhancement from many irregularly coated QDs on the metallic surface, truly by roughness effect. The R_{RMS} was observed from topographic images obtained by AFM tapping mode (Figure 2.1C, D). The R_{RMS} of the smooth surface was about 1.8 ± 0.12 nm, whereas the other R_{RMS} was 39.7 ± 1.08 nm. It indicates that the particle size and distribution were relatively uniform for the smooth surfaces. However, the surface topography was quite irregular, and the size distribution was uneven when the Ag-nNDLs were grown. The insets in Figure 8C, D show the depth profiles along the solid lines, respectively. The average height of the smooth Ag surface was approximately 6 nm, while for the rough surface, it was measured at 100 ± 2.62 nm on average. This was slightly lower than the measured length determined from the SEM image, which might be due to detection allowance of the tapping mode in AFM.

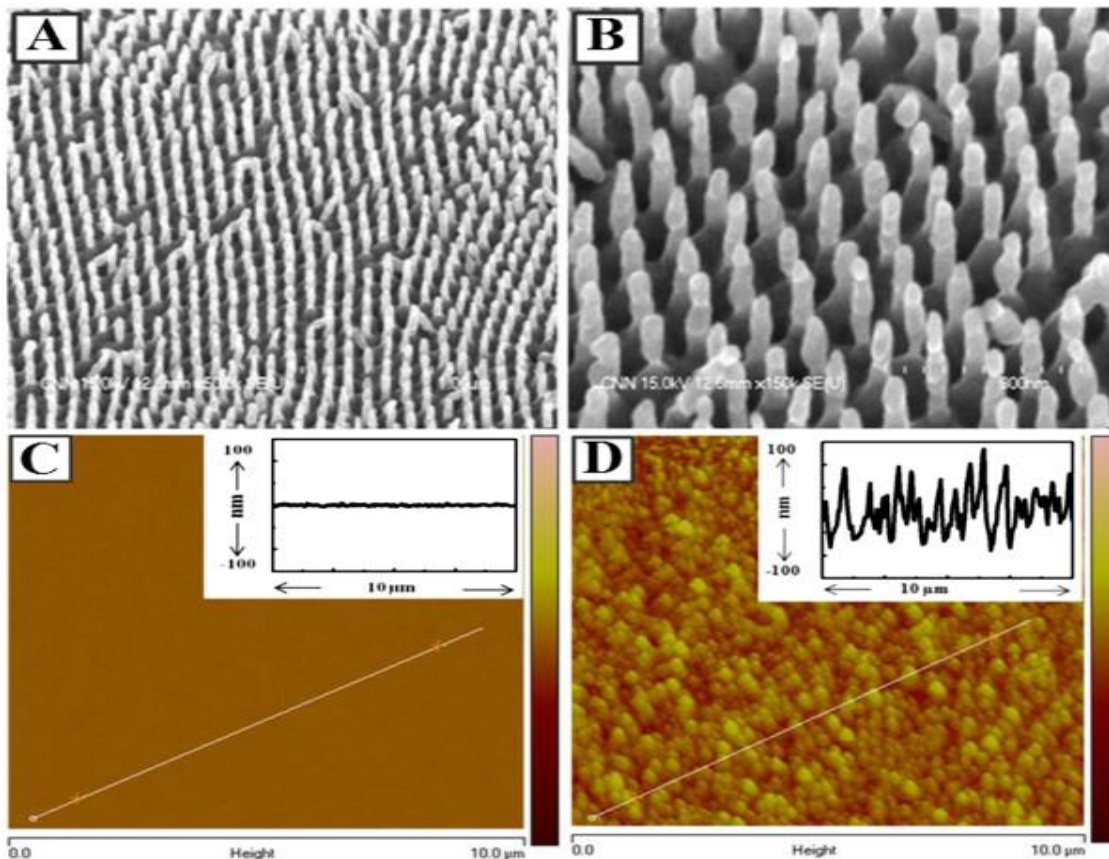


Figure 2.1. SEM images of Ag-nNDLs at $\times 50,000$ (A) and $\times 150,000$ (B). Topographical AFM images of Ag films: (C) smooth Ag substrate and (D) rough Ag-nNDLs. Insets show the depth profiles along each line.

2.3.2. QD coating on smooth and rough substrates

Figure 2.2 presents the surface morphology of the smooth and rough surfaces after QD-coating processes as described in the ‘Methods’ section. The sequential coating of polymers and QDs showed a well-distributed surface on both Ag surfaces, respectively. In Figure 2.2A, most QDs were well dispersed on the smooth Ag substrate, which may decrease the quenching of PL by aggregation. In Figure 2.2B, most QDs were scanned on top of the Ag-nNDL where deep-area scanning by AFM imaging may be limited. It is probable that the aggregation of QDs on the rough surface was also minimized due to a surface area larger than the smooth one.

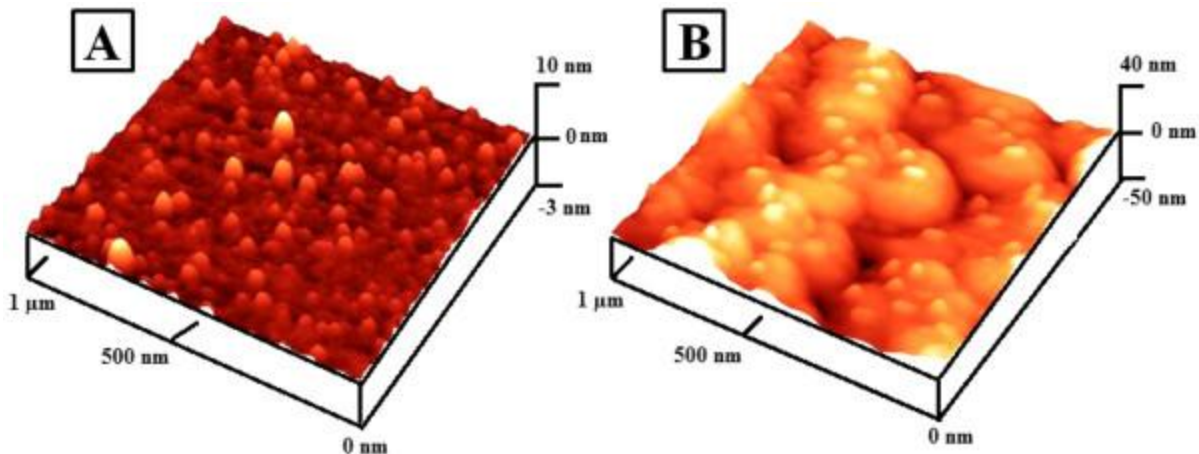


Figure 2.2: AFM images of smooth (A) and rough (B) substrate after QD coating.

2.3.3. Spectroscopic study of QDs on Ag substrates

Figure 2.3A shows typical absorption and PL spectra of the synthesized CdSe/ZnS QDs. The absorption spectrum of QD was shown with the highest peak at 450 nm, and the fluorescence band was very narrow at 100 nm, with a quantum yield (QY) of >20%. The quantum yield was measured by the relative ratio against rhodamine dispersed in ethylene glycol (its QY as 0.95). Figure 2.3B illustrates the typical UV–vis spectra of the smooth and rough Ag-nNDLs. Absorption spectra of the prepared substrates were measured in the reflection mode. For the smooth substrate (image in Figure 2.1C), the UV spectrum revealed an absorption maximum (λ_{max}) at 360 nm, which corresponded to the plasmon band of Ag nanomaterials because the thermally coated layer was approximately 300 nm. For the rough substrate, λ_{max} showed a bathochromic shift from 360 to 420 nm with a plateau region. The shift would be crucial to affect PL enhancement of the deposited QDs by plasmonic coupling. Since the roughness of the produced films was different, special care was required in the QD-coating process in order to deposit the same amount of QDs on each substrate. In the coating process, the absorbances of QDs on the surface of the respective substrates were monitored to maintain similar intensities since absorbance corresponds to PL intensity. The absorbance was monitored by UV–vis spectroscopy after QD deposition on the surface of each substrate (Figure 2.3C). The absorbance difference between two substrates after QD deposition was about 0.07 at the wavelength of 380 nm where the QD was excited.

Fluorescence intensity of the QD at this absorbance difference was monitored in solvent state. The PL spectra in Figure 2.3D showed a small difference in the PL intensity between the two substrates, from which it is probable that similar amounts of QDs were deposited on the respective substrates, and these results can be comparable to the striking PL intensity variance of QDs depending on the different roughness of substrates in Figure 2.4A. Figure 2.4A shows the PL spectra obtained for CdSe/ZnS QDs on the two different Ag substrates at the excitation wavelength of 380 nm. A dramatic enhancement in the PL intensity from the QDs on the rough surface of Ag-nNDLs was observed. About six-fold enhancement was observed compared with the PL intensity on the smooth surface. It is probable that the huge PL change stems from the different surfaces, i.e., the roughness difference or the aggregation control of the deposited QDs. First, such aggregation on the substrate may induce a decrease in the PL intensity. In the evaporation step after coating, the distance between the QDs decreased, and dipole-dipole attraction was more pronounced than charge-charge repulsion. Furthermore, the continuous surface tension during the evaporation forces the congregation of QDs into localized areas. However, on the rough surface, aggregation can be dramatically avoided because of the extremely large surface area. The physical barrier of the Ag-nNDLs decreases the surface tension energy, which may induce fast solvent evaporation after coating. These factors should limit the movement of QDs on the surface, with respect to gathering in a localized area. However, the avoidance of aggregation would not be the main factor for PL enhancement because most of the aggregation was intentionally avoided during the coating process by adjusting the concentration of deposited QDs. Furthermore, note that the detailed imaging of AFM proved less aggregation in Figure 8. When similar amounts of QDs were deposited on the respective substrates, the intensity difference between them was very small, which may strongly support the vital role of the plasmonic rough surface in enhancing fluorescence emission Figure 2.3D.

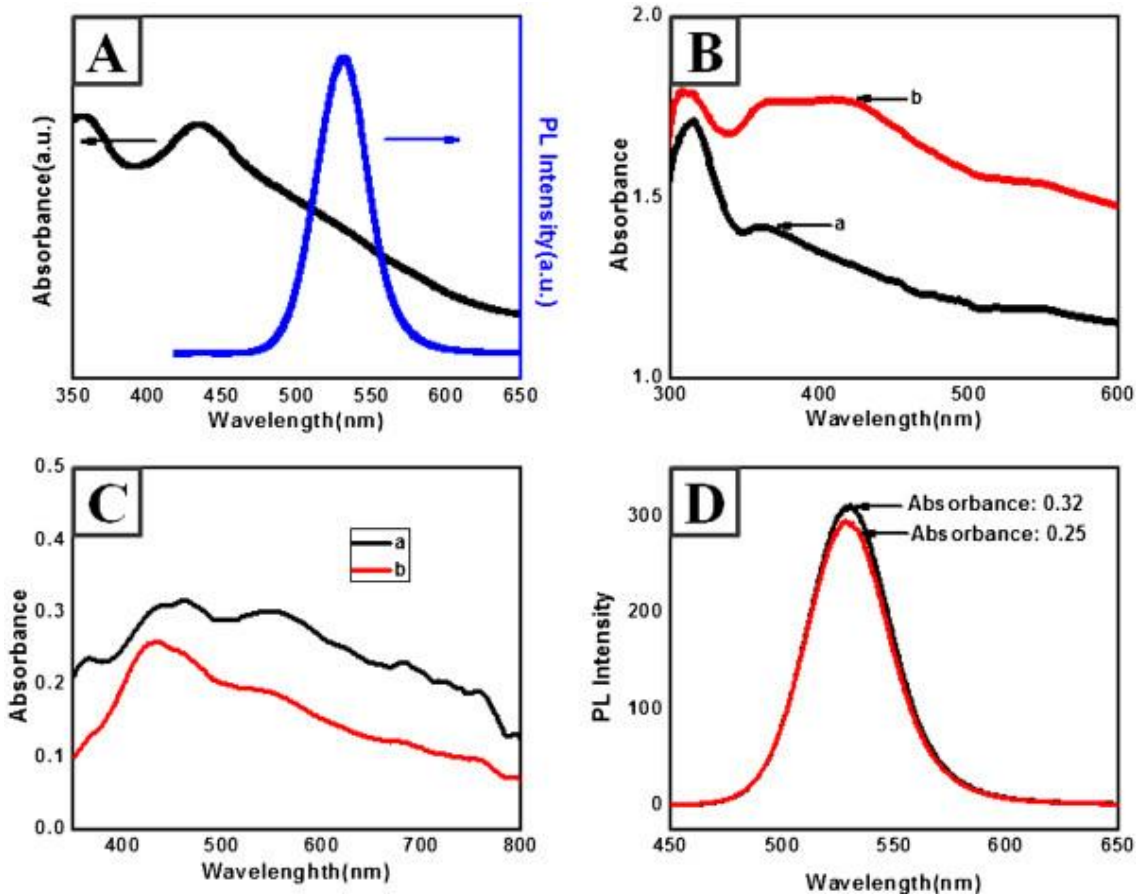


Figure 2.3: UV and PL spectra of CdSe/ZnS QDs (A) and UV-vis spectra of Ag-nNDLS (B). a, smooth Ag nanofilm; b, Ag-nNDL. (C) Absorbance spectra of QDs on each film. (D) Fluorescence spectra of QDs in chloroform at the same absorbance intensity.

PL decay was measured using a 380-nm excitation source at room temperature. Figure 2.4B shows the PL lifetime profiles of the QDs on the two different Ag surfaces. Clearly, the PL decay on the rough surface was faster than that on the smooth surface. The decay rate of QDs was 9.303 ns, and the decay rates of the CdSe/ZnS nanocrystals on the smooth and rough surfaces were about 2.156, 1.445 ns, respectively, which are much shorter than that of QD. Even the rough surface showed shorter decay rate than the smooth Ag surfaces. The standard deviation of decay was <5% after measurement of different samples ten times. It is probable that the shorter PL lifetimes on the rough surfaces are governed by the energy transfer rate that is faster than that in the case of the smooth surfaces.

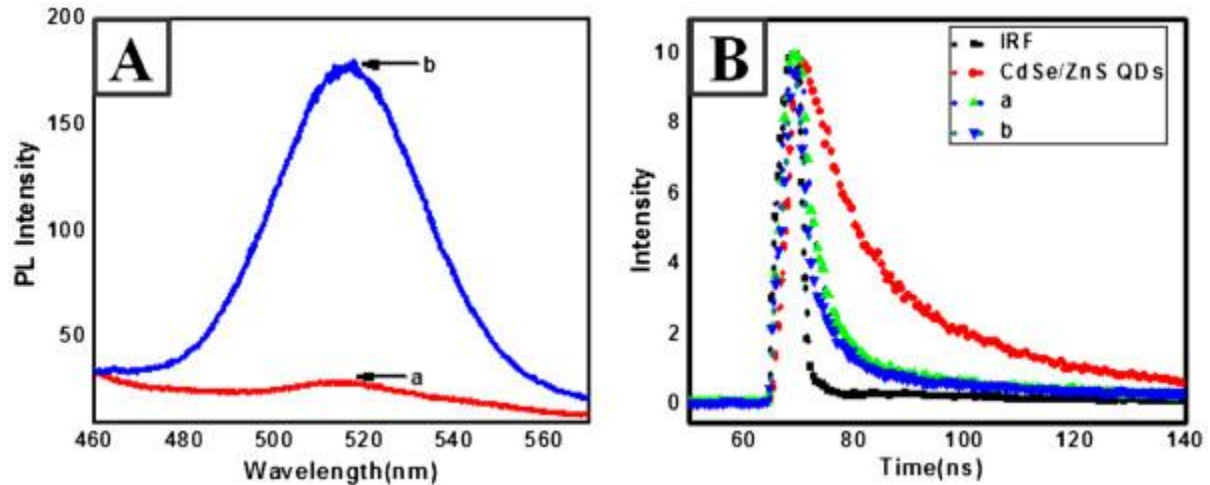


Figure 2.4: PL spectra for CdSe/ZnS nanocrystals on silver surfaces (A). a, smooth surface; b, rough surface. (B) Time profile of PL signal for CdSe/ZnS nanocrystals on Ag surfaces.

Interactions between excitons and plasmons occur when metal and semiconductor nanostructures are in close proximity. The noble metallic surface usually displays a plasmon resonance arising from the collective oscillation of migrated electrons. The radiating energy from the QDs is dramatically altered through coupling with the metal plasmon resonance, which causes a change in the emission properties. However, one often discerns two opposite cases of weak and strong coupling. In the weak coupling regime, wave functions and electromagnetic modes of excitons and plasmons are relatively unperturbed, and exciton-plasmon interactions are often described by the coupling of the exciton dipole with the electromagnetic field of the SP. This model has been used to explain the original experiments of an emission dipole in the proximity of a plane metal surface where plasmonic scattering is insufficient and energy dissipates thermally, resulting in minimal fluorescence enhancement. Meanwhile, the strong coupling regime is considered when resonant exciton-plasmon interactions modify exciton wave functions and SP modes and lead to changes of exciton and SP resonance energies that are larger than their natural line widths. Typically, an evanescent field created by total internal reflection at the interface is used to realize supercritical light propagation (forbidden light) in random media. According to near field optics, both metallic surfaces and nanocrystals act as tiny particles. In this regime, the excitation

energy is shared and oscillates between the plasmonic and excitonic systems (Rabi oscillations), and typical anticrossing and splitting of energy levels at the resonance frequency are observed. These energy resonances adsorbed by the QDs result in the plasmon interaction, which could amend the energy gap between the exciton hole and the trapped hole, and thus eliminate the hole-trapping process, omit unwanted nonradiative energy transfer, and lead to enhanced fluorescence emission. The strong coupling regime is observed in heterostructures due to the efficient radiative scattering without any loss of energy, which would lead to interactions between quantum-confined electronic states in semiconductor nanostructures and dielectric-confined electromagnetic modes in the metal counterparts. Such exciton-plasmon interactions allow the design of absorption and emission properties, control of nanoscale energy transfer processes, and creation of new excitations in the strong coupling regime [79,80]. The fluorescence lifetime is also sensitive to the local environment of the QDs. The spontaneous emission decay rates of the optically excited QDs are accelerated by the locally enhanced electromagnetic field in the vicinity of the metallic structure. The possibility of energy transfer between the excitonic and the plasmonic systems depends on the local environment. The surface plasmon coupling technique has the potential to enhance the spontaneous emission rate. For a smooth surface, energy transfer can be considered unidirectional due to the weak exciton-plasmon coupling. The energy is transferred to the metal or semiconductor subsystem that either spatially removes the energy from the interaction zone or rapidly relaxes the energy to lower energy levels, thereby omitting resonant back transfer. In the strong coupling regime, i.e., the rough surface, the energy is stored in both (metallic surface and QDs) and oscillates back and forth between excitons and surface plasmons (Rabi oscillations). The decoherence time of surface plasmons in this case is on the femtosecond time scale and is often shorter than the time required for Rabi oscillations. The scattering of light due to surface roughness is one of the effects that can cause substantial losses and can significantly reduce the SP decoherence time, which is considered to increase radiative decay rates and shorten the fluorescence lifetime.

2.4. Conclusions

In this paper, we present a SP-enhanced QD emission due to scattering on rough Ag nanoneedle films. Our results strongly suggest that the locally enhanced electromagnetic field due to the scattering of SP energy on a rough surface results in a more effective QD excitation, as compared to the case of QDs on smooth surfaces. The strong metal-QD interaction due to the heterogeneous surface topography of the silver nanostructure also dramatically shortens the lifetime of the non-emissive state. The methodology and observations reported here could be relevant for the design and construction of high-efficiency light-emitting diodes, platform fabrication of biological and environmental monitoring, and high-contrast imaging.

CHAPTER III

FLUORESCENT HYBRID NANOSTRUCTURE- BASED ASSAY PLATFORM FOR VIRUS DETECTION

3.1. Introduction

Epidemic diseases via transmission of the virus are becoming a threatening fear for public health system; e.g., the pandemic influenza A (H1N1) 2009 virus was firstly identified in Mexico in 2009 and caused rapid outbreaks, resulting in ca. 18,000 casualties around the world [81]. It continues to expand globally and causes significant rates of morbidity and mortality, particularly in the elderly and children. A rapid diagnosis of influenza viruses is vital for prevention and timely control of influenza epidemics. Currently forefront tests, i.e., immunosensors and genosensors for monitoring influenza viruses at initial stage usually require professional skill, equipment, multiple processes, and low sensitivity, resulting in retardation to clinical decision [82-87]. Numerous technologies for higher sensitivity are emerging for virus detection. In particular, it has been attractive to utilize photoluminescence (PL) enhancement based on the near-field plasmonic effect at metallic nanostructures [3,88,89]. The interaction between metal and semiconductor nanostructure offers attractive opportunities for tuning the optical properties of such composites based on exciton-plasmon coupling. Such composite structures feature complementary optical properties; e.g., semiconductor nanostructures give rise to high emission yields and light-harvesting capabilities, whereas the metallic surface is particularly effective for local probing, confined excitation, non-linear optics and intense PL enhancement [90,91]. Surface roughness has long been considered as one of the critical parameters for optimizing metal enhanced fluorescence and has enabled precise control of localized surface plasmon resonance (LSPR) as well as surface plasmon polariton (SPP). In rough metallic surface, the scattering of SPP mode can produce photons that can decrease diffraction limit and resolve the sub-wavelength structure, thereby unlocking the prospect of utilizing metal-semiconductor nanocomposite films for enhancing PL emission [15,92,93].

Nanoporous gold film has unique physical properties such as excellent stability, biocompatibility, as well as high specific surface area to form self-assembled monolayers from thiols, sulfides and disulfides [94]. Usually a dealloying technique is utilized to prepare nanoporous structures with controlled pore size and ligaments. By exploiting the dealloying method, PL enhancement in the vicinity of metal nanostructures can be achieved with delicate control of the morphology of the surface on the scale of a few

hundreds nanometers in conjunction with interconnected-porous structures [93,94]. In the present study, the fabrication of metallic surfaces with tunable roughness and controlled structures is reported using the dealloying method. The procedure for fabrication of metal–semiconductor hybrid nanostructures was achieved by means of self-assembly techniques, and the importance of the metallic surface morphology for PL enhancement is illustrated. Furthermore, this physical study expanded to develop a highly sensitive metal–semiconductor hybrid nanostructure for the detection of influenza virus (Fig. 3.1).

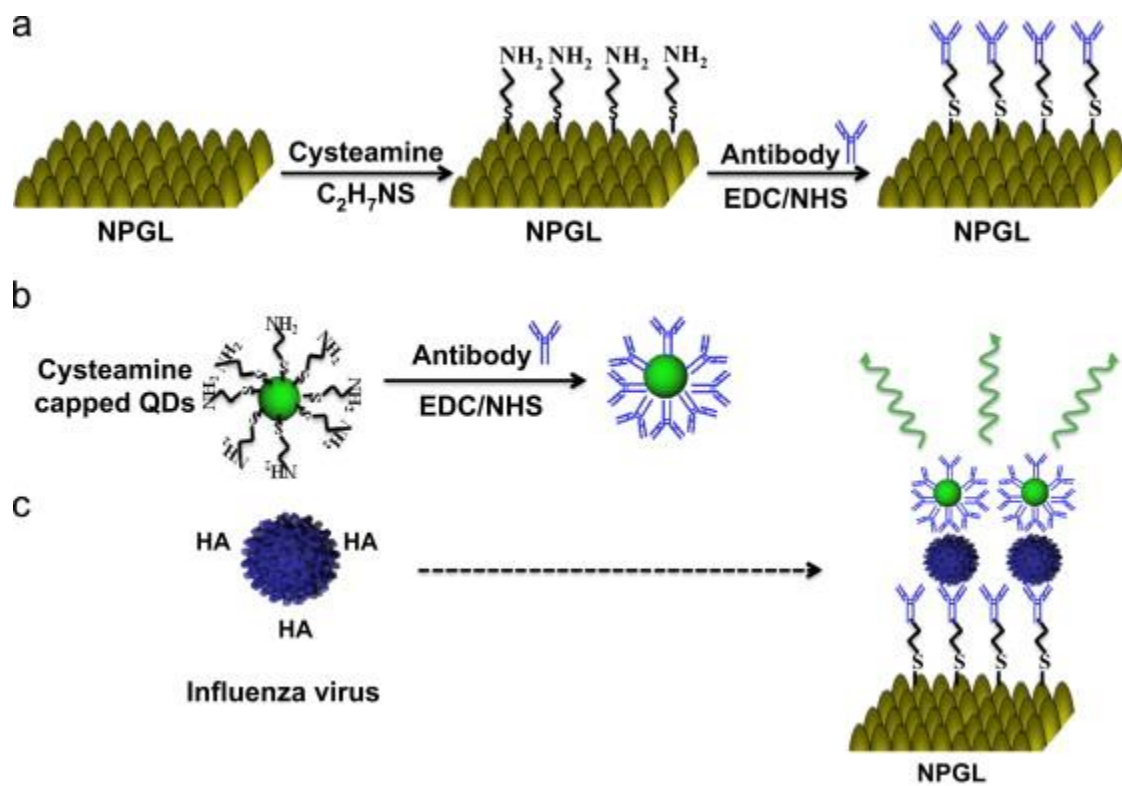


Figure 3.1: Schematic of virus detection using nanoporous gold leaf (NPGL) film. The NPGL (a) and quantum dots (QDs) (b) were firstly conjugated with anti-hemagglutinin (HA) antibodies (anti-HA Ab, Y shape) by the reaction of ethylcarbodiimide (EDC)/N-hydroxysuccinimide (NHS). Then anti-HA Ab-conjugated with NPGL and QDs form complex (c) in presence of HA on the surface of influenza virus, finally enhancing PL intensity.

3.2. Materials and methods

3.2.1. Materials

3-Mercaptopropionic acid (MPA; 99%), poly-diallyldimethylammonium chloride (PDDA; M.W. 400,000–500,000), polyacrylic acid (PAA; M.W.,_450,000), cadmium perchlorate hydrate, thioglycolic acid (TGA), 1-Ethyl-3-(3-dimethylaminopropyl)carbodiimide (EDC) and N-hydroxysuccinimide (NHS) were purchased from Sigma-Aldrich (Milwaukee, USA). Aluminum telluride (Al_2Te_3) was acquired from Cerac Company (Milwaukee, USA) at the highest purity available. The chromogenic substrate, 3,3',5,5'-tetramethylbenzidine (TMB) was obtained from Dojindo (Osaka, Japan). Gold leaf films were purchased from Giusto Manetti Inc. (Campi Bisenzio, Italy). Anti-Influenza A virus HA H1 antibody [B219M] (ab661189, Lot: GR40088-11), anti-Swine Influenza A (H1N1) HA antibody (ab91530, Lot: 942815), and anti-H3 (H3N2) antibody [InA227] (ab82454, Lot: GR84403-3) were purchased from Abcam Inc. (Cambridge, UK). Recombinant influenza A virus HA (H1N1) (New Caledonia/20/1999; Cat: 11683-V08H) and influenza virus A/Beijing/262/95 (H1N1) (Cat: 81N73-2) were purchased from Sino Biological Inc. (Beijing, China) and HyTest Ltd. (Turku, Finland), respectively. Influenza virus A/Yokohama/110/2009 (H3N2) that was isolated from a clinical sample was kindly provided by Dr. C. Kawakami of the Yokohama City Institute of Health, Japan, and was used for confirming the versatility of the assay system. ECLTM anti-mouse IgG, horseradish peroxidase (HRP) linked whole antibody (from sheep) was purchased from GE Healthcare UK Ltd. (Buckinghamshire, UK). All other chemicals were obtained from Wako Pure Chem. Ind. Ltd. (Osaka, Japan). All experiments were carried out using high purity deionized (DI) water (418 M Ω).

3.2.2. Preparation of NPGL and semiconductor nanoparticles

The dealloying process of NPGL film has previously been described [93]. In this study, a gold/silver leaf was gently placed on a microscope slide. This slide was then slowly immersed into a beaker of concentrated nitric acid in order to float the leaf at the air–acid interface. The glass slide was removed when the leaf floated freely on the surface of the nitric acid solution. Subsequently, it was dealloyed for the desired time

intervals of 5, 10, 30, and 60 min, and labeled as NPGL05, NPGL10, NPGL30 and NPGL60, respectively. The leaf was removed from the acid using a glass slide and transferred into a beaker containing deionized water, where the leaf was rinsed by floating for 30 min. The dealloyed leaf was withdrawn on a glass substrate that had previously been modified with 3-mercaptopropyl trimethoxysilane in n-hexane. TGA-capped cadmium telluride (CdTe) QDs were also synthesized by a technique previously reported in detail [95] and stored at 4 °C prior to use.

3.2.3. Immobilization of CdTe QDs on the NPGL substrate

To evaluate optical properties of NPGL surface, the QDs were immobilized on the NPGL substrate by means of ultrasonic-assisted layer-by-layer (LbL) assembly [96]. The polymer spacer layer of ca. 20 nm between nanocrystals and metal surface avoids unwanted quenching effects but assists PL enhancement.

3.2.4. Immobilization of CdTe QDs on the NPGL substrate

An electrostatic charge was transferred to the NPGL substrate by immersion of the sample in 10 mM methanolic 3-mercaptopropionic acid for 30 min, followed by numerous washing steps with alternating methanol and DI water. The sample was then dried under a flow of ultrapure nitrogen gas. All substrates acquired a negative charge at this stage. The negatively charged substrates were used for polyelectrolyte deposition beginning with PDDA. Polymer layers were deposited on the functionalized NPGL substrates by means of ultrasonic-assisted layer-by-layer (LbL) assembly, a method previously used to deposit nanoparticles into nanoscale porous structures to effectively generate uniform distribution and strong penetration into the solid films. Following this procedure, 1% PAA and 1% PDDA were prepared in aqueous media. Beakers containing the polymer solutions and rinsing deionized water were placed in an ultrasonic bath (Bransonic 8510E-DTH, USA) for efficient penetration of the polymers into the porous substrate. The substrates were immersed in PAA or PDDA solution for 10 min, followed by washing in DI water for 10 min in order to assemble two layers of PDDA and PAA, depicted as [PDDA/PAA]₂PDDA. The final stage for the NPGL was immersion in PDDA

to confer strong positive electrostatic charges. The LbL-assembled sample was then washed with DI water and dried under ultrapure N₂ gas. This sample was immersed in CdTe QD solution, stabilized with TGA for 10 min, at which time the final concentration of the QD solutions was adjusted to the nanomolar level by dilution with DI water to pH 9.5 using 1 M NaOH (note: the original synthesized solution was of μM concentration). This dilution prevented any unwanted probe aggregation owing to strong electrostatic interactions of the substrate by decreasing the deposition rate during the LbL assembly process. The polymer spacer layer (~20 nm) between nanocrystals and metal surface avoids unwanted quenching effects due to radioactive energy transfer from nanocrystals to metal surface and assists in PL enhancement.

3.2.5. Topographic observation and spectroscopic studies of NPGL films

Topographic images of the NPGL surfaces were obtained using atomic force microscopy (AFM, diInnova, Veeco, USA) and scanning electron microscopy (SEM, S4700, Hitachi High-Technol. Co., Minato-ku, Japan).

3.2.6. Characterization of antibody specificity

The specificity of the antibody for H1N1 was evaluated using an enzyme-linked immunosorbent assay (ELISA). Briefly, viral stocks were diluted with phosphate buffered saline (PBS, pH 7.5) to a concentration of 10 $\mu\text{g/ml}$ to perform the ELISA. Virus solution (100 μl) was then added to each well of a polystyrene, nonsterile, 96 well, flat bottom microtiter plate (Becton Dickinson Labware, NJ, USA) and incubated overnight at 4°C to allow adsorption of the virus to the plates. The plates were then rinsed with PBS (pH 7.5) buffer and blocked with 100 μl of 2% skim milk for 2 h at room temperature. One ng/ml of mAb HA Ab66189 and BSA (100 $\mu\text{l/well}$, 1 ng/ml) were added to the pre-adsorbed wells and the plates incubated for 1 h at room temperature. The secondary antibody, HRP-labeled goat anti-mouse IgG (GE Healthcare UK Limited, UK) was then added to each of the wells. The chromogenic substrate, TMB was added to each well and the absorbance of the enzymatic product read at 450 nm using a plate reader (Model 680, Bio-Rad, Hercules, CA, USA) to quantify the interaction of mAb with whole influenza virus.

3.2.7. Conjugation of HA Ab66189 antibody with NPGL and its binding check using ELISA

An initial cysteamine monolayer was formed on the NPGL by placing it into a 10 mM aqueous solution of cysteamine for about 20–30 min. Positively charged amino group was acquired on the surface of NPGL at this stage. After rinsed several times with DI water, 100 μ l of EDC (4 mM) and 10mM of NHS were added in all wells and incubated for 30 min, following by addition of 1 μ l of HA Ab66189 antibody (final concentration of 5 ng/ml) in each well and kept at 4°C for 24 h. The plate was washed 3 times with PBS buffer solution to remove nonspecific or unbound components. Antibody will bind with NPGL either through amide bond or simply electrostatic interaction. To check whether antibody binds with NPGL or not, samples were blocked with 100 μ l of 2% BSA for 2 h at room temperature. One ng/ml antimouse IgG-horseradish peroxidase (HRP) (Santa Cruz Biotechnology, CA) was added to each sample. After incubation at room temperature for 1 h, samples were washed 3 times with PBS buffer solution. Horseradish peroxidase (HRP) was developed with 100 μ l TMBZ substrate solution (10 μ g/ml, TMB, 10% H₂O₂ in 100 mM NaOAc, pH 6.0) for 5–30 min at 25°C. A blue color solution developed at this stage. The reaction was stopped by adding 100 μ l 10% H₂SO₄. The solution then became yellow in color and the absorbance read at 450 nm with a reference at 655 nm using a micro plate reader (Model 680, Bio-Rad, Hercules, CA, USA).

3.2.8. Binding capacity of HA Ab66189 antibody with cysteamine capped QDs using ELISA

Cysteamine capped CdTe QDs were synthesized with modification as previously described [95]. Fifty microliter of HA Ab66189 antibody modified QDs were prepared in a 1.5 ml tube using 4 mM of EDC, NHS (10 mM). Anti-mouse IgG-HRP (Santa Cruz Biotechnol., CA) was then added for a final concentration of 1ng/ml. Following 1h incubation at room temperature, samples were washed by centrifuge at 9170 g for 10 min, three times. HRP was developed with 50 μ l TMBZ substrate solution (10 μ g/ml TMB) and 10% H₂O₂ in 100 mM NaOAc, pH 6.0) for 5–30 min at 25°C. The reaction was stopped by adding 25 μ l of 10% H₂SO₄ and the absorbance read at 450 nm with a

reference at 655 nm using a micro plate reader (Model 680, Bio-Rad, Hercules, CA, USA).

3.2.9. Detection platform of HA, Influenza viruses A/Beijing/262/95 (H1N1), and A/Yokohama/110/2009 (H3N2) on NPGL

Antibody specificity for HA (H1N1) was confirmed using an enzyme-linked immunosorbent assay (ELISA) before conjugation to NPGL5 film. The anti-HA Ab (ab66189)-conjugated NPGL5 films were rinsed 3 times with phosphate buffered saline (PBS). 100 μ l anti-HA Ab-conjugated QDs (Ab-QDs) containing different concentrations of recombinant influenza HA (H1N1) were added to the microplate wells. An Ab-QDs solution in BSA and without influenza virus HA (H1N1) was added to the same microplate as a negative control. To determine the PL enhancement effect of NPGL05 for HA detection, an identical amount of Ab-QDs solution containing 10 mg/mL HA protein was added to the wells of microplate. The microplate was then incubated for 30 min at room temperature. An infinite F500 microplate fluorescence reader (TECAN, Männedorf, Switzerland) was employed to measure the PL intensity of each well. The samples were excited at 380 nm, and the exciting and the emission slits were 5 and 10 nm, respectively. Based on the PL values at different concentrations of HA, a dose-dependent curve was constructed. This NPGL-based assay platform was applied on detection of two different types of influenza viruses using the same protocol as described above. Influenza virus A/Beijing/262/95 (H1N1) was detected using anti-HA (H1N1) Ab-bioconjugated NPGL and QDs; influenza virus A/Yokohama/110/2009 (H3N2) was detected using anti-HA (H3N2) Ab-bioconjugated NPGL and QDs.

3.2.10. Detection of influenza virus by rapid influenza diagnostic test (RIDT)

To carry out direct and complementary comparison of the detection ability with commercially available influenza diagnostic kit, a commercial RIDT (ImunoAce Flu, TAUNS Lab. Inc., Numazu, Shizuoka, Japan), was purchased to detect Influenza virus A/Yokohama/110/2009 (H3N2) according to manufacturer's protocol. Different virus titers were prepared and then, three drops of virus solution were put on the sample port of the testing kit. Positive and negative influenza diagnostic results were obtained from different

significant bands that appeared on the strip paper after 10 min of incubation at room temperature.

3.3. Results and discussion

3.3.1. Topographic observation of NPGL films

SEM and AFM images showed that the pore sizes of the substrates varied depending on the dealloying times (Fig. 3.2a–d). The size of the pores and ligaments increased with longer dealloying times due to increased removal of the less-noble constituent (silver) of the alloy. AFM was used to evaluate the root mean square roughness (R_{rms}) of the surface of each substrate with different dealloying times. The R_{rms} of the substrate was calculated in the scanning area ($3 \times 3 \mu\text{m}^2$) of the AFM tip. It was found that the shorter is dealloying times the smaller is pore sizes, resulting in increasing surface irregularities and the surface roughness. Four selected NPGL samples of variant surface roughness (R_{rms} in lower panel of Fig. 3.2) were used for further optical evaluation.

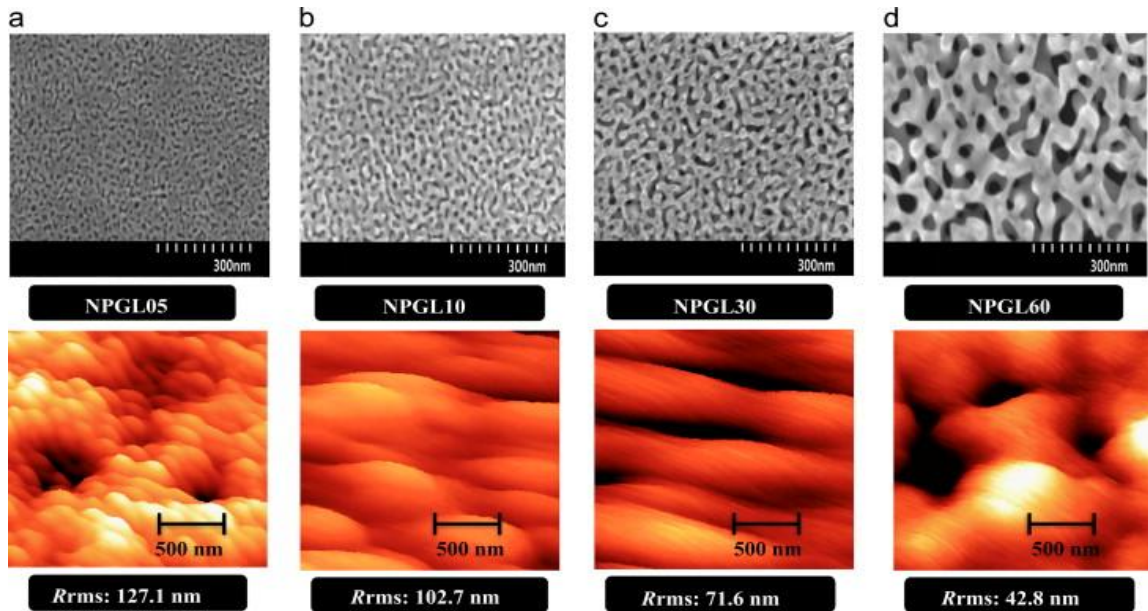


Figure 3.2: SEM and AFM images and the measured R_{rms} of each NPGL sample with various dealloying times (5–60 min), where e.g., NPGL05 depicts 5 min of dealloying time. Dealloyed times are 5 min (a), 10 min (b), 30 min (c) and 60 min (d). Bars in upper and lower panels denote 300 and 500 nm respectively.

3.3.2. Spectroscopic and microscopic studies of the NPGL films

The PL band of the synthesized QD solution was observed at 526 nm with a relative quantum yield of 20% that was determined from the relative ratio versus rhodamine B dispersed in ethylene glycol, where the quantum yield of rhodamine B was 0.95 (Fig. 3.3A). Given that the surface roughness of each produced NPGL films differed, special care was taken in the QD immobilizing process to ensure that the equivalent amount of QDs was deposited on each substrate. Consequently, it is important to produce a monolayer of QDs on the surface of a metallic substrate. We monitored the absorbance of the QDs on the respective substrates to maintain similar intensities by adjusting the deposition time during the LbL process. Then, the PL intensity of the QD solution at the same absorption of the LbL film was measured. It was observed that the difference in the PL intensity of the various samples was less than 10%, indicating that fairly identical amount of QDs were deposited on the samples (Fig. 3.3B). Indeed, PL enhancement of QDs on metal surfaces was observed. Fig. 15a shows that higher the roughness higher is the PL enhancement; e.g., the emission intensity of QDs on NPGL05 (R_{rms} .127.1 nm) and NPGL60 (R_{rms} .42.8 nm) was 9- and 2-fold higher than that on a glass substrate, respectively (Fig. 3.4a). When QDs were deposited on the metal surface without a spacer layer, no PL intensity was observed, rather quenching dominated. This remarkable PL enhancement may be attributed to a strong interaction with surface plasmon of metallic substrate. It has previously been reported that the excitons generated in the QDs can resonate with electron vibrations at the metal surface collectively to induce luminescence enhancement [20,91]. Furthermore, the roughness effect on PL enhancement may be related to the multiple scattering phenomena of the SPP mode in combination with rough surfaces. Such roughness and imperfections in nanostructured random media allow SPP of high momentum to scatter and lose momentum and then couple to radioactive light [21].

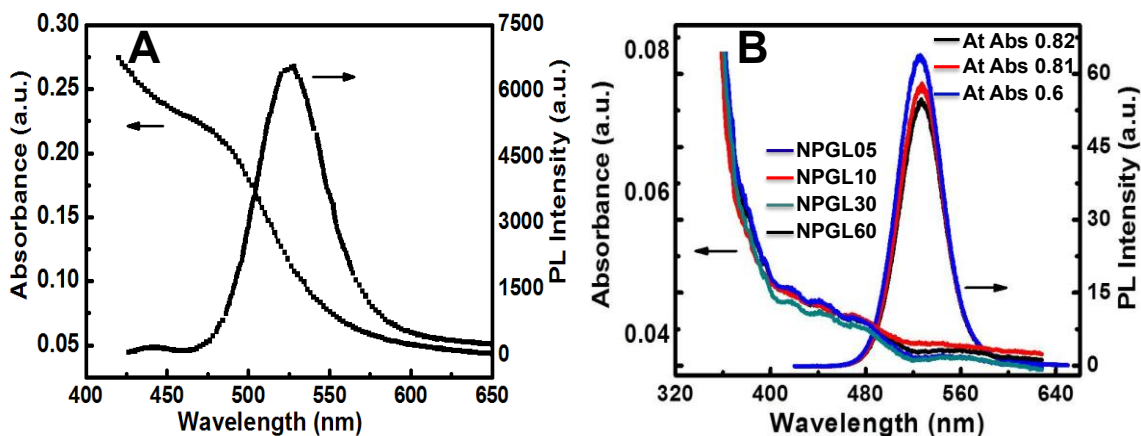


Figure 3.3. (A) UV and PL spectra of CdTe QDs; (B) absorbance spectra of QDs on different films and PL spectra of QDs in aqueous solvent at the same absorbance intensity.

The fluorescence lifetimes (τ) of the respective samples were measured at an excitation wavelength of 380 nm using a light-emitting diode spectrophotometer (PTI Inc., USA). The spectra in Fig. 3.4b presents that the rougher the substrate is the shorter is the lifetime, i.e., the PL lifetime varied from 3.17 ns to 1.2 ns while the Rrms values varied from 42.8 to 127.1 nm (Fig. 3.4c). In contrast, the lifetime of CdTe QDs on glass slides was 7.42 ns. In particular, the short dealloying time generated ultrafine structures that are characterized as small pores and pimples (~10 nm) that play a major role in plasmonic scattering with consequent PL enhancement. Fig. 3.4d demonstrates a fluorescence microscopic image of the QD/polymer-deposited films on metallic nanostripe pattern to demonstrate strong PL enhancement induced by metal enhanced fluorescence. With increasing surface roughness, multiple scattering of lights occurs in nanostructured random media. The high enhancement effect observed in close proximity of metallic nanopatterns is primarily due to the absorption and/or emission bands of the QDs overlap with the scattering wavelength of the rough metallic surface. From these fundamental physical experiments NPGL05 substrate was chosen for further sensing experiments of virus detection.

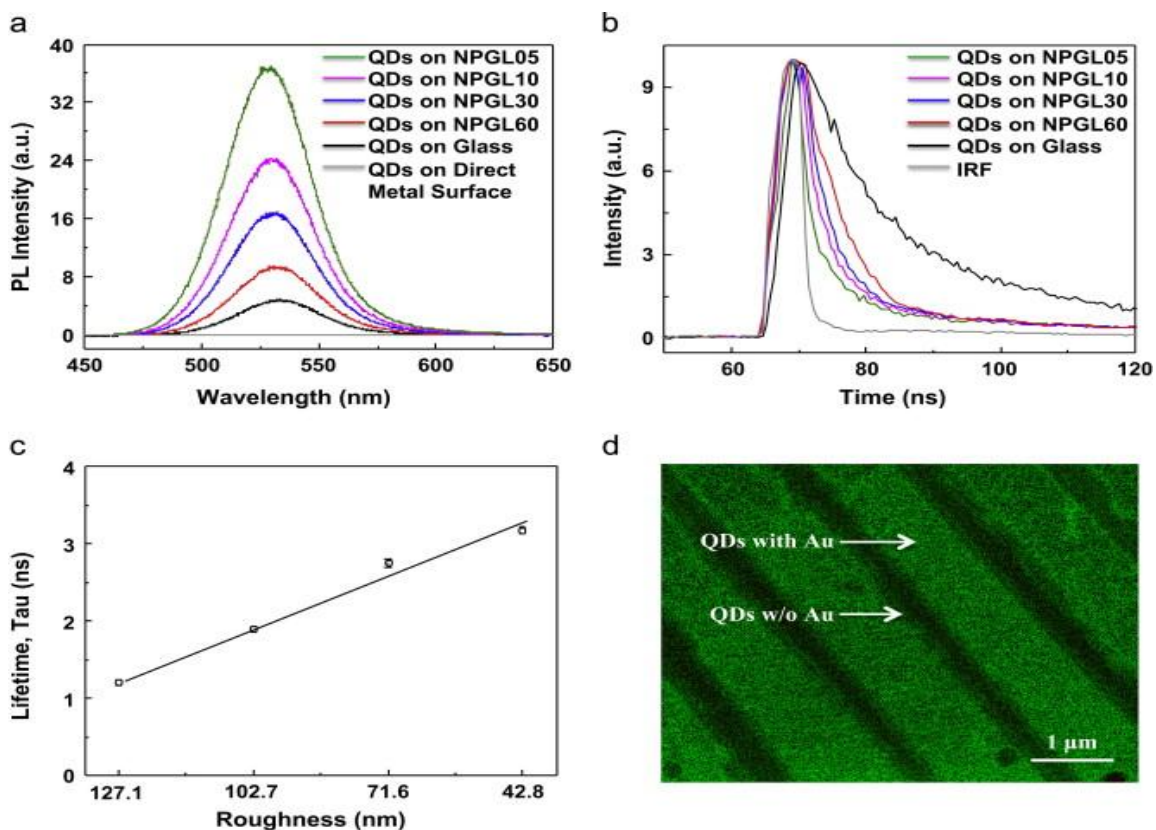


Figure 3.4: (a) Photoluminescence (PL) spectra of QDs on different roughnesses of NPGL and glass substrate (for QD only); (b) time-based fluorescence kinetics profile of PL signal for QDs on different surfaces; (c) lifetimes (τ) variance depending on surface roughness; (d) fluorescence microscopic image of QDs on metallic nanostripe patterns. IRF in (b) stands for instrumental response function. The error bars in (c) indicate standard deviation (SD) in each measurement and the scale bar in (d) denotes 1 μm .

3.3.3. Immunoassay of HA on NPGL05 and QDs

It is known that HA, a surface glycoprotein on the surface of viruses has unique immune-specificity in the initial stage of infection mechanism [97]. The detailed optical observation at every respective step of bioconjugation with nanomaterials and antibodies was carefully monitored by using ELISA and FTIR spectrophotometry. Immuno-specificity of the anti- HA Ab (ab66189) for influenza virus A/Beijing/262/95 (H1N1) was investigated. A different type of Ab (ab91530) and BSA was used for comparison. A higher absorbance was observed with anti-HA Ab (ab66189) compared to the anti-HA Ab (ab91530) or BSA (Fig. 3.5A). From these experimental results, anti-HA Ab

(ab66189) has a strong immunospecificity for influenza virus A/Beijing/262/95 (H1N1) whereas other antibody and BSA show no binding affinity with influenza A virus. The ELISA test indicated that the antibodies are successfully conjugated on the NPGLs without losing its binding affinity (Fig. 3.5B and C). Furthermore, FTIR bands found at 3700–3500 cm^{-1} for amide N–H stretching and 1690–1630 cm^{-1} for amide C=O stretching corresponds the chemical binding between NPGL and anti-HA Ab (ab66189) (Fig. 3.5D). Then the same experiments were carried out to scrutinize any influence of binding affinity when cysteamine capped QDs were conjugated with anti-HA Ab (ab66189) using recombinant influenza H1N1 HA (New Caledonia/20/1999) (Fig. 3.6A), resulting that cysteamine capped QDs were successfully conjugated with the antibody (Fig. 3.6B and C). In fluorescence microscopic image, the aggregated and brighter spot might be virus deposited part on the film (Fig. 3.6D).

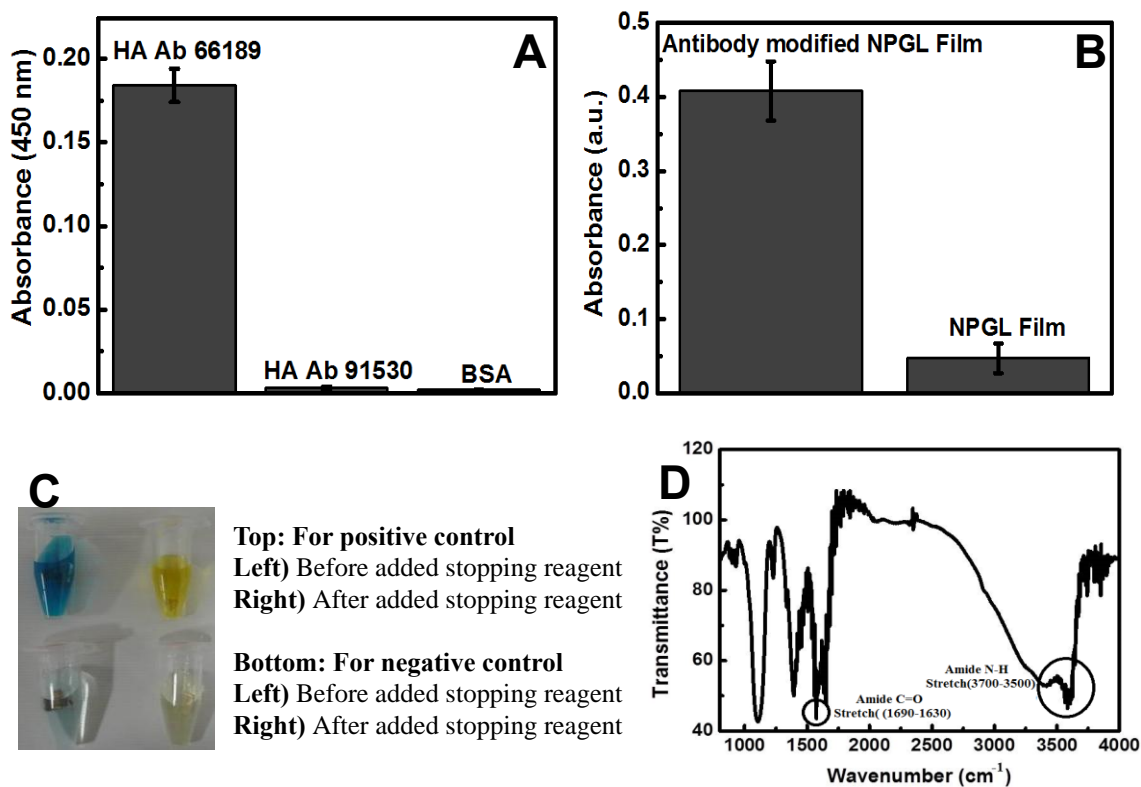


Figure 3.5: (A) ELISA for HA ab66189 antibody binding with influenza H1N1 HA; (B) ELISA for recombinant influenza H1N1 HA binding with HA ab661891 antibody-conjugated NPGL05; (C) Binding check of antibody with NPGL05 with naked eyes; (D) FTIR spectrum of antibody binding with NPGL. The error bars in A and B indicate standard deviation (SD) in each measurement.

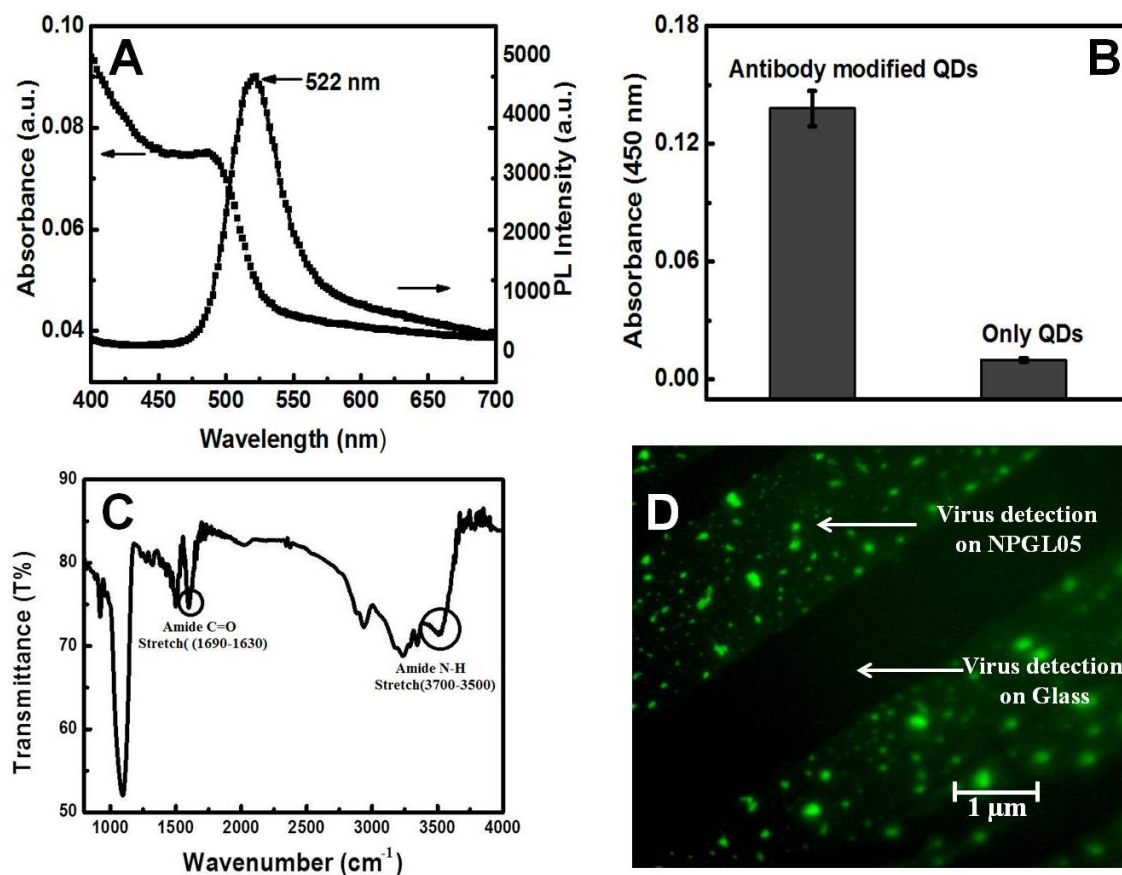


Figure 3.6: (A) PL and absorbance spectra of cysteamine capped QDs; (B) ELISA for HA ab661891 antibody-modified QDs with recombinant influenza H1N1 HA ; (C) FTIR spectrum of antibody binding with QDs ; (D) Fluorescence microscopic image of virus detection. The error bars in B indicate SD in each measurement.

The detection procedure consisted of three steps – (i) binding of antibody on NPGL, (ii) binding of antibody on QDs and (iii) immune-reaction between the antibody and antigen. After confirming the binding affinity of antibody on the surface of NPGL film, the recombinant HA (H1N1) was monitored. Both NPGL film and QDs were bound with anti-HA (H1N1) Ab (ab66189). With HA, these bioconjugated components form a complex, consequently producing high PL intensity from QDs via surface plasmon resonance with the NPGL substrate. In our experiment, 3 times higher PL intensity were monitored in the nanostructure of the antibody-functionalized NPGL than that without the NPGL, where 10 mg/mL of HA was added in each experiment (Fig. 3.7A). In the quantitative analysis using different concentrations of HA, PL intensities were

logarithmically correspondent on HA concentration in the range of 1 ng/ml–10 µg/mL (Fig. 3.7B and the inset). However, there was no significant PL change without any addition of HA or in the addition of BSA.

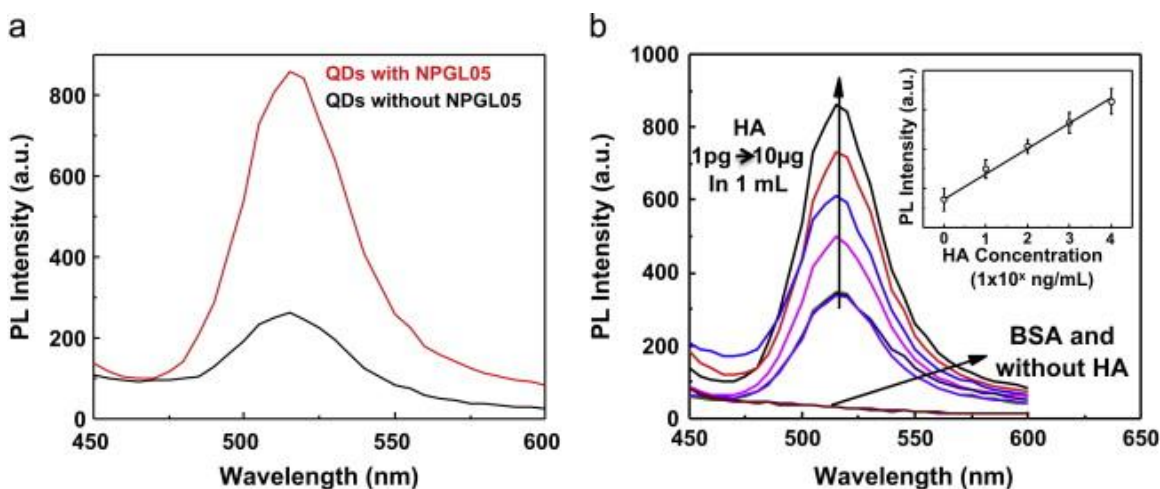


Figure 3.7: (a) PL enhancement of QDs with and without the nanostructure; (b) PL enhancement corresponding on different quantities of recombinant influenza HA (H1N1) on anti-HA Ab-conjugated NPGL05. (Inset) The calibration curve of PL intensity versus HA concentration. The error bars indicate SD in each measurement.

3.3.4. Immunoassay for virus detection

After confirmation of HA monitoring using this novel sensing system with NPGL and QDs, different concentrations of influenza virus A/Beijing/262/95 (H1N1) where the surface of this virus also has specific binding sites of anti-HA (H1N1) Ab were monitored. Similar results were observed as the previous experiment of HA only as shown in Fig. 3.7b. A significant PL enhancement was observed in the presence of viruses and NPGL (Fig. 3.8a). Furthermore, a logarithmical relationship existed between PL intensities and the virus concentration in the range of 1 ng/ml–10 µg/mL (Fig. 3.8b). Using this developed monitoring system, an influenza virus A/Yokohama/110/2009 (H3N2) was monitored. The specificity of HA (H3N2) Ab 82454 for influenza virus A/Yokohama/110/2009 was confirmed (Fig. 3.8c), and binding of HA (H3N2) Ab 82454

with NPGL05 and QDs was also confirmed using ELISA (Fig. 3.9). Then, the sensitivity of influenza virus A/Yokohama/110/2009 (H3N2) detection was observed in the range of 50–10,000 plaque forming units (PFU)/mL (Fig. 3.8d). The detection limit was shown at ca. 50 PFU/mL.

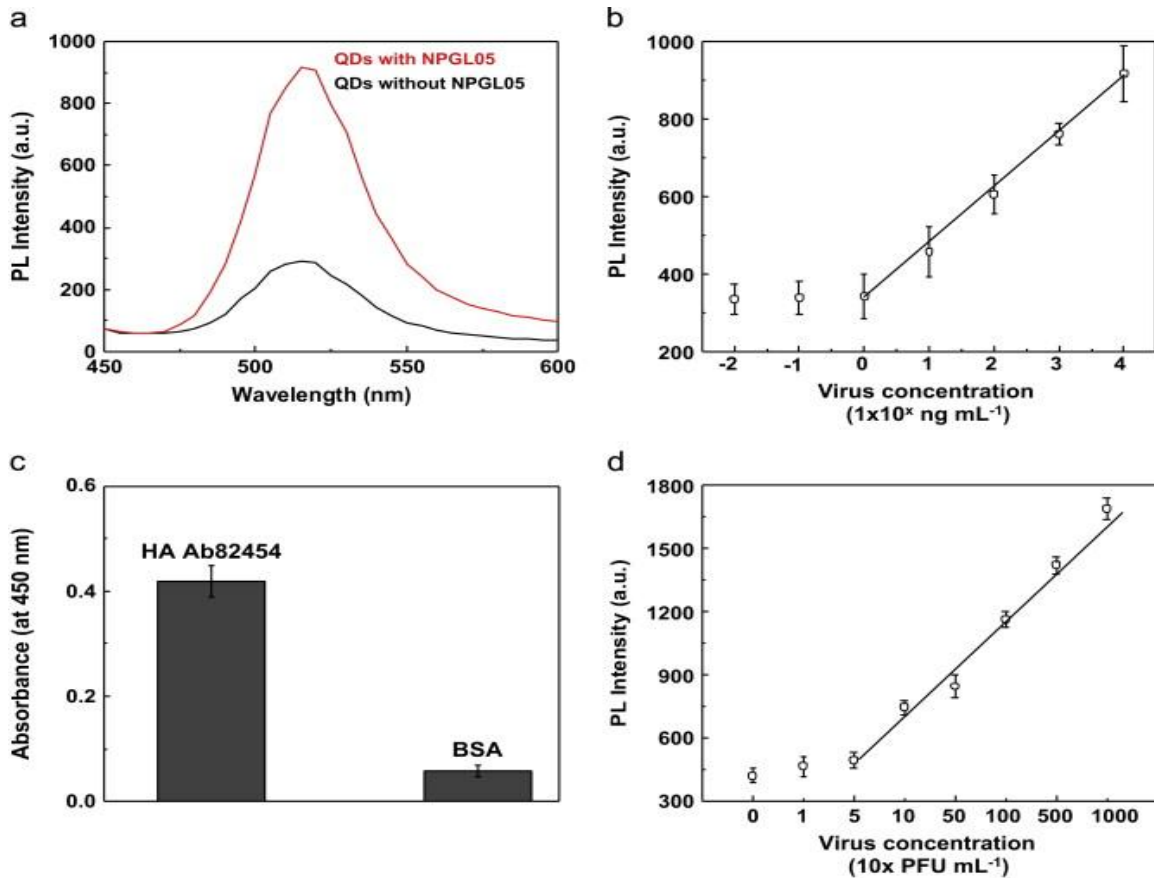


Figure 3.8: (a) PL spectroscopic detection of influenza virus A/Beijing/262/95 (H1N1) using anti-HA (H1N1) Ab (ab66189)-bioconjugated QDs depending on the existence of anti-HA (H1N1) Ab (ab66189)-bioconjugated NPGL05 film; (b) PL intensity versus influenza virus A/Beijing/262/95 (H1N1) concentration; (c) ELISA results for anti-HA (H3N2) Ab 82454 binding with influenza virus A/Yokohama/110/2009 (H3N2); (d) the calibration curve of PL intensity corresponding on the concentration of the influenza virus A/Yokohama/110/2009 (H3N2). The error bars in (B–D) indicate SD ($n=3$).

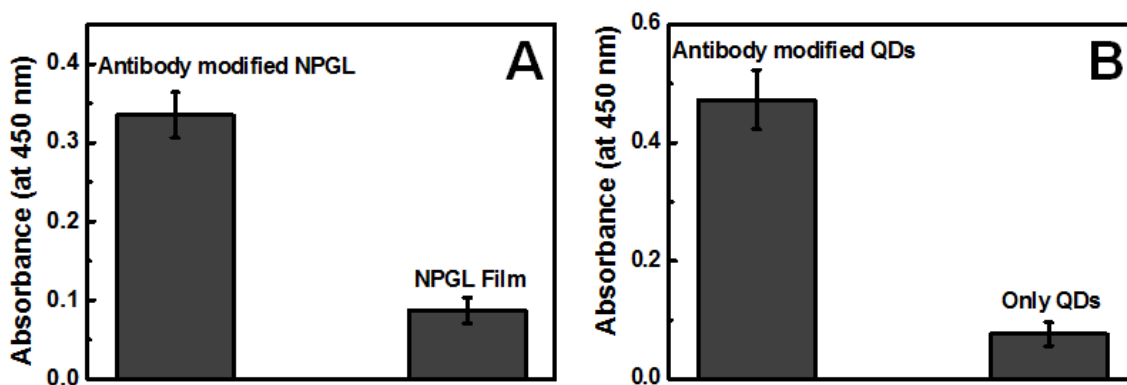


Figure 3.9 (A) ELISA for HA (H3N2) ab82454 antibody-modified NPGL film with recombinant influenza HA (H3N2); (B) ELISA for HA (H3N2) ab82454 antibody-modified QDs with recombinant influenza HA (H3N2). The error bars in A & B indicate SD in each measurement.

3.3.5. Detection of influenza virus using rapid influenza diagnostic test (RIDT)

A commercially available RIDT kit (ImunoAce Flu, TAUNS Lab. Inc., Numazu, Shizuoka, Japan) was used for comparison with our sensing system to diagnose influenza virus infection using the influenza virus A/Yokohama/110/2009 (H3N2). Table 1 shows the results of the RIDT depending on the concentration of virus. In the case of the commercial RIDT, at least 5000 PFU/mL of virus was required for detection, which means the limit of detection (LOD) of the influenza virus detection using our sensing system of NPGL-QDs was 100 times more sensitive than that of the commercial RIDT.

Table 1:
Comparison of influenza virus A/Yokohama/110/2009 (H3N2) detection using RIDT.

Detection method	Virus concentration (PFU/mL)								
	10000	5000	1000	500	100	50	10	1	0
This study	+	+	+	+	+	+	-	-	-
Commercial RIDT	+	+	-	-	-	-	-	-	-

Note: + and - denote positive and negative diagnosis's, respectively.

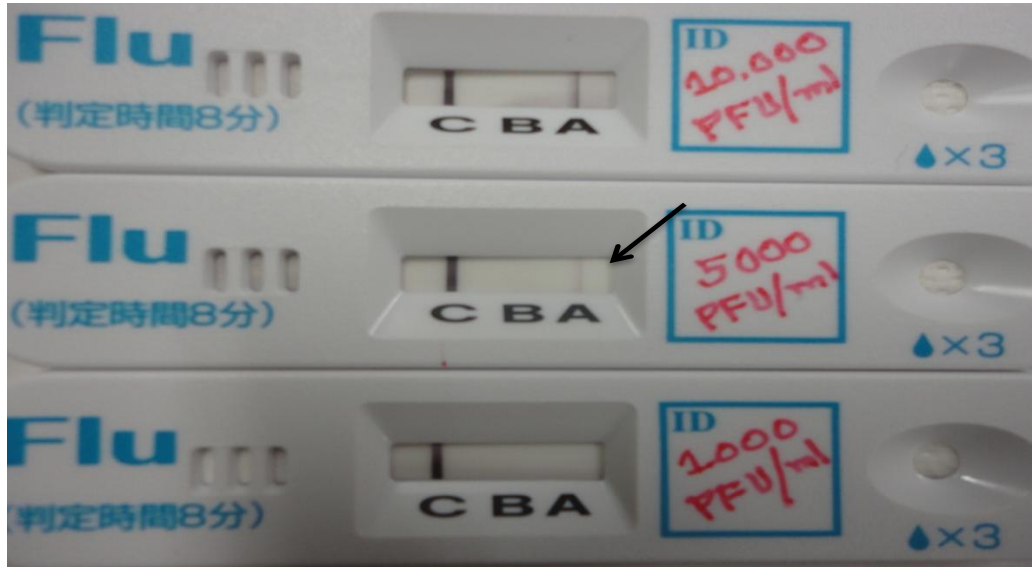


Figure 3.10. Influenza virus A/Yokohama/110/2009 (H3N2) detection using commercial RIDT. Virus concentrations were 10,000, 5,000 and 1,000 PFU/ml, respectively. A, B, and C denote influenza A virus, influenza B virus, and control, respectively.

In this study, a new detection method on metallic surface based on exciton-plasmon interaction was presented. In particular, the research centered on the development of robust rough metallic surfaces that would be used for the generation of high efficient optical device for biosensor applications. Many implications for medical take care require a low detection system. An important goal here was to improve detection limit with high sensitivity. As we can see, our proposed detection method showed at least 100 times higher sensitivity than a representative commercial test kit. It might result from the presence of plasmonic rough metallic surface and adjacent control of distance between QDs to induce PL enhancement. In addition, the assay is performed with fewer amounts of reagents and easier to wash out unbound reagents. However, because of the lack of many medical samples, the huge analysis is not attainable using our technique up to now, which will be included in future work.

3.4. Conclusion

This paper reports a near-field optical evaluation of QDs and plasmonic surface composites with varying roughness. A dramatic enhancement of PL intensity and decay rate of the QDs was achieved on rougher metallic surfaces. The observation of these PL enhancements from nanocomposites was further applied for the development of sensitive influenza virus A (H1N1) detection (up to 1 ng/mL) and influenza A (H3N2) virus isolated from a clinical sample (up to 50 PFU/mL). The proposed method represented an alternative traditional method by requiring a higher sensitivity, much smaller sample volume, less amount reagents. Further research will be focused on the development of rough plasmonic metallic surface using self-assembly techniques as well as clinical evaluation.

CHAPTER IV
FLUORESCENT HYBRID NANOSTRUCTURE FOR
IMAGING COLON CARCINOMA CELLS

4.1. Introduction

The merging of dual natured components of optical and magnetic properties on nanoscale regime can enable new advance in molecular imaging and medical theranosis that are essential for early detection and rapid treatment of diseases [98,99]. Magnetic nanoparticles (MNPs), e.g. Fe_3O_4 NPs, are of immense importance in the emerging area of nanomedicine because of their ability to be manipulated and detected with an external magnetic field. They can be used in numerous applications, both in vitro and in vivo, such as magnetic resonance imaging (MRI) contrast enhancement [100], bioseparation [101], biosensing [102], cancer therapy using magnetic hyperthermia [103], and targeted drug delivery [104]. Although MNPs appear to be the currently preferred cell-labeling materials, the poor signal intensity on MRI limits their clinical utility [105]. MNPs label is a major limitation for long-term tracking, as the magnetic resonance signal is lost over time due to cellular proliferation, especially with rapidly dividing cells. Hence, more efficient cellular-internalizing methods are highly preferable. Regardless of magnetic imaging, optical techniques offer improved high spatial resolution allowing the visualization of cell structures. They are used for the simultaneous visualization of multiple modalities with two or more fluorescent probes with different spectra, but have limited depth of imaging and poor absolute quantitative accuracy due to the absorption of light in tissues. Magnetic imaging has no practical limitation in terms of the depth of imaging; however, spatial resolution is poor and imaging with more than one probe is problematic [106]. Therefore, it is conceivable that one single agent to provide imaging in multiple imaging modalities (optical and magnetic) would be of great value to offer more comprehensive diagnostic information and the dynamics of disease progression. An example of such multifunctional NPs are FMNPs that bear two attractive features, fluorescence and superparamagnetism, allowing their intracellular movements to be controlled using magnetic force and monitored using a fluorescent microscopy, simultaneous delivery of fluorescence and magnetic particles to individual cells offers the opportunity of correlating optical images and MRI [107,108]. These features could lead to effective multifunctional drug-loaded MNPs that would facilitate increased drug

transport rates, mucus penetration, antibiotic efficiency in biofilms and cellular imaging. Semiconductor nanocrystals called quantum dots (QDs) is well known promising candidate as fluorescent materials for its high photostability, high emission quantum yield, narrow emission peak, size dependent wavelength tunability in comparison with organic dyes and fluorescent proteins. These properties of QDs make them more interesting for potential biomedical application such as protein trafficking, DNA detection, cellular imaging and dynamic studies of cell motility. QDs owing to their inorganic nature, are more robust than organic dyes and therefore their reduced photobleaching under light allows for real-time monitoring of biological events over extended periods of time [109,110]. Taking the advantages of QDs and MNPs, we designed, prepared and characterized new dual-marker particles, simultaneously combining both fluorescence nanocrystals, such as QDs and superparamagnetic nanoparticles (Fe_3O_4 NPs) in one entity. Considerable research has been devoted to the combination of magnetic and fluorescent properties in a single nanocomposite [104,105,111]. However, many of those synthetic processes usually involve complexed multi-step reactions [112-114]. Alternatively, a rapid one pot self-assembly synthesis using controlled electrostatic force may improve photostability and colloidal stability. The cytotoxicity of prepared NPs was investigated in Vero cells using the trypan blue in vitro assay. The result indicates the cytotoxicity of FMNPs were reduced with dilution and allowed its potential use in biomedical application. The prepared FMNPs were further applied to cancer cell imaging using monoclonal antibodies against specific markers on cancer as a tool for therapy. Humanized monoclonal antibody CC49 (hCC49) [114] is a clinically validated antibody to target tumor-associated glycoprotein-72 (TAG-72) a well-known marker in colon carcinoma [115]. In this work, fragment antigen binding (Fab) region of hCC49 was conjugated with FMNPs, which was used for specific cancer cell imaging. Fluorescence microscopy showed significant preferential binding of the NPs conjugates by cells. Such a nanoprobe could potentially be used to image resections of cancer cells in real time and to correlate preoperative diagnostic images with intraoperative pathology at cellular-level resolution.

4.2. Materials & Methods

4.2.1 Materials

Cadmium perchlorate hydrate, thioglycolic acid solution (TGA) and hexadecyltrimethyl ammonium bromide (CTAB) were purchased from Sigma-Aldrich (St. Louis, Missouri, USA). Aluminum telluride (Al_2Te_3) with the highest purity was acquired from Cerac Inc. (Albuquerque, NM, USA). Ferric chloride, ferrous sulfate, trisodium citrate dihydrate and ammonium solution were purchased from Wako Pure Chem. Inc. (Osaka, Japan). LS174T human colon adenocarcinoma cell line (ATCC No. 50845) and Vero cell (No. CCL-81) strains were purchased from ATCC (Rockville, MD, USA).

4.2.2. Synthesis of CdTe QDs

CdTe-QDs have been synthesized as previously reported [95]. Shortly, 0.985 g (2.35 mmol) of $\text{Cd}(\text{ClO}_4)_2 \cdot 6\text{H}_2\text{O}$ was dissolved in 125 ml of water, and 5.7 mmol of the TGA added under stirring, followed by adjusting pH to appropriate values (11.4–11.6) by dropwise addition of 1 M NaOH. The solution was placed in a three-necked flask and deaerated by nitrogen gas-bubbling for 30 min. Under stirring, H_2Te gas (generated by the reaction of 0.2 g (0.46 mmol) of Al_2Te_3 lumps with 15–20 ml of 0.5 M H_2SO_4 under nitrogen atmosphere) was passed through the solution together with a slow nitrogen flow for 20 min. CdTe precursors formed were converted to CdTe nanocrystals by refluxing the reaction mixture at 100°C under open-air conditions with condenser attached for 20 min. The UV and PL spectra of CdTe QDs were recorded using a Tecan infinite M 200 spectrophotometer. The samples were excited at 380 nm, and the exciting and the emission slits were 5 and 10 nm, respectively.

4.2.3. Synthesis of Fe_3O_4 NPs

The preparation of citrate-capped Fe_3O_4 NPs was synthesized using the previously described method with minor modification [116]. The reaction mixture contained 1.622 g

of $\text{FeCl}_3 \cdot 6\text{H}_2\text{O}$ and 0.994 g of $\text{FeCl}_2 \cdot 4\text{H}_2\text{O}$, were mixed with 40 ml of distilled water. Five ml of concentrated ammonia aqueous (28%) was added in this solution and heated at 90°C . Then, 4.4 g sodium citrate was added and continued the reaction for 30 min. The MNPs thus obtained were washed with anhydrous ethanol and redispersed in deionized water for further use. Particle size and electric charge the prepared Fe_3O_4 NPs were measured by dynamic light scattering (ZetaSizer Nano-ZS, Malvern, UK).

4.2.4. Preparation of FMNPs

New synthesis method for fluorescent-magnetic nanocomposites structure were prepared based on simple and efficient LbL self-assembly method [117]. Briefly, 100 ml Fe_3O_4 NPs were dispersed in 5 ml of CTAB (10 mg/ml) solution under vigorous stirring. Next, 200 ml of ammonia solution was added and the mixture was stirred at room temperature for 30 min. Cationic surfactant CTAB capped Fe_3O_4 NPs by electrostatic force at this stage. Then, 200 ml of CdTe QDs was added and mixtures were stirred at room temperature for 2 h for binding of QDs with CTAB. The resulting FMNPs were collected by external magnetic field, washed three times with MilliQ water and redispersed in MilliQ water for further use. The PL spectra of FMNPs were recorded using a Tecan infinite M 200 spectrophotometer. The samples were excited at 380 nm, and the exciting slit and the emission slit were 5 and 10 nm, respectively.

4.2.5. TIRF microscope and TEM Imaging of FMNPs

TIRF microscope (Leica AM TIRF MC, Germany) was used to observe fluorescence image of FMNPs. Two hundred microliter FMNPs solutions were loaded in glass bottom dishes and samples were excited using 400 nm wavelength. The TEM image of FMNPs was recorded using JEM 2000FX II-TEM (JOEL Ltd., Akishima, Japan). The samples were spotted onto carbon grids (Okenshoji, Tokyo, Japan), dried at room temperature and observed at 50,000 \times magnification operating at 160 kV.

4.2.6. Superconducting quantum interference device (SQUID) measurement

SQUID magnetometry was used to measure the saturation magnetizations of

naked MNPs and FMNPs at 300 K. Aliquots (200 μ l) of the MilliQ suspension of MNPs and FMNPs were placed in micro centrifuge tube and allowed to vacuum evaporation (Centrifugal evaporator CVE-2000, EYELA, Japan). Magnetic measurements were made on a Quantum Design MPMS-7 SQUID (San Diego, CA, USA) magnetometer.

4.2.7. Cell lines and cell cultures

HEK293 was obtained from Riken Bio Resource Center (RCB1637). LS174T cells were cultured in 60 mm culture plates (TPP, Trasadingen, Switzerland) with minimal essential media-eagle (Sigma-Aldrich, Tokyo, Japan) containing 10%(v/v) fetal bovine serum (Invitrogen, San Diego, CA, USA), supplemented with 1%(v/v) antibiotic solution containing penicillin, streptomycin, fungizone (Sigma-Aldrich, Tokyo, Japan) and incubated at 37°C in 5% CO₂ incubator (MCO-175 Sanyo, Osaka, Japan). HEK293 cells were cultured in 60 mm culture plates with MEM/EBSS (HyClone Laboratories Inc., Utah, USA) containing 2 mM L-glutamine, 1% non-essential amino acid (Invitrogen, Carlsbad, CA, USA), 10% fetal bovine serum, supplemented with 1% (v/v) antibiotic solution containing penicillin, streptomycin, fungizone and incubated at 37°C in 5% CO₂ incubator. Both the cell lines were grown till confluence and splitting was done in 1:5 ratio once every week by trypsinisation using TrypLE Express (Life Technologies Japan LTD., Minato-Ku, Tokyo, Japan) for 15 min at 37°C in 5% CO₂ incubator.

4.2.8. Trypan blue test

The cytotoxicity of the FMNPs were determined using the trypan blue exclusion test, which determines the number of viable cells present in a cell suspension. In 96-well plates, 100 μ l suspension of Vero cells (5×10^4 cells/ml) in 5%(v/v) horse serum containing minimum essential medium was added per well and incubated in a 5% CO₂ humidified incubator at 37°C for 24 h. Then different diluted solutions of FMNPs were added to each well and further incubate at 37°C for 24 h. After medium was removed, 0.25% trypsin was added in all wells. The plate was centrifuged (Centrifuge 5430, Eppendorf AG, Germany), removed supernatant and redispersed in 5% (v/v) horse serum minimal essential medium. The 96- well plates were further incubated for 15 min. Fifteen

microliter of trypan blue was added to each cell well. The resulting mixture was gently shaken for 10 min at room temperature. Cell numbers were counted using haemocytometer (Line Seiki, Tokyo, Japan) under microscope (Model CHT, Olympus optical Co. Ltd., Tokyo, Japan) and the percentage of viability was calculated.

4.2.9. Preparation of hCC49 antibody Fab regions

The gene of hCC49 antibody [114] was amplified from plasmid pDong1 (hCC49), which is a gift from Professor Hiroshi Ueda of Chemical Resources Laboratory of Tokyo Institute of Technology by PCR using primers bx-FLAG-hCC49VHCH-F (5'-CACCATGAAGATACTCCTTGCTATTGCATTAATGTTGTCAACAGTAATGTGGG TGTC AACATGGAGCCACCCGCAGTTCGAAAAGATGAAATACCTATTG-3') and hCC49VHCH-R (5'-CTATGCGGCCCCATTCAG-3') for hCC49VHCH1, primers bx-FLAG-hCC49VLCL-F (5'-CACCATGAAGATACTCCTTGCTATTGCATTAATGTTGTCAACAGTAATGTGGGTGTCAACAGACTACAAGGATGACGATGACAAGGATA TTGTGATGACC-3') and hCC49VLCL-R (5'-TCACTCTCCCCTGTTGAA-3') for hCC49VLCL. The amplified genes were inserted into pENTR/D-TOPO (Invitrogen), respectively, to make pENTR/D-hCC49VHCH1 and pENTR/ D-hCC49VLCL by the topoisomerase reaction. Using the above plasmids, the gene was inserted into pDEST8 using Gateway technology (Invitrogen) to construct pDESThCC49VHCH1 and pDEST-hCC49VLCL, which were then used to transform *E. coli* BmDH10Bac to obtain the recombinant *Bombyx mori* nucleopolyhedrin (BmNPV) bacmids, rBmNPV-hCC49VHCH1 and rBmNPV-hCC49VLCL. The recombinant bacmids (10 µg each) were mixed with onetenth volume of DMRIE-C (Invitrogen) and incubated at room temperature for over 45 min. Fifty microliters of this mixture was injected into a silkworm larva on the first day of the fifth instar larvae (Ehime Sansyu Co. Ltd., Ehime, Japan). Injected silkworm larvae were reared for 5–7 days, and the hemolymph collected was centrifuged to remove hemocytes at $2400 \times g$ for 10 min at 4°C. The supernatant was used as a hemolymph sample for purification. Fab antibodies were purified with an ANTI-FLAG M2 Affinity Gel (Sigma) according to the instructions provided by the manufacturer.

4.2.10. Conjugation of hCC49 antibody Fab region with FMNPs and its binding activity

To apply FMNPs on bioimaging, the NPs were conjugated with hCC49 antibodies Fab region to assess their potential as fluorescent probes for LS174T cancer cells. Fab region of hCC49 antibodies has binding affinity with sialylated sugar chain in TAG-72 region of LS174T cancer cells. Electrostatic interaction between positively charged FMNPs (+18.3 mV, measured by ZetaSizer, Nano-ZS, Malvern, UK) and negatively charged of hCC49 antibodies (-3.53 mV, Tris glycine at pH 8.5, measured by ZetaSizer, Nano-ZS, Malvern, UK) was used to bind each other. NPs were dissolved in hCC49 antibodies (final concentration of 20 µg/ml) and kept at 10°C for 2 h with continuous stirring. To check whether antibodies were bound with FMNPs or not, at first FMNPs were blocked with 2% bovine serum albumin (BSA). After incubation at room temperature for 2 h, samples were washed three times with PBS buffer solution and redispersed in anti-FLAG antibodies conjugated horseradish peroxidase (Sigma, USA) with a final concentration of 1 ng/ml. After incubation at room temperature for 1 h, samples were washed three times with PBS buffer solution and transferred to a new tube. Signal was developed with 100 µl 3,3',5,5'- tetramethylbenzidine (TMBZ, Sigma) substrate solution (20 µg ml⁻¹ TMBZ and 0.2 µl H₂O₂ in 1 ml NaOAc, pH 6.0) for 5–30 min at 25°C. The reaction was stopped by adding 100 µl of 10% H₂SO₄ and absorbance of reaction supernatant was recorded at 450 nm with a reference at 655 nm using a micro plate reader (Model 680, Bio-Rad, Hercules, CA, USA).

4.2.11. Cellular imaging using hCC49 antibody Fab region conjugated FMNPs

Colon carcinoma cancer cells (LS174T) were seeded on slide glass 24 h prior to labeling and staining. LS174T cells were cultured with hCC49-conjugated NPs, without hCC49-conjugated NPs and HEK293 cells were cultured with hCC49-conjugated NPs for 24 h in a 37°C humidified incubator maintained at 5% CO₂. After incubation, fixation of the cells were carried out using 10%(v/v) formalin for 20 min and rinsed four times using PBS (pH 7.5). Then, 50 mmol NH₄Cl solutions were added and washed four times with

PBS (pH 7.5). Next, 4% BSA solution was used as a blocking agent for 1 h at RT. Following labeling, the slide glasses were washed four times PBS buffer (pH 7.5). After washes, cellular nuclei were stained with 1% (v/v) solution of DAPI in 2% BSA solution in PBS buffer (pH 7.5) for 1 h and washed with PBS (pH 7.5) four times. Confocal images were acquired using a confocal laser scanning microscope (LSM 700, Carl Zeiss Microimaging GmbH, 07740 Jena, Germany) and Image processing was performed using LSM Software ZEN 2010.

4.3. Results and discussion

4.3.1. Spectroscopic study of CdTe QDs and FMNPs

The absorbance and photoluminescence (PL) intensity of QDs are shown in Figure 5.1A. The absorbance shoulder of QDs was located at 502 nm, while the PL peak of QDs was situated at 522 nm. According to Peng's equation [118], the particle size of QDs was about 2.85 nm and concentration was 2.17 μM . Fluorescence emission spectrum of FMNPs was recorded for the supernatant and residue after magnetic separation from the reaction mixtures. Residual solution remained strong fluorescence intensity while supernatant had ignorable PL intensity (Figure 5.1B). This indicates most of QDs capped on MNPs. Such a stable PL property is favorable for labeling cancer cells. It is worth noting that the PL peak position (at 540 nm) for FMNPs in solutions red – shifted compared with free QDs, suggesting that some free NPs may aggregate to form clusters through partial electrostatic force. The clustering of individual QDs causes slight degradation of energy level, leading to narrower energy band gap and band broadening. However, it did not observe any further uncontrolled aggregation of QDs that may bring fluorescence quenching in the experiments because of strong repulsion forces among QDs through their highly negative surface charges.

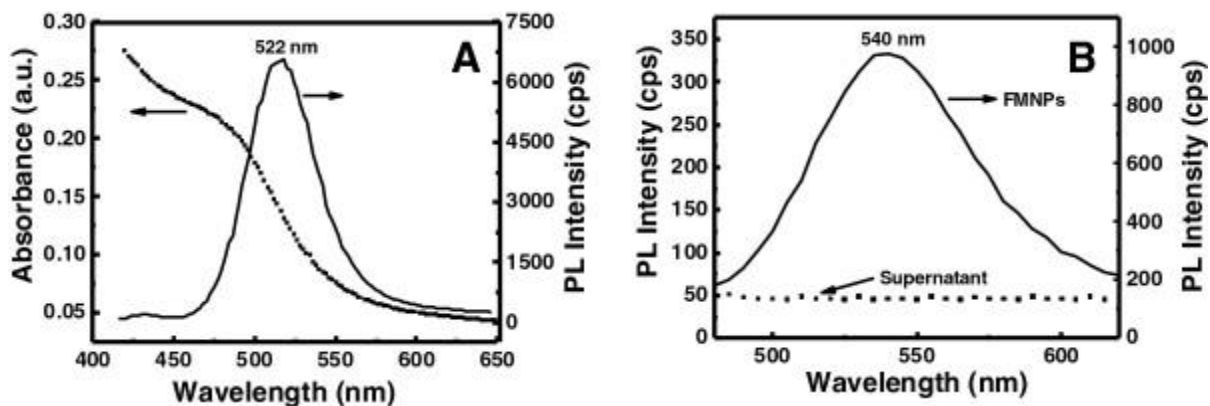


Figure 4.1: Spectroscopic analysis of CdTe QDs and FMNPs. (A) Absorbance and PL spectra of CdTe QDs; (B) PL spectra of FMNPs and supernatant solution.

4.3.2. Total internal reflection fluorescence (TIRF), transmission electron microscope (TEM) images and dynamic light scattering (DLS) studies of FMNPs

TIRF image shows the dark core made up of Fe_3O_4 NPs showing no fluorescence, whereas electrostatically adsorbed CdTe QDs covering the surface of NPs show distinct fluorescence (Figure 5.2A). Some single particle with distinct fluorescence property is also shown in inset of Figure 4.2A. TEM image of the FMNPs have shown the formation of core-shell NPs (Figure 5.2B). Fe_3O_4 NPs that are shown in black color, were covered by CdTe QDs that are shown transparent color. DLS data suggest that the size of FMNPs is about 50 nm (Figure 5.2C). Taking together these results smaller size CdTe QDs covered the surface of core Fe_3O_4 NPs. CTAB (not shown) between QDs and Fe_3O_4 NPs will avoid NPs to come in contact of each other, which would be helpful for better fluorescence emission. Due to the strong electrostatic interaction between the negatively charged $-\text{COO}^-$ groups on the surface of the CdTe QDs and the positively charged quaternary amino groups of the CTAB, some QDs are forced to aggregate and forming a thick shell. It is better to notify that the size of NPs in TIRF image is bigger than TEM image. Usually, TIRF microscope has limitation to measure small particle size. In this study, TIRF microscope specially used to observe core (dark) and shell (green) structure of FMNPs.

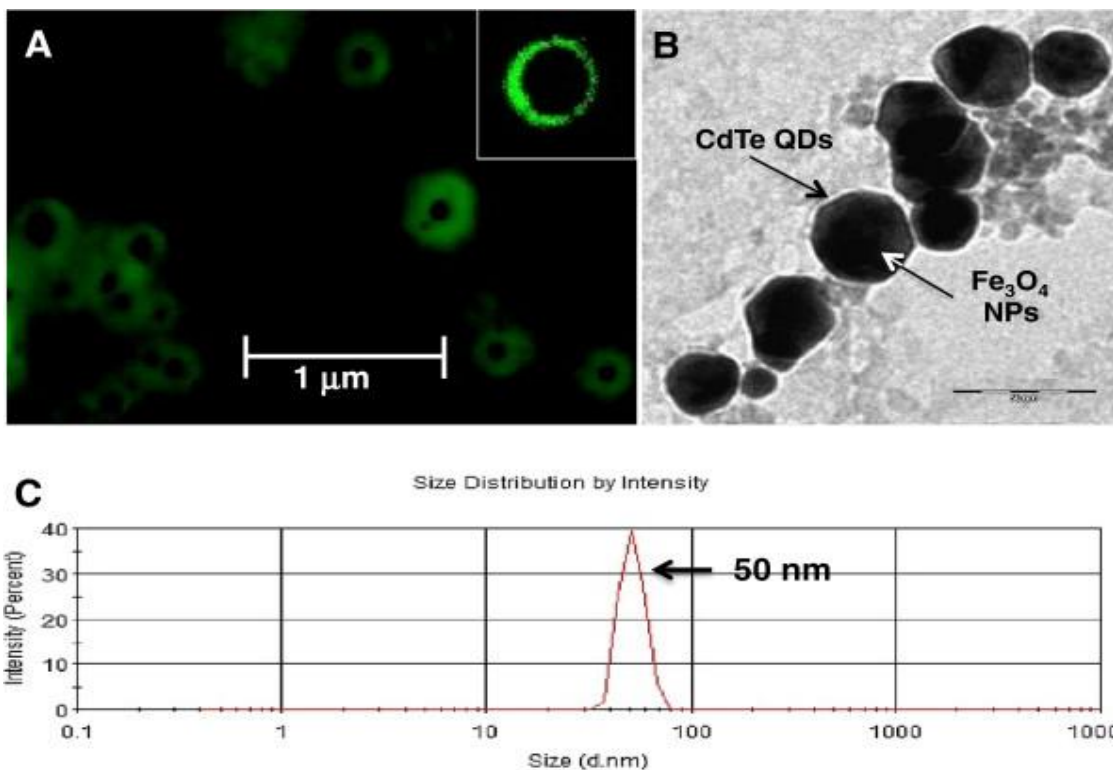


Figure. 4.2: Images of TIRF (A) and TEM (B), and DLS (C). Bars in A and B denote 1 μm and 50 nm, respectively.

4.3.3. Superconducting quantum interference device (SQUID) study of FMNPs

The FMNPs were prepared by encapsulating inorganic magnetic particles covered by inorganic QDs. The MNPs were coated with CTAB and CdTe QDs using self assembly method. Both the Fe₃O₄ MNPs and FMNPs exhibited typical superparamagnetic behavior due to no hysteresis. The remanence and coercivity are zero, illustrating that the particles respond magnetically to an external magnetic field, and redisperse rapidly when the magnetic field is removed. Figure 5.3 shows hysteresis loops of the proposed MNPs and FMNPs, which indicate that they possess a magnetic saturation value of about 71.0 and 65.0 emug⁻¹. This large saturation magnetization makes them very susceptible to magnetic fields. The decrease in the overall magnetization values indicates that the Fe₃O₄ surface is covered with nonmagnetic materials such as mostly QDs and some organic materials of CTAB and stabilizers. These FMNPs have superparamagnetism, and no magnetism remains without the magnetic field. These properties make the FMNPs a useful tool for micro-separation in fluidic systems.

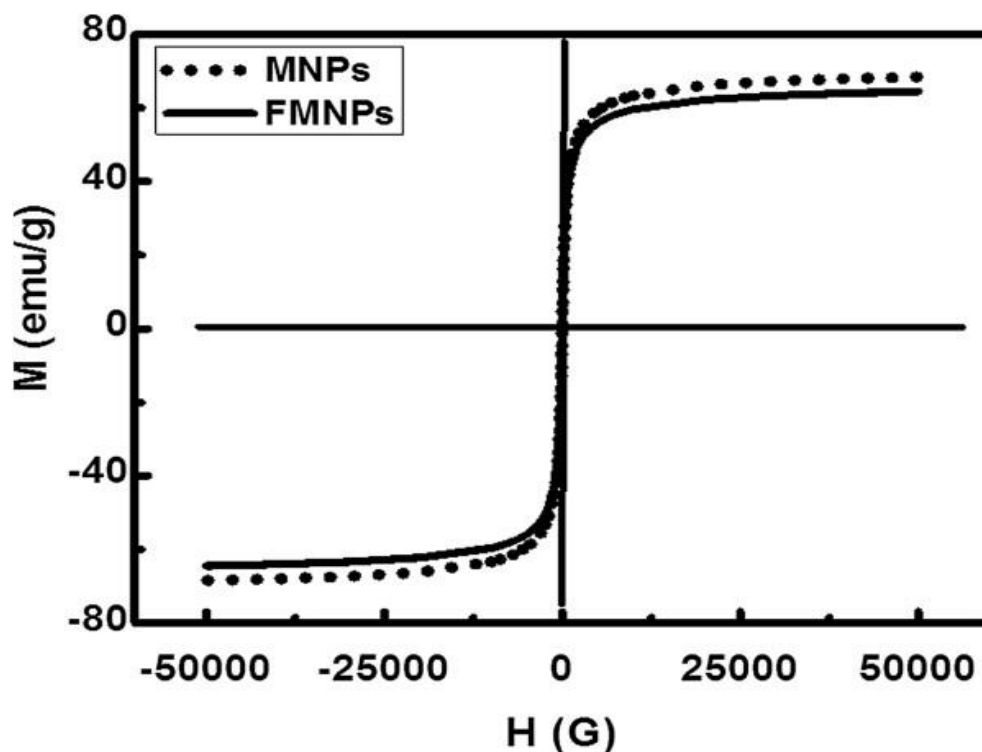


Figure 4.3: Hysteresis loops of the FMNPs. Magnetic properties of FMNPs and MNPs were measured using SQUID at 300 K.

4.3.4. Stability of FMNPs and cell viability in the presence of FMNPs

As far as the stability of FMNPs, the FMNPs are in aqueous solution at room temperature for > 1 month. PL intensity of FMNPs did not deteriorate until 4 weeks (Figure 5.4A). This superior colloidal stability of FMNPs results from the cationic surfactant layer between QDs and MNPs which avoids QDs to come in close proximity to MNPs and retained its optical properties. FMNPs can be precipitate using external magnetic field and redispersed in water. This type of precipitation and redispersion can be repeated many times, suggesting that NPs structures are very robust in nature. Fluorescence images of FMNPs during washing and cell labeling are also shown stable optical properties (Figure 5.4B).

FMNPs are toxic for Vero cells, but dilution of FMNPs led to lower cytotoxicity. About 64 times diluted solution of FMNPs has shown no cytotoxicity (Figure 5.4C).

Compared with TGA-capped CdTe QDs, the as-prepared QDs showed lower cytotoxicity under the same conditions (data not shown). Generally, CdTe QDs are highly toxic for cells due to the release of Cd^{2+} ions [119]. However, the prepared FMNPs reduce the cytotoxicity of QDs to a small extent. A reasonable interpretation is that the outer surface of FMNPs was covered by quaternary ammonium groups and leading to less released Cd^{2+} ions.

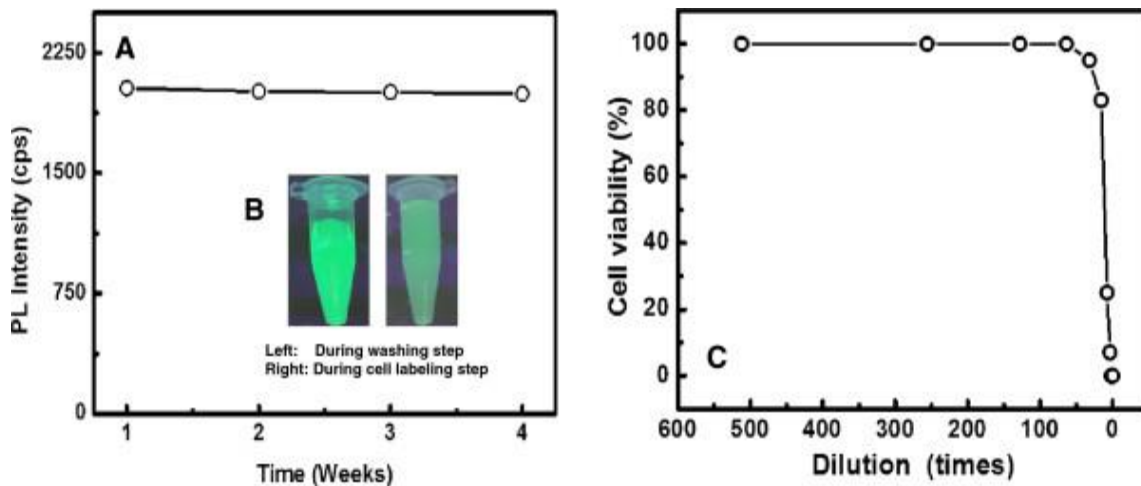


Figure 4.4: Stability of prepared FMNPs at room temperature (A), fluorescence images of FMNPs at different stages (B), and cell viability in the presence of FMNPs (C). The cytotoxicity of the FMNPs was measured using Vero cells by the trypan blue exclusion test.

4.3.5. Confirmation of FMNPs conjugated with Fab region of hCC49 antibody

FMNPs conjugated with Fab region of hCC49 antibodies are confirmed with bead enzyme-linked immunosorbent assay (ELISA). Higher signal was observed with Fab antibody modified FMNPs than only FMNPs (Figure 5.5), suggesting that the FMNPs was successfully conjugated with antibodies.

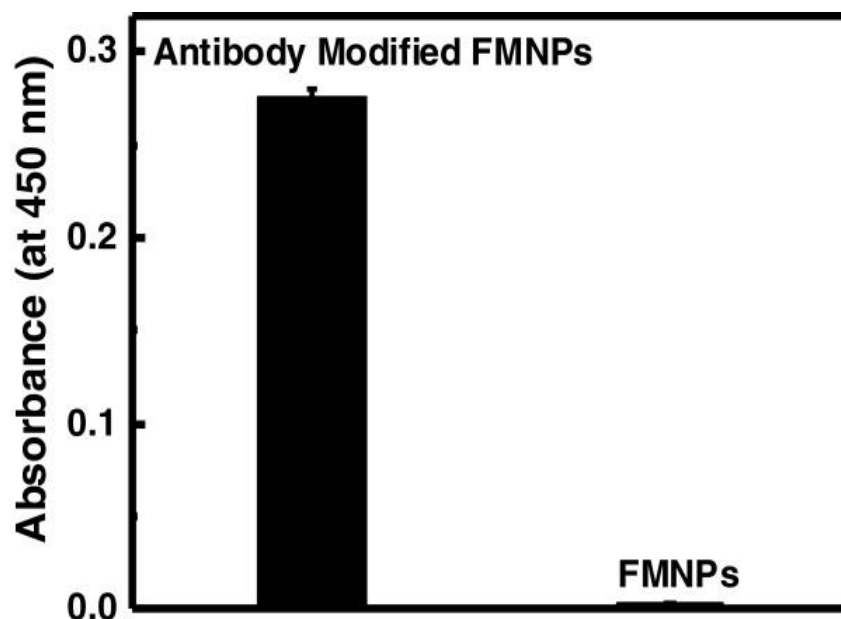


Figure 4.5: ELISA result for Figure 26: antibody conjugated with FMNPs. Anti-FLAG antibody and hCC49 antibody Fab region conjugation were performed on FMNPs.

4.3.6. Cellular imaging of colon carcinoma cells using FMNPs conjugated with Fab region of hCC49 antibody

Specific binding between FMNPs and cancer cells was observed by confocal laser scanning microscopy in vitro. When LS174T cancer cells were incubated with FMNPs conjugated with Fab region of hCC49 antibodies, green fluorescence around the nucleus (Figure 5.6D) confirming Fab region of antibodies bound with sialylated sugar chain in TAG-72 region of LS174T cancer cells. As a negative control, LS174T cancer cells were incubated without hCC49 antibodies Fab region-conjugated FMNPs. However, negative cells show only nucleus staining by 4',6- diamidino-2-phenylindole (DAPI) (Figure 5.6E), no green fluorescence around the nucleus. For more specificity, HEK293 cells were incubated with FMNPs conjugated with Fab region of hCC49 antibodies and merged image of DAPI and fluorescence confirmed no green fluorescence around the nucleus (Figure 5.6C and F). This indicates that HEK293 cells have no specific binding site of Fab region of hCC49 antibodies. Cell morphology was maintained after being incubated with the FMNPs, which implies that the nanocomposites had no cytotoxic effect on the

cancer cells. In addition, these confocal images confirmed that the NPs were bound the cell surface and the NPs accumulated uniformly around cell surface.

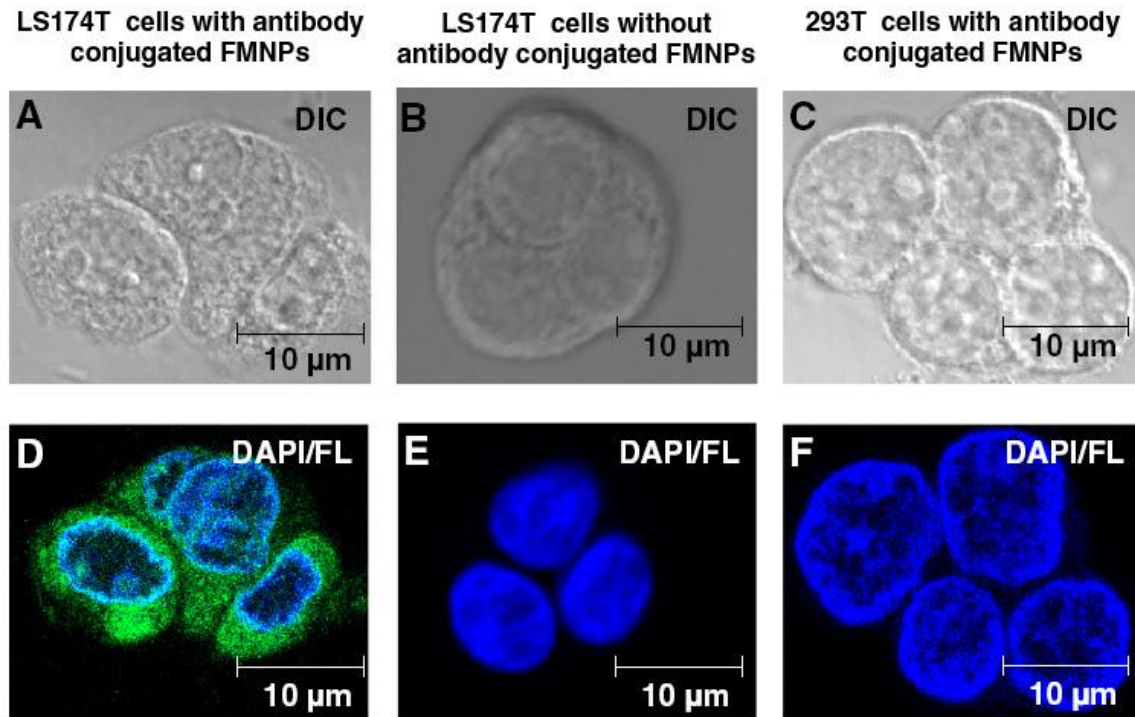


Figure 4.6: Confocal laser scanning microscopy images of cancer cells. Differential interference contrast (DIC) images of LS174T cells with (A), without (B) hCC49 antibody Fab region conjugated FMNPs, and 293 T cells with hCC49 antibody Fab region conjugated FMNPs (C). Merged images of DAPI/Fluorescence for LS174T cells with (D), without (E) hCC49 antibody Fab region conjugated FMNPs, and 293 T cells with hCC49 antibody Fab region conjugated FMNPs (F).

4.4. Conclusion

In conclusion, dual modal fluorescent-magnetic nanocomposites based on fluorescent CdTe QDs and Fe₃O₄ MNPs were developed by a simple LbL fabrication. This self-assembly technique retains the magnetic and fluorescence properties of FMNPs. FMNPs had good optical properties, and decent saturation magnetization. Further in vitro studies showing less toxicity at 64 fold dilutions and the ability to interact with cancer cells showing the ability of the FMNPs probes for imaging. Ultimately, it is believed that these particles will provide a new class of multimodal NPs for the complex biologic systems.

CHAPTER V
GENERAL CONCLUSIONS AND FUTURE
PERSPECTIVES

5.1. Conclusions

In this dissertation, we mainly focused on preparation of fluorescent hybrid nanostructure and their biological applications, i.e., bio-sensing and bio-imaging. Hybrid structures were made with (i) Ag Nanoneedles/ (CdSe/ZnS) QDs, (ii) Nanoporous Au leaf/ CdTe QDs and (iii) Fe₃O₄ NPs/ CdTe QDs. The important achievement from plasmonic/QDs hybrid system was manipulation of light due to plasmonic scattering and further applied such phenomena to construct supersensitive nanobio-sensor for virus detection. The detection limit was 2-order more sensitive than a commercially available rapid influenza diagnostic test. From these results, the proposed assay may offer a new strategy to monitor influenza virus for public health.

Besides those, a new engineered multifunctional nanoparticles (NPs) with combination of optical (QDs) and magnetic responses (MNPs) based on layer-by-layer (LbL) self-assembly techniques have developed and NPs conjugated with anti cancer antibodies were successfully labeled on colon carcinoma cells (LS174) *in vitro* and showed significant specificity to target cells. Such labeling of cells with new fluorescent-magneto nanoprobe for living detection is of interest to various biomedical applications and has demonstrated the potential for future medical use.

5.2. Future Perspectives

In recent decades, numerous developments have been achieved for preparation and application of fluorescent hybrid NPs in nanobiotechnological field. However, more importance should be given to a simple, cheap, sensitive, selective, and field portable detector. A significant part of the future work in this area must be focused on the preparation of rough plasmonic surface using self-assembly layer by layer technique and also magneto/fluorescent hybrid structure using same method.

In the past two decades, controlled synthesis of spherical superparamagnetic iron oxide nanoparticles have been developed as T2-negative contrast agents for magnetic resonance imaging in clinical use because of their biocompatibility and ease of synthesis; however, they exhibit relatively low transverse relaxivity. The investigation of iron oxide nanoparticles with different morphologies is rare, probably because it is difficult to prepare iron oxide nanoparticles with diverse shapes. The nanostructure-activity

relationship of iron oxide nanoparticles as MRI contrast agents has not been extensively exploited. Usually, non-spherical iron oxide nanoparticles exhibit an ultrahigh transverse relaxivity value, indicating that these iron oxide nanoparticles are much more effective T2 contrast agents for in vivo imaging and small tumour detection in comparison with conventional spherical iron oxide nanoparticles, which holds great promise for highly sensitive, early stage and accurate detection of cancer in the clinic.

Currently, we are in the initial state of fluorescent hybrid nanostructure based nanobiosensor. We hope that, in the near future, many researchers will take an interest in this field. This will be crucial for further development of this very important field of nano-biotechnology.

REFERENCES

- [1] Costi, R.; Saunders, A. E.; Banin, U., Colloidal Hybrid Nanostructures: A New Type of Functional Materials, *Angewandte Chemie International Edition* **2010**, *49* (29), 4878-4897.
- [2] Suh, W. H.; Suh, Y. H.; Stucky, G. D., Multifunctional nanosystems at the interface of physical and life sciences, *Nano Today* **2009**, *4* (1), 27-36.
- [3] Achermann, M., Exciton-Plasmon Interactions in Metal-Semiconductor Nanostructures, *J. Phys. Chem. Lett.* **2010**, *1* (19), 2837-2843.
- [4] Jiang, R.; Li, B.; Fang, C.; Wang, J., Metal/Semiconductor Hybrid Nanostructures for Plasmon-Enhanced Applications, *Adv. Mater.* **2014**, *26* (31), 5274-5309.
- [5] Lee, J.; Hernandez, P.; Lee, J.; Govorov, A. O.; Kotov, N. A., Exciton-plasmon interactions in molecular spring assemblies of nanowires and wavelength-based protein detection, *Nat Mater* **2007**, *6* (4), 291-295.
- [6] Chen, O.; Riedemann, L.; Etoc, F.; Herrmann, H.; Coppey, M.; Barch, M.; Farrar, C. T.; Zhao, J.; Bruns, O. T.; Wei, H.; Guo, P.; Cui, J.; Jensen, R.; Chen, Y.; Harris, D. K.; Cordero, J. M.; Wang, Z.; Jasanoff, A.; Fukumura, D.; Reimer, R.; Dahan, M.; Jain, R. K.; Bawendi, M. G., Magneto-fluorescent core-shell supernanoparticles, *Nat Commun* **2014**, *5*, 5093.
- [7] Bakalova, R.; Zhelev, Z.; Aoki, I.; Kanno, I., Designing quantum-dot probes, *Nat Photon* **2007**, *1* (9), 487-489.
- [8] Bruns, O. T.; Ittrich, H.; Peldschus, K.; Kaul, M. G.; Tromsdorf, U. I.; Lauterwasser, J.; Nikolic, M. S.; Mollwitz, B.; Merkel, M.; Bigall, N. C.; Sapra, S.; Reimer, R.; Hohenberg, H.; Weller, H.; Eychmuller, A.; Adam, G.; Beisiegel, U.; Heeren, J., Real-time magnetic resonance imaging and quantification of lipoprotein metabolism in vivo using nanocrystals, *Nat Nano* **2009**, *4* (3), 193-201.
- [9] Corr, S.; Rakovich, Y.; Gun'ko, Y., Multifunctional Magnetic-fluorescent Nanocomposites for Biomedical Applications, *Nanoscale Research Letters*, **2008**, *3* (3), 87-104.

- [10] Hwang, E.; Smolyaninov, I. I.; Davis, C. C., Surface Plasmon Polariton Enhanced Fluorescence from Quantum Dots on Nanostructured Metal Surfaces, *Nano Lett.*, **2010**, *10* (3), 813-820.
- [11] Lee, J.; Ahmed, S.; Oh, S.; Kim, J.; Suzuki, T.; Parmar, K.; Park, S.; Lee, J.; Park, E., A Plasmon-assisted fluoro-immunoassay using gold nanoparticles-decorated carbon nanotubes for monitoring the influenza virus, *Biosens. and Bioelectron.*, **2015**, *64*, 311-317.
- [12] Ahmed, S.; Cha, H.; Park, J.; Park, E.; Lee, D.; Lee, J., Photoluminescence enhancement of quantum dots on Ag nanoneedles, *Nanoscale Research Letters*, **2012**, *7* (1), 438.
- [13] Barnes, W. L. Light-emitting devices: Turning the tables on surface plasmons, *Nat Mater*, **2004**, *3* (9), 588-589.
- [14] Okamoto, K.; Niki, I.; Shvartser, A.; Narukawa, Y.; Mukai, T.; Scherer, A., Surface-plasmon-enhanced light emitters based on InGaN quantum wells, *Nat Mater*, **2004**, *3* (9), 601-605.
- [15] Resch-Genger, U.; Grabolle, M.; Cavaliere-Jaricot, S.; Nitschke, R.; Nann, T., Quantum dots versus organic dyes as fluorescent labels, *Nat Meth*, **2008**, *5* (9), 763-775.
- [16] Zhou, H.; Kim, J. P.; Bahng, J. H.; Kotov, N. A.; Lee, J., Self-Assembly Mechanism of Spiky Magnetoplasmonic Supraparticles, *Adv. Funct. Mater.*, **2014**, *24* (10), 1439-1448.
- [17] Yin, N.; Jiang, T.; Yu, J.; He, J.; Li, X.; Huang, Q.; Liu, L.; Xu, X.; Zhu, L., Study of gold nanostar@SiO₂@CdTeS quantum dots@SiO₂ with enhanced-fluorescence and photothermal therapy multifunctional cell nanoprobe, *J Nanopart Res*, **2014**, *16* (3), 1-10.
- [18] Zhou, H.; Dong, J.; Deo, V. K.; Park, E. Y.; Lee, J., Detection of anti-Neospora antibodies in bovine serum by using spiky Au-CdTe nanocomplexes, *Sensors and Actuators B: Chemical*, **2013**, *178* (0), 192-199.
- [19] Ahmed, S. R.; Hossain, M.; Park, J. Y.; Kim, S. H.; Lee, D.; Suzuki, T.; Lee, J.; Park, E. Y., Metal enhanced fluorescence on nanoporous gold leaf-based assay platform for virus detection, *Biosensors and Bioelectronics*, **2014**, *58* (0), 33-39.

- [20] Langhuth, H.; Frédérick, S.; Kaniber, M.; Finley, J.; Rührmair, U., Strong Photoluminescence Enhancement from Colloidal Quantum Dot Near Silver Nano-Island Films, *J Fluoresc*, **2011**, *21* (2), 539-543.
- [21] Okamoto, K.; Vyawahare, S.; Scherer, A., Surface-plasmon enhanced bright emission from CdSe quantum-dot nanocrystals, *J. Opt. Soc. Am. B*, **2006**, *23* (8), 1674-1678.
- [22] Li, X.; He, Y.; Zhang, T.; Que, L., Aluminum oxide nanostructure-based substrates for fluorescence enhancement, *Opt. Express*, **2012**, *20* (19), 21272-21277.
- [23] Zin M.T.; Leong K.; Wong N.Y.; Ma H.; Sarikaya M.; Jen A.K., Surface-plasmon-enhanced fluorescence from periodic quantum dot arrays through distance control using biomolecular linkers, *Nanotechnology*, **2009**, *20* (1), 015305.
- [24] Tanaka, K.; Plum, E.; Ou, J. Y.; Uchino, T.; Zheludev, N. I., Multi-fold quantum dot luminescence enhancement in a plasmonic metamaterial, **2010**, *105*, 227403.
- [25] Pacifico, J.; Gómez, D.; Mulvaney, P. A., Simple Route to Tunable Two-Dimensional Arrays of Quantum Dots, *Adv. Mater.*, **2005**, *17* (4), 415-418.
- [26] Chan, W. C. W.; Nie, S. Quantum Dot Bioconjugates for Ultrasensitive Nonisotopic Detection, *Science*, **1998**, *281* (5385), 2016-2018.
- [27] So, M. K.; Xu, C.; Loening, A. M.; Gambhir, S. S.; Rao, J., Self-illuminating quantum dot conjugates for in vivo imaging, *Nat Biotech*, **2006**, *24* (3), 339-343.
- [28] Medintz, I. L.; Clapp, A. R.; Mattoussi, H.; Goldman, E. R.; Fisher, B.; Mauro, J. M., Self-assembled nanoscale biosensors based on quantum dot FRET donors, *Nat Mater*, **2003**, *2* (9), 630-638.
- [29] Zhao, Z.; Zhou, Z.; Bao, J.; Wang, Z.; Hu, J.; Chi, X.; Ni, K.; Wang, R.; Chen, X.; Chen, Z.; Gao, J., Octapod iron oxide nanoparticles as high-performance T2 contrast agents for magnetic resonance imaging, *Nat Commun*, **2013**, *4*, 2266.
- [30] Laurent, S.; Forge, D.; Port, M.; Roch, A.; Robic, C.; Vander Elst, L.; Muller, R. N., Magnetic Iron Oxide Nanoparticles: Synthesis, Stabilization, Vectorization, Physicochemical Characterizations, and Biological Applications, *Chem. Rev.*, **2008**, *108* (6), 2064-2110.

- [31] Bulte, J. W. M.; Kraitchman, D. L., Iron oxide MR contrast agents for molecular and cellular imaging, *NMR Biomed.*, **2004**, *17* (7), 484-499.
- [32] Tassa, C.; Shaw, S. Y.; Weissleder, R. Dextran-Coated Iron Oxide Nanoparticles: A Versatile Platform for Targeted Molecular Imaging, Molecular Diagnostics, and Therapy, *Acc. Chem. Res.*, **2011**, *44* (10), 842-852.
- [33] Son, S. J.; Reichel, J.; He, B.; Schuchman, M.; Lee, S. B. Magnetic Nanotubes for Magnetic-Field-Assisted Bioseparation, Biointeraction, and Drug Delivery, *J. Am. Chem. Soc.*, **2005**, *127* (20), 7316-7317.
- [34] Bao, J.; Chen, W.; Liu, T.; Zhu, Y.; Jin, P.; Wang, L.; Liu, J.; Wei, Y.; Li, Y., Bifunctional Au-Fe₃O₄ Nanoparticles for Protein Separation, *ACS Nano*, **2007**, *1* (4), 293-298.
- [35] Haun, J. B.; Yoon, T. J.; Lee, H.; Weissleder, R., Magnetic nanoparticle biosensors, *WIREs Nanomed Nanobiotechnol*, **2010**, *2* (3), 291-304.
- [36] Insin, N.; Tracy, J. B.; Lee, H.; Zimmer, J. P.; Westervelt, R. M.; Bawendi, M. G., Incorporation of Iron Oxide Nanoparticles and Quantum Dots into Silica Microspheres, *ACS Nano*, **2008**, *2* (2), 197-202.
- [37] Sun, P.; Zhang, H.; Liu, C.; Fang, J.; Wang, M.; Chen, J.; Zhang, J.; Mao, C.; Xu, S. Preparation and Characterization of Fe₃O₄/CdTe Magnetic/Fluorescent Nanocomposites and Their Applications in Immuno-Labeling and Fluorescent Imaging of Cancer Cells, *Langmuir*, **2009**, *26* (2), 1278-1284.
- [38] Selvan, S. G. T.; Patra, P. K.; Ang, C. Y.; Ying, J. Y., Synthesis of Silica-Coated Semiconductor and Magnetic Quantum Dots and Their Use in the Imaging of Live Cells, *Angewandte Chemie International Edition*, **2007**, *46* (14), 2448-2452.
- [39] Yi, D. K.; Selvan, S. T.; Lee, S. S.; Papaefthymiou, G. C.; Kundaliya, D.; Ying, J. Y., Silica-Coated Nanocomposites of Magnetic Nanoparticles and Quantum Dots, *J. Am. Chem. Soc.*, **2005**, *127* (14), 4990-4991.
- [40] Mandal, S. K.; Lequeux, N.; Rotenberg, B.; Tramier, M.; Fattaccioli, J.; Bibette, J.; Dubertret, B., Encapsulation of Magnetic and Fluorescent Nanoparticles in Emulsion Droplets, *Langmuir*, **2005**, *21* (9), 4175-4179.
- [41] Beaune, G. g.; Dubertret, B.; Clément, O.; Vayssettes, C.; Cabuil, V. r.; Ménager, C., Giant Vesicles Containing Magnetic Nanoparticles and Quantum Dots:

- Feasibility and Tracking by Fiber Confocal Fluorescence Microscopy, *Angewandte Chemie International Edition*, **2007**, *46* (28), 5421-5424.
- [42] Lou, L.; Yu, K.; Zhang, Z.; Li, B.; Zhu, J.; Wang, Y.; Huang, R.; Zhu, Z., Functionalized magnetic-fluorescent hybrid nanoparticles for cell labelling. *Nanoscale*, **2011**, *3* (5), 2315-2323.
- [43] Roullier, V.; Grasset, F.; Boulmedais, F.; Artzner, F.; Cador, O.; Marchi-Artzner, V. r. Small Bioactivated Magnetic Quantum Dot Micelles, *Chem. Mater.*, **2008**, *20* (21), 6657-6665.
- [44] Shi, D.; Cho, H. S.; Chen, Y.; Xu, H.; Gu, H.; Lian, J.; Wang, W.; Liu, G.; Huth, C.; Wang, L.; Ewing, R. C.; Budko, S.; Pauletti, G. M.; Dong, Z., Fluorescent Polystyrene-F₃O₄ Composite Nanospheres for In Vivo Imaging and Hyperthermia, *Adv. Mater.*, **2009**, *21* (21), 2170-2173.
- [45] Zhang, B.; Cheng, J.; Gong, X.; Dong, X.; Liu, X.; Ma, G.; Chang, J., Facile fabrication of multi-colors high fluorescent/superparamagnetic nanoparticles, *Journal of Colloid and Interface Science*, **2008**, *322* (2), 485-490.
- [46] Di Corato, R.; Bigall, N. C.; Ragusa, A.; Dorfs, D.; Genovese, A.; Marotta, R.; Manna, L.; Pellegrino, T., Multifunctional Nanobeads Based on Quantum Dots and Magnetic Nanoparticles: Synthesis and Cancer Cell Targeting and Sorting, *ACS Nano*, **2011**, *5* (2), 1109-1121.
- [47] Hu, J.; Xie, M.; Wen, C. Y.; Zhang, Z. L.; Xie, H. Y.; Liu, A. A.; Chen, Y. Y.; Zhou, S. M.; Pang, D. W., A multicomponent recognition and separation system established via fluorescent, magnetic, dual encoded multifunctional bioprobes, *Biomaterials*, **2011**, *32* (4), 1177-1184.
- [48] Gaponik, N.; Radtchenko, I. L.; Sukhorukov, G. B.; Rogach, A. L., Luminescent Polymer Microcapsules Addressable by a Magnetic Field, *Langmuir*, **2004**, *20* (4), 1449-1452.
- [49] Zebli, B.; Susha, A. S.; Sukhorukov, G. B.; Rogach, A. L.; Parak, W. J., Magnetic Targeting and Cellular Uptake of Polymer Microcapsules Simultaneously Functionalized with Magnetic and Luminescent Nanocrystals, *Langmuir*, **2005**, *21* (10), 4262-4265.

- [50] Fan, H. M.; Olivo, M.; Shuter, B.; Yi, J. B.; Bhuvaneswari, R.; Tan, H. R.; Xing, G. C.; Ng, C. T.; Liu, L.; Lucky, S. S.; Bay, B. H.; Ding, J., Quantum Dot Capped Magnetite Nanorings as High Performance Nanoprobe for Multiphoton Fluorescence and Magnetic Resonance Imaging, *J. Am. Chem. Soc.*, **2010**, *132* (42), 14803-14811.
- [51] Liu, X.; Hu, Q.; Zhang, X.; Fang, Z.; Wang, Q., Generalized and Facile Synthesis of Fe₃O₄/MS (M = Zn, Cd, Hg, Pb, Co, and Ni) Nanocomposites, *J. Phys. Chem. C*, **2008**, *112* (33), 12728-12735.
- [52] Yu, X.; Wan, J.; Shan, Y.; Chen, K.; Han, X., A Facile Approach to Fabrication of Bifunctional Magnetic-Optical Fe₃O₄@ZnS Microspheres, *Chem. Mater.*, **2009**, *21* (20), 4892-4898.
- [53] Wang, Z.; Wu, L.; Chen, M.; Zhou, S., Facile Synthesis of Superparamagnetic Fluorescent Fe₃O₄/ZnS Hollow Nanospheres, *J. Am. Chem. Soc.*, **2009**, *131* (32), 11276-11277.
- [54] Gu, H.; Zheng, R.; Zhang, X.; Xu, B., Facile One-Pot Synthesis of Bifunctional Heterodimers of Nanoparticles: A Conjugate of Quantum Dot and Magnetic Nanoparticles, *J. Am. Chem. Soc.*, **2004**, *126* (18), 5664-5665.
- [55] Jose M.; Amber A. McBride.; John B. Plumley.; Yann Fichou.; Tosifa A. Memon.; Vichiksha Shah.; Nathaniel C. Cook.; Brain A. Akins.; Antonio C. Rivera.; Gennady A. Smolyakov.; James R. OBrien, Natalie L. Adolphi, Hugh D.C. Smyth and Marek Osinski, Synthesis and characterization of core/shell Fe₃O₄/ZnSe fluorescent magnetic nanoparticles, *J. of App. Phys.*, **2011**, *109*, 07B536.
- [56] Berkovitch, N.; Ginzburg, P.; Orenstein, M., Concave Plasmonic Particles: Broad-Band Geometrical Tunability in the Near-Infrared, *Nano Lett.*, **2010**, *10* (4), 1405-1408.
- [57] Chen, S.; Carroll, D. L., Synthesis and Characterization of Truncated Triangular Silver Nanoplates, *Nano Lett.*, **2002**, *2* (9), 1003-1007.
- [58] Govorov, A. O.; Bryant, G. W.; Zhang, W.; Skeini, T.; Lee, J.; Kotov, N. A.; Slocik, J. M.; Naik, R. R., Exciton-Plasmon Interaction and Hybrid Excitons in Semiconductor-Metal Nanoparticle Assemblies, *Nano Lett.*, **2006**, *6* (5), 984-994.

- [59] Sapienza, L.; Thyrestrup, H.; Stobbe, S.; Garcia, P. D.; Smolka, S.; Lodahl, P., Cavity Quantum Electrodynamics with Anderson-Localized Modes, *Science*, **2010**, 327 (5971), 1352-1355.
- [60] WurtzG.A.; PollardR.; HendrenW.; WiederrechtG.P.; GosztolaD.J.; PodolskiyV.A.; ZayatsA.V., Designed ultrafast optical nonlinearity in a plasmonic nanorod metamaterial enhanced by nonlocality, *Nat Nano*, **2011**, 6 (2), 107-111.
- [61] Lee, J.; Govorov, A. O.; Dulka, J.; Kotov, N. A., Bioconjugates of CdTe Nanowires and Au Nanoparticles: Plasmon-Exciton Interactions, Luminescence Enhancement, and Collective Effects, *Nano Lett.*, **2004**, 4 (12), 2323-2330.
- [62] Lee, J.; Javed, T.; Skeini, T.; Govorov, A. O.; Bryant, G. W.; Kotov, N. A., Bioconjugated Ag Nanoparticles and CdTe Nanowires: Metamaterials with Field-Enhanced Light Absorption, *Angewandte Chemie International Edition*, **2006**, 45 (29), 4819-4823.
- [63] Goumez, D. E.; Vernon, K. C.; Mulvaney, P.; Davis, T. J., Surface plasmon mediated strong exciton-photon coupling in semiconductor nanocrystals, *Nano Lett*, **2009**, 10, 274.
- [64] Gryczynski, I.; Malicka, J.; Jiang, W.; Fischer, H.; Chan, W. C. W.; Gryczynski, Z.; Grudzinski, W.; Lakowicz, J. R., Surface-plasmon-coupled emission of quantum dots, *J Phys Chem B*, **2004**, 109, 1088.
- [65] Barnes, W. L., Light-emitting devices: Turning the tables on surface plasmons, *Nat Mater*, **2004**, 3 (9), 588-589.
- [66] Hwang, E.; Smolyaninov, I. I.; Davis, C. C., Surface plasmon polariton enhanced fluorescence from quantum dots on nanostructured metal surfaces, *Nano Lett*, **2010**, 10, 813.
- [67] Ito, Y.; Matsuda, K.; Kanemitsu, Y., Mechanism of photoluminescence enhancement in single semiconductor nanocrystals on metal surfaces, *Phys Rev B*, **2007**, 75, 033309.
- [68] Leong, K.; Chen, Y.; Masiello, D. J.; Zin, M. T.; Hnilova, M.; Ma, H.; Tamerler, C.; Sarikaya, M.; Ginger, D. S.; Jen, A. K. Y., Cooperative near-field surface plasmon enhanced quantum dot nanoarrays, *Adv Funct Mater*, **2010**, 20, 2675.

- [69] Liu, F.; Tang, C.; Pan, J.; Cao, Z.; Wang, Z., A strategy for the maximum fluorescence enhancement based on tetrahedral amorphous carbon-coated metal substrates, *J Phys Chem C*, **2010**, *114*, 9871.
- [70] Okamoto, K.; Niki, I.; Shvartser, A.; Narukawa, Y.; Mukai, T.; Scherer, A., Surface-plasmon-enhanced light emitters based on InGaN quantum wells, *Nat Mater*, **2004**, *3*, 601.
- [71] Shimizu, K. T.; Woo, W. K.; Fisher, B. R.; Eisler, H. J.; Bawendi, M. G., Surface-enhanced emission from single semiconductor nanocrystals, *Phys Rev Lett*, **2002**, *89*, 117401.
- [72] Yeshchenko, O. A.; Dmitruk, I. M.; Alexeenko, A. A.; Losytsky, M. Y.; Kotko, A. V.; Pinchuk, A. O., Size-dependent surface-plasmon-enhanced photoluminescence from silver nanoparticles embedded in silica, *Phys Rev B*, **2009**, *79*, 235438.
- [73] Okamoto, K.; Scherer, A.; Kawakami, Y., Surface plasmon enhanced light emission from semiconductor materials, *Phys Status Solidi (c)*, **2008**, *5*, 2822.
- [74] Losic, D.; Shapter, J. G.; Mitchell, J. G.; Voelcker, N. H., Fabrication of gold nanorod arrays by templating from porous alumina, *Nanotechnology*, **2005**, *16*, 2275.
- [75] Liu, X. F.; Gao, Y.; Wang, X. M.; Wu, S. J.; Tang, Z. Y., Preparation of stable, water-soluble, highly luminescence quantum dots with small hydrodynamic sizes, *J Nanosci Nanotechnol*, **1941**, *2011*, 11.
- [76] Langhuth, H.; Frederick, S.; Kaniber, M.; Finley, J.; Ruhmair, U., Strong photoluminescence enhancement from colloidal quantum dot near silver nano-island films, *J Fluoresc*, **2010**, *21*, 539.
- [77] Bujak, L.; Piatkowski, D.; Mackowski, S.; Wormke, S.; Jung, C.; Brauchle, C.; Agarwal, A.; Kotov, N. A.; Schulte, T.; Hofmann, E.; Brotsudarmo, T. H. P.; Scheer, H.; Govorov, A. O.; Hiller, R. G., Plasmon enhancement of fluorescence in single light-harvesting complexes from *Amphidinium carterae*, *Acta Physica Polonica A*, **2009**, *116*, 22.

- [78] Link, S.; El-Sayed, M. A., Spectral properties and relaxation dynamics of surface plasmon electronic oscillations in gold and silver nanodots and nanorods, *J Phys Chem B*, **1999**, 1999, 103.
- [79] Drexhage, K. H., Interaction of light with monomolecular dye layers, *Progress in Optics*, **1974**, 163.
- [80] Ray, K.; Badugu, R.; Lakowicz, J. R., Metal-enhanced fluorescence from CdTe nanocrystals: a single-molecule fluorescence study, *J Am Chem Soc*, **2006**, 128, 8998.
- [81] Kawai, Y.; Kimura, Y.; Lezhava, A.; Kanamori, H.; Usui, K.; Hanami, T.; Soma, T.; Morlighem, J. t.; Saga, S.; Ishizu, Y.; Aoki, S.; Endo, R.; Oguchi-Katayama, A.; Kogo, Y.; Mitani, Y.; Ishidao, T.; Kawakami, C.; Kurata, H.; Furuya, Y.; Saito, T.; Okazaki, N.; Chikahira, M.; Hayashi, E.; Tsuruoka, S. i.; Toguchi, T.; Saito, Y.; Ban, T.; Izumi, S.; Uryu, H.; Kudo, K.; Sakai-Tagawa, Y.; Kawaoka, Y.; Hirai, A.; Hayashizaki, Y.; Ishikawa, T., One-Step Detection of the 2009 Pandemic Influenza A(H1N1) Virus by the RT-SmartAmp Assay and Its Clinical Validation, *PLoS ONE*, **2012**, 7 (1), e30236.
- [82] Bonanni, A.; Pividori, M. I.; del Valle, M., Impedimetric detection of influenza A (H1N1) DNA sequence using carbon nanotubes platform and gold nanoparticles amplification, *Analyst*, **2010**, 135 (7), 1765-1772.
- [83] Druce, J.; Tran, T.; Kelly, H.; Kaye, M.; Chibo, D.; Kostecky, R.; Amiri, A.; Catton, M.; Birch, C., Laboratory diagnosis and surveillance of human respiratory viruses by PCR in Victoria, Australia, 2002-2003., *J. Med. Virol.*, **2005**, 75 (1), 122-129.
- [84] Egashira, N.; Morita, S. i.; Hifumi, E.; Mitoma, Y.; Uda, T. Attomole Detection of Hemagglutinin Molecule of Influenza Virus by Combining an Electrochemiluminescence Sensor with an Immunoliposome That Encapsulates a Ru Complex, *Anal. Chem.*, **2008**, 80 (11), 4020-4025.
- [85] Owen, T. W.; Al-Kaysi, R. O.; Bardeen, C. J.; Cheng, Q., Microgravimetric immunosensor for direct detection of aerosolized influenza A virus particles, *Sensors and Actuators B: Chemical*, **2007**, 126 (2), 691-699.

- [86] Pavlovic, E.; Lai, R. Y.; Wu, T. T.; Ferguson, B. S.; Sun, R.; Plaxco, K. W.; Soh, H. T., Microfluidic Device Architecture for Electrochemical Patterning and Detection of Multiple DNA Sequences, *Langmuir*, **2008**, *24* (3), 1102-1107.
- [87] Rahman, M.; Vandermause, M. F.; Kieke, B. A.; Belongia, E. A., Performance of Binax NOW Flu A and B and direct fluorescent assay in comparison with a composite of viral culture or reverse transcription polymerase chain reaction for detection of influenza infection during the 2006 to 2007 season, *Diagnostic Microbiology and Infectious Disease*, **2008**, *62* (2), 162-166.
- [88] Driskell, J. D.; Jones, C. A.; Tompkins, S. M.; Tripp, R. A., One-step assay for detecting influenza virus using dynamic light scattering and gold nanoparticles, *Analyst*, **2011**, *136* (15), 3083-3090.
- [89] Gramotnev, D. K.; Bozhevolnyi, S. I., Plasmonics beyond the diffraction limit, *Nat Photon*, **2010**, *4* (2), 83-91.
- [90] Schuller, J. A.; Barnard, E. S.; Cai, W.; Jun, Y. C.; White, J. S.; Brongersma, M. L., Plasmonics for extreme light concentration and manipulation, *Nat Mater*, **2010**, *9* (3), 193-204.
- [91] Leong, K.; Chen, Y.; Masiello, D. J.; Zin, M. T.; Hnilova, M.; Ma, H.; Tamerler, C.; Sarikaya, M.; Ginger, D. S.; Jen, A. K. Y., Cooperative Near-Field Surface Plasmon Enhanced Quantum Dot Nanoarrays, *Adv. Funct. Mater.*, **2010**, *20* (16), 2675-2682.
- [92] Biener, J.; Nyce, G. W.; Hodge, A. M.; Biener, M. M.; Hamza, A. V.; Maier, S. A., Nanoporous Plasmonic Metamaterials, *Adv. Mater.*, **2008**, *20* (6), 1211-1217.
- [93] Ciesielski, P. N.; Scott, A. M.; Faulkner, C. J.; Berron, B. J.; Cliffler, D. E.; Jennings, G. K., Functionalized Nanoporous Gold Leaf Electrode Films for the Immobilization of Photosystem I, *ACS Nano*, **2008**, *2* (12), 2465-2472.
- [94] Detsi, E.; van de Schootbrugge, M.; Punzhin, S.; Onck, P. R.; De Hosson, J. T. M., On tuning the morphology of nanoporous gold, *Scripta Materialia*, **2011**, *64* (4), 319-322.
- [95] Gaponik, N.; Talapin, D. V.; Rogach, A. L.; Hoppe, K.; Shevchenko, E. V.; Kornowski, A.; Eychmüller, A.; Weller, H., Thiol-Capping of CdTe Nanocrystals:

- An Alternative to Organometallic Synthetic Routes, *J. Phys. Chem. B*, **2002**, *106* (29), 7177-7185.
- [96] Ouyang, J.; Chang, M.; Zhang, Y.; Li, X., CdSe-sensitized TiO₂ nanotube array film fabricated by ultrasonic-assisted electrochemical deposition and subsequently wrapped with TiO₂ thin layer for the visible light photoelectrocatalysis, *Thin Solid Films*, **2012**, *520* (7), 2994-2999.
- [97] Wiley, D. C.; Skehel, J. J. The Structure and Function of the Hemagglutinin Membrane Glycoprotein of Influenza Virus, *Annu. Rev. Biochem.*, **1987**, *56* (1), 365-394.
- [98] Cheon, J.; Lee, J. H. Synergistically integrated nanoparticles as multimodal probes for nanobiotechnology, *Acc Chem Res*, **2008**, *41*, 1630-1640.
- [99] Mahmoudi, M.; Shokrgozar, M. A., Multifunctional stable fluorescent magnetic nanoparticles, *Chem Commun*, **2012**, *48*, 3957-3959.
- [100] Xu, W.; Kattel, K.; Park, J. Y.; Chang, Y.; Kim, T. J.; Lee, G. H., Paramagnetic nanoparticle T1 and T2 MRI contrast agents, *Phys Chem Chem Phys*, **2012**, *14*, 12687-12700.
- [101] Bao, F.; Yao, J. L.; Ren-Ao Gu, R. A., Synthesis of magnetic Fe₂O₃/Au core/shell nanoparticles for bioseparation and immunoassay based on surface-enhanced raman spectroscopy, *Langmuir*, **2009**, *25*, 10782-10787.
- [102] Wang, Y.; Dostalek, J.; Knoll, W., Magnetic nanoparticle-enhanced biosensor based on grating-coupled surface plasmon resonance, *Anal Chem*, **2011**, *83*, 6202-6207.
- [103] Kobayashi, T., Cancer hyperthermia using magnetic nanoparticles, *Biotechnol J*, **2011**, *6*, 1342-1347.
- [104] Verma, N. K.; Crosbie-Staunton, K.; Satti, A.; Gallagher, S.; Ryan, K. B.; Doody, T.; McAtamney, C.; MacLoughlin, R.; Galvin, P., Magnetic core-shell nanoparticles for drug delivery by nebulization, *J Nanobiotechnol*, **2013**, *11*, 1.
- [105] Ge, Y.; Zhang, Y.; He, S.; Nie, F.; Teng, G.; Gu, N., Fluorescence modified chitosan-coated magnetic nanoparticles for high-efficient cellular imaging, *Nanoscale Res Lett*, **2009**, *4*, 287-295.

- [105] Chekina, N.; Horak, D.; Jendelova, P.; Trchova, M.; Benes, M. J.; Hruby, M.; Herynek, V.; Turnovcova, K.; Sykova, E., Fluorescent magnetic nanoparticles for biomedical applications, *J Mater Chem*, **2011**, *21*, 7630-7639.
- [106] Vargas, J. M.; McBride, A. A.; Plumley, J. B.; Fichou, Y.; Memon, T. A.; Shah, V.; Cook, N. C.; Akins, B. A.; Rivera, A. C., Synthesis and characterization of core/shell Fe₃O₄/ZnSe fluorescent magnetic nanoparticles, *J Appl Phys*, **2011**, *109*, 07B536-07B563.
- [107] Zhang, B.; Chen, B.; Wang, Y.; Guo, F.; Li, Z.; Shi, D., Preparation of highly fluorescent magnetic nanoparticles for analytes-enrichment and subsequent biodetection, *J Colloid Interface Sci*, **2011**, *353*, 426-432.
- [108] Quarta, A.; Di Corato, R.; Manna, L.; Ragusa, A.; Pellegrino, T. Fluorescent-magnetic hybrid nanostructures: preparation, properties, and applications in biology, *NanoBiosci, IEEE Trans on 2007*, *6*, 298-308.
- [109] Fu, A.; Wilson, R. J.; Smith, B. R.; Mullenix, J.; Earhart, C.; Akin, D.; Guccione, S.; Wang, S. X.; Gambhir, S. S., Fluorescent magnetic nanoparticles for magnetically enhanced cancer imaging and targeting in living subjects, *ACS Nano*, **2012**, *6*, 6862-6869.
- [110] Yang, J.; Lee, J.; Kang, J.; Chung, C. H.; Lee, K.; Suh, J. S.; Yoon, H. G.; Huh, Y. M.; Haam, S., Magnetic sensitivity enhanced novel fluorescent magnetic silica nanoparticles for biomedical applications, *Nanotechnol*, **2008**, *19*, 075610.
- [111] Ebrahimezhad, A.; Ghasemi, Y.; Rasoul-Amini, S.; Barar, J.; Davaran, S., Preparation of novel magnetic fluorescent nanoparticles using amino acids, *Colloids Surf, B*, **2013**, *102*, 534-539.
- [112] Chang, I. P.; Hwang, K. C.; Chiang, C. S., Preparation of fluorescent magnetic nanodiamonds and cellular imaging, *J Am Chem Soc*, **2008**, *130*, 15476-15481.
- [113] Kashmiri, S. V.; Iwahashi, M.; Tamura, M.; Padlanm, E. A.; Milenic, D. E.; Schlom, J. Development of a minimally immunogenic variant of humanized anti-carcinoma monoclonal antibody CC49. *Crit Rev Oncol Hematol*, **2001**, *38*, 3-16.
- [114] Alderson, R. F.; Toki, B. E.; Roberge, M.; Geng, W.; Basler, J.; Chin, R.; Liu, A.; Ueda, R.; Hodges, D., Characterization of a CC49-based single-chain fragment-

- beta-lactamase fusion protein for antibody-directed enzyme prodrug therapy (ADEPT), *Bioconjug Chem*, **2006**, *17*, 410-418.
- [115] Yoon, S. O.; Lee, T. S.; Kim, S. J.; Jang, M. H.; Kang, Y. J.; Park, J. H.; Kim, K. S.; Lee, H. S.; Ryu, C. J., Construction, affinity maturation, and biological characterization of an anti-tumor-associated glycoprotein-72 humanized antibody, *J Biol Chem*, **2006**, *281*, 6985-6992.
- [116] Chang, B.; Zhang, X.; Guo, J.; Sun, Y.; Tang, H.; Ren, Q.; Yang, W., General one-pot strategy to prepare multifunctional nanocomposites with hydrophilic colloidal nanoparticles core/mesoporous silica shell structure, *J of Colloid Interf Sci*, **2012**, *377*, 64-75.
- [117] Ahmed, S.; Hong, S.; Lee, J., Optical and electrical nano eco-sensors using alternative deposition of charged layer, *Front Mater Sci*, *2011*, *5*, 40-49.
- [118] Yu, W. W.; Qu, L.; Guo, W.; Peng, X., Experimental determination of the extinction coefficient of CdTe, CdSe, and CdS nanocrystals, *Chem Mater*, **2003**, *15*, 2854-2860.
- [119] Derfus, A. M.; Chan, W. C. W.; Bhatia, S. N., Probing the cytotoxicity of semiconductor quantum dots, *Nano Lett*, **2003**, *4*, 11-18.

LIST OF PUBLICATIONS

- (1) **Syed Rahin Ahmed**, Md. Ashraf Hossain, Jung Youn Park, Soo-Hyung Kim, Dongyun Lee, Tetsuro Suzuki, Jaebeom Lee, Enoch Y. Park, (2014). Metal enhanced fluorescence on nanoporous gold leaf-based assay platform for virus detection, *Biosensors and Bioelectronics*, 58: 33.
- (2) Jaewook Lee, **Syed Rahin Ahmed**, Sangjin Oh, Jeonghyo Kim, Tetsuro Suzuki, Kaushik Parmar, Simon S. Park, Jaebeom Lee, Enoch Y. Park, (2015). A plasmon assisted fluoro-immunoassay using gold nanoparticle-decorated carbon nanotubes for monitoring the influenza virus, *Biosensors and Bioelectronics*, 64: 311.
- (3) Jaewook Lee, Jeonghyo Kim, **Syed Rahin Ahmed**, Hongjian Zhou, Jong-Man Kim, and Jaebeom Lee, (2014). Plasmon-induced photoluminescence immunoassay for tuberculosis monitoring using gold nanoparticles decorated graphene, *ACS Appl. Mater. Interfaces*, 6: 21380.
- (4) **Syed Rahin Ahmed**, Jinhua Dong, Megumi Yui, Tatsuya Kato, Jaebeom Lee, Enoch Y Park, (2013). Quantum dots incorporated magnetic nanoparticles for imaging colon carcinoma cells, *Nanobiotechnology*, 11: 28.
- (5) **Syed Rahin Ahmed**, Kwangnak Koh, Enoch Y. Park, and Jaebeom Lee, (2013). Toxic chemical monitoring of agricultural bioproducts using nanomaterials-based sensors, *Korean J. Chem. Eng.*, 30: 1825.
- (6) **Syed Rahin Ahmed**, Hee Ryoung Cha, Jung Youn Park, Enoch Y. Park, Dongyun Lee, Jaebeom Lee, (2012). Photoluminescence enhancement of quantum dots on Ag nanoneedles, *Nanoscale Res. Lett.*, 7: 438.
- (7) **Syed Rahin Ahmed**, Kwangnak Koh, Nam Lyong Kang, and Jaebeom Lee, (2012). Highly Sensitive Fluorescent Probes for the Quantitative Determination of Singlet Oxygen ($^1\text{O}_2$), *Bull. Korean Chem. Soc.*, 33: 1608.
- (8) **Syed Rahin Ahmed**, Seong Cheol Hong Jaebeom Lee, (2011). Optical and electrical nano eco-sensors using alternative deposition of charged layer, *Frontiers of Materials Science*, 5: 40.

ACKNOWLEDGEMENT

My highest regards and gratitude go to my advisors, Prof. Dr. Enoch Y Park and Prof. Dr. Jaebeom Lee, for their guidance, teaching, support, as well as providing a wonderful environment for doing research in the two groups. They have enlightened my life and both are unique in my heart. Their enthusiasm toward science and their knowledge, dedication, hard-work, and creativity are the landmarks for me to follow in life. I especially thank Prof. Dr. Enoch Y Park for providing positions and a welcoming atmosphere for doing research in your group. I would also like to thank for his assistance and guidance in getting my graduate career started on the right foot and providing me with the foundation for becoming a researcher.

I would like to thank my former research partners and friends, too. They are Megumi Yui, Dr. Jaewook Lee, Dr. Hongjian Zhou Takahashi Naoto and Md. Ashraf Hossain. Thanks for more than five years of pleasant work together. I really enjoyed those days, months and years.

Special thanks go out to Prof Jinhua Dong, who helped to bring influenza virus detection project to fruition. I am so deeply grateful for his help, professionalism, and valuable guidance throughout this project.

I would like to thank the Ministry of Education, Science, Sports and Culture (Monbukagakusho), Government of Japan for awarding the Monbukagakusho Scholarship to proceed with my research successfully, without which the output of this thesis writing might have been impossible.

I would like to begin by thanking to my family. To my family members, I am grateful for their understanding and support on my choice to leave home for a better education. For my father who raised me with a love of science and supported me in all my pursuits. No words are sufficient to describe my late mother contribution to my life. I owe every bit of my existence to her. This dissertation is dedicated for her memory. Finally, for my loving, supportive, encouraging, and patient wife Farhana Zaman whose faithful support during the final stages of this Ph.D. is so appreciated. Thank you.